CHAPTER 2

Detector Optimisation

The choice of the main parameters of the ILD, such as the magnetic field, B, and overall size, is motivated by extensive simulation studies based on variants of the GLD [2] and LDC [3] detector concepts. The main studies, described in the following sections, are of: i) the performance of particle flow calorimetry in terms of jet energy resolution; ii) the tracking performance for momentum resolution and impact parameter resolution; iii) the beam-related backgrounds and the impact of the choice of B; iv) the efficiency and purity of heavy flavour tagging; v) and the impact on physics performance in three benchmark processes.

Ideally the overall detector cost would feed directly into the optimisation of the ILD detector. However, because of the large uncertainties in the cost of raw materials and detector sensors, it is felt that the approach of optimising the detector performance for a fixed cost is not reliable at this stage. Hence, whilst cost is a consideration in defining the parameters of the ILD concept, the main criterion is to develop a detector concept optimised for physics at the ILC.

2.1 SIMULATION TOOLS AND DETECTOR PARAMETERS

The optimisation of the ILD concept was performed in parallel using the software tools developed by the GLD and the LDC groups. The detector models were simulated using a fairly detailed GEANT4 [5] simulation. A significant effort has been made to use a reasonable geometry for the subdetectors, including a description of dead regions and support structures, as described in in Section 3.1. The studies presented are based on full reconstruction of the simulated events without reference to the Monte Carlo (MC) truth information.

Six detector models were defined; three based on the GLD simulation (GLD, GLDPrime and GLD4LDC) and three based on the LDC simulation (LDC, LDCPrime, and LDC4GLD). The main parameters of the models are summarised in Table 2.1-1. The models represent different compromises between magnetic field and TPC outer radius. The software frameworks (JSF/Jupiter/Satellites and Mokka/Marlin) used to simulate and reconstruct the detector models are summarised below. The detector simulation was performed using GEANT4 (version 9.1 patch01) with the `LCPhysics` physics list [6].

Model Name		GLD	GLD′	GLD4LDC	LDC4GLD	LDC′	LDC	ILD
Simulator		Jupiter			Mokka			Mokka
B field (T)		3.0	3.5	4.0	3.0	3.5	4.0	3.5
Beampipe R_{min}		15.0	14.0	13.0	15.5	14.0	13.0	14.5
Vertex Detector	Geometry	cylindrical			ladders			ladders
	Layers	3 doublets			5			3 doublets
	R_{min}	17.5	16.0	15.0	16.5	15.0	14.0	16.0
Barrel SIT	Layers	4 cylinders			2 cylinders			2 cylinders
	Radii	90, 160, 230, 300			161.4, 270.1			165, 309
TPC drift region	R_{min}	437	435	371	371			395
	R_{max}	1978	1740	1520	1931	1733	1511	1739
	z_{max}	2600	2350	2160	2498	2248	2186	2247.5
TPC pad rows		256	217	196	260	227	190	224
ECAL barrel	R_{min}	2100	1850	1600	2020	1825	1610	1847.4
	Layers	33			20(thin)+9(thick)			20+9
	Total X_0	28.4			22.9			23.6
ECAL endcap z_{min}		2800	2250	2100	2700	2300	2550	2450
HCAL barrel	Layers	46	42	37	48			48
	R_{max}	3617	3260	2857	3554	3359	3144	3330
λ_I (ECAL+HCAL)		6.79	6.29	5.67	6.86			6.86

TABLE 2.1-1
Geometrical parameters of the baseline detector models used for the optimisation studies (GLD, GLDPrime, GLD4LDC, LDC4GLD, LDCPrime and LDC). Also shown are the corresponding parameters for the ILD baseline detector. Unless otherwise specified, values are shown in units of mm.

2.1.1 GLD Software: JSF

JSF [7] is a ROOT [8] based software framework for modular applications, such as event generation, fast and full simulation, event reconstruction and data analysis. The two main components are Jupiter [9] and Satellites [9]. Jupiter is a GEANT4 based detector simulation, designed to enable easy installation and modification of subdetector components. Satellites is a collection of event reconstruction modules in the JSF framework. Satellites includes smearing of hit points simulated by Jupiter, a "cheated" track finder using MC information to associate hits to tracks, a Kalman Filter based track fitter, and a cheated particle flow algorithm (PFA).

Jupiter reads a set of detector parameters at run time from a text file, which makes it easy to study different detector configurations. The geometry information is saved in an output ROOT file for use by event reconstruction. In the Jupiter detector simulation the vertex detector and intermediate silicon trackers are modelled as cylinders. The calorimeters have a 12-fold symmetry. The electromagnetic calorimeter consists of a sandwich structure comprising layers of 3 mm of tungsten absorber, 2 mm of scintillator, and a 1 mm air gap. The hadron calorimeter consists of layers comprising of 20 mm of iron absorber, 5 mm of

plastic scintillator, and a 1 mm air gap. For the purpose of simulation, the scintillator in both the ECAL and HCAL is segmented into $1 \times 1\,\mathrm{cm}^2$ readout tiles. Signals in these tiles can be combined at the time of reconstruction to simulate the strip readout structure of proposed system. In the version of the simulation used for the studies presented here, there is no gap between the ECAL and HCAL. Jupiter was executed as a module of the JSF and GEANT4 hits in each sensitive detector are saved in a ROOT file for subsequent study with the Satellites package or as an LCIO [10] file for reconstruction with MarlinReco [11].

The point resolution of the tracking chambers was implemented in the Satellites reconstruction. The GEANT4 hit points in the vertex detector (VTX) and intermediate silicon tracker (IT) were smeared with a Gaussian with the following resolutions. For the VTX, $\sigma_{r\phi}$ and σ_z were taken to be 2.8μm. For the barrel silicon tracker, a resolution of $10\,\mu$m was used for both $\sigma_{r\phi}$ and σ_z. The TPC space points were smeared by Gaussian resolutions, $\sigma_{r\phi}$ and σ_z, given by the following physically motivated form:

$$\begin{aligned} \sigma^2_{r\phi}/\mu\mathrm{m}^2 &= 50^2 + 900^2 \sin^2\phi + \left((25^2/22) \times (4/B)^2 \sin\theta\right) z; \\ \sigma^2_{z}/\mu\mathrm{m}^2 &= 40^2 + 8^2 \times z; \end{aligned}$$

where z is the drift length in cm, B is the magnetic field strength in Tesla, and θ and ϕ are the track angles with respect to the axes perpendicular to the readout plane and perpendicular to the pad rows. For the calorimeter hits, no additional smearing is applied at reconstruction time; the simulated energy deposits in the scintillator tiles are used directly.

The optimisation studies in the GLD framework use the Satellites reconstruction to investigate tracking performance and MarlinReco for other studies. The interoperability between the two software frameworks is provided by the LCIO data format, *e.g.* after simulating the detector response with the Jupiter program, MarlinReco and PandoraPFA [12] were used for the event reconstruction.

2.1.2 LDC Software: Mokka and Marlin

The software framework developed by the LDC concept is based on the LCIO persistency format and event data model. The detailed simulation of the detector response is performed by the GEANT4 based Mokka [13] application. The detailed subdetector geometries and component materials are stored in a MySQL database. The overall detector is then built from individual subdetectors, making it relatively straightforward to compare different technology choices. The corresponding `C++` code instantiating the subdetector geometry in memory is written such that the whole detector model can be scaled in length and radius; this feature proved invaluable in optimising the detector geometry. The GEAR [14] package provides access to these geometrical detector properties at the reconstruction and analysis level. The Mokka simulation of the different subdetectors is described in more detail in Section 3.1.

The Mokka generated events are processed in Marlin [15]. Marlin is a modular `C++` application framework which supports plug-in modules (called processors) which can be loaded at runtime. This plug-in-based design supports the distributed development of reconstruction algorithms and also allows comparison of different algorithms at runtime, *e.g.* it is possible to run two tracking algorithms producing parallel collections of reconstructed tracks.

Event reconstruction is performed with the MarlinReco [16] package. This consists of a set of modules for digitisation, track finding, track fitting, particle flow reconstruction, and flavour tagging. The hit smearing for the tracking detectors is implemented at the digitisation stage using the same parameterisation as used for Satellites, except that resolutions

for the intermediate silicon tracker (SIT) are taken to be $4\,\mu$m for $\sigma_{r\phi}$ and $50\,\mu$m for σ_z. The pattern recognition processors use Kalman Filter techniques and code developed for the LEP experiments. Tracks from standalone pattern recognition in the silicon trackers and in the TPC are combined and refitted, The resulting momentum resolution is discussed in Section 3.2.1. Reconstruction of the individual particles in the event is performed with the particle flow algorithm in the PandoraPFA [12] package, currently the best algorithm available. The LCFIVertex [17] package provides sophisticated code for vertex finding/fitting and for the identification of heavy flavour jets using a neural network approach. It also provides jet charge estimation. In addition to reconstruction algorithms, MarlinReco includes a set of analysis tools such as algorithms for jet finding and kinematic fitting. The RAVE toolkit [18], also available within Marlin, provides an alternative set of vertex reconstruction based on linear and non-linear estimators. tools such as algorithms for jet finding and kinematic fitting.

2.2 DETECTOR OPTIMISATION FOR PARTICLE FLOW

One of the main design considerations for a detector at the ILC is the ability to efficiently identify and distinguish $Z \to q\bar{q}$ and $W \to q\bar{q}$ decays. This imposes the requirement that the di-jet mass resolution should be comparable to the natural widths of the electroweak gauge bosons, $\sigma_m/m < 2.7\,\% \approx \Gamma_Z/m_Z \approx \Gamma_W/m_W$. In terms of jet energy resolution this requirement approximately corresponds to $\sigma_E/E < 3.8\,\%$. After accounting for the gauge boson widths, this results in a ~ 2.75 standard deviation separation of the W and Z mass peaks for di-jet events. Most of the interesting physics at the ILC, operating in the centre-of-mass range $\sqrt{s} = 0.5 - 1.0\,\text{TeV}$, will consist of final states with four or more fermions and for processes near threshold, the gauge bosons will decay almost at rest. Hence the typical di-jet energies of interest will be in the range $80 - 350\,\text{GeV}$. This sets the requirement on calorimetric performance of $\sigma_E/E \sim 30\,\%/\sqrt{E}$. It has been demonstrated that one way of reaching this goal is particle flow calorimetry [12]. Whilst, the separation of W and Z bosons defines the *minimum* requirement for the jet energy resolution, it should be remembered that di-jet invariant masses will be an important part of the event selection for many physics analyses; the jet energy resolution will affect the signal-to-background ratio in many analyses.

The ILD concept is based on the belief that particle flow calorimetry provides the best way of achieving the ILC jet energy goals. Particle flow reconstruction places strong requirements on the subdetector technologies and the overall detector design. Particle flow calorimetry requires efficient separation of photons and showers produced by neutral hadrons from showers produced by the interactions of charged hadrons. This implies high granularity calorimetry and that both the ECAL and HCAL lie inside the detector solenoid. For high energy jets, failures in the ability to efficiently separate energy deposits from different particles, the *confusion* term, will dominate the jet energy resolution. The physical separation of calorimetric energy deposits from different particles will be greater in a large detector, scaling as the inner radius of the ECAL, R, in the barrel region and the detector length, L, in the endcap region. There are also arguments favouring a high magnetic field, as this will tend to deflect charged particles away from the core of a jet. The scaling law here is less clear. The separation between a charged particle and an initially collinear neutral particle will scale as BR^2. However, there is no reason to believe that this will hold for a jet of (non-collinear) neutral and charged particles. The true dependence of particle flow on the overall detector parameters (B and R) has to be evaluated empirically.

2.2.1 Particle Flow Optimisation Methodology

The particle flow optimisation studies for ILD use the PandoraPFA algorithm[12] to reconstruct events for both the LDC and the GLD detector models. All studies are based on full reconstruction of the tracking and the calorimetric information. The starting point for the optimisation studies is the LDCPrime model with a 3.5 T magnetic field, an ECAL inner radius of 1825 mm and a 48 layer ($6\lambda_I$) HCAL. The ECAL and HCAL transverse segmentations are $5 \times 5\,\mathrm{mm}^2$ and $3 \times 3\,\mathrm{cm}^2$ respectively. The studies use variations of this model where (usually) a single parameter is changed and the dependence of jet energy resolution is determined as a function of this parameter. For each model variation, particle flow performance was evaluated using samples of approximately 10000 $Z \rightarrow q\bar{q}$ events (only light quarks, *i.e.* $q = u, d, s$) generated with the Z decaying at rest (no ISR or beamstrahlung) with $E_Z = 91.2$, 200, 360, and 500 GeV. These jet energies are typical of those expected at the ILC for $\sqrt{s} = 0.5 - 1.0$ TeV. For each set of events, the rms_{90} of the total reconstructed energy distribution was determined, where rms_{90} is the root-mean-squared deviation from the mean in the smallest energy range containing 90 % of the reconstructed events.

2.2.2 HCAL Depth

Good particle flow calorimetry requires that both the ECAL and HCAL are within the detector solenoid. Consequently, in addition to the cost of the HCAL, the HCAL thickness impacts the cost of the overall detector through the radius of the superconducting solenoid. The thickness of the HCAL determines the average fraction of jet energy contained within the calorimeter system. The impact of the HCAL thickness on particle flow performance is assessed by changing the number of HCAL layers in the LDCPrime model from 32 to 63. This corresponds to a variation of $4.0 - 7.9\,\lambda_I$ ($4.8 - 8.7\,\lambda_I$) in the HCAL (ECAL+HCAL).

The study of the optimal HCAL thickness depends on the possible use of the instrumented return yoke (the muon system) to correct for leakage of high energy showers out of the rear of the HCAL. The effectiveness of this approach is limited by the fact that, for much of the polar angle, the muon system is behind the relatively thick solenoid ($2\lambda_I$ in the Mokka simulation of the detector). Nevertheless, to assess the possible impact of using the muon detector as a "tail-catcher", the energy depositions in the muon detectors were included in the PandoraPFA reconstruction. Whilst the treatment could be improved upon, it provides an estimate of how much of the degradation in jet energy resolution due to leakage can be recovered in this way. The results are summarised in Figure 2.2-1 which shows the jet energy resolution obtained from PandoraPFA as a function of HCAL thickness. The effect of leakage is clearly visible, with about half of the degradation in resolution being recovered when including the muon detector information. For jet energies of 100 GeV or less, leakage is not a major contributor to the jet energy resolution provided the HCAL is approximately $4.7\lambda_I$ thick (38 layers). However, for $180-250$ GeV jets this is not sufficient; for leakage not to contribute significantly to the jet energy resolution at $\sqrt{s} = 1$ TeV, the results in Figure 2.2-1 suggest that the HCAL thickness should be between $5.5 - 6.0\lambda_I$ ($43 - 48$ layers). To allow for uncertainties in the simulation of the longitudinal development of hadronic showers, and to ensure the detector is appropriate for collisions at 1 TeV, a 48 layer HCAL was chosen for ILD. This was also used for the LDC-based models discussed below.

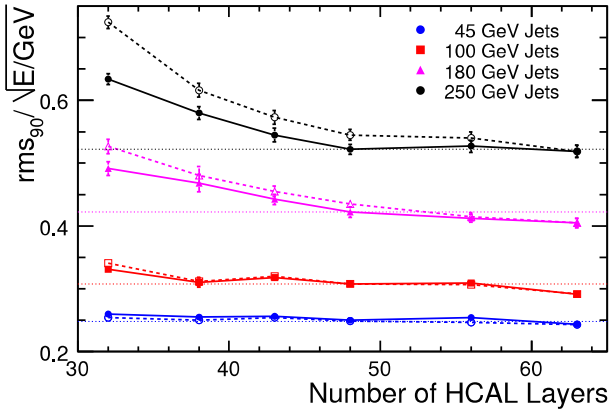

FIGURE 2.2-1. Jet energy resolutions (rms_{90}) for the LDCPrime detector model with different numbers of HCAL layers. Results are shown with (solid markers) and without (open markers) taking into account energy depositions in the muon detectors. All results are based on $Z \to u\bar{u}, d\bar{d}, s\bar{s}$ with generated polar angle in the barrel region of the detector, $|\cos\theta_{q\bar{q}}| < 0.7$.

2.2.3 Magnetic Field versus Detector Radius

The dependence of particle flow performance on B and R is studied in the region of parameter space close to the LDCPrime model. The LDCPrime model assumes a magnetic field of 3.5 T and an ECAL inner radius of 1820 mm. A number of variations on these parameters were studied: i) variations of both B and R with four sets of parameters considered, "LDC-like" (B=4.0 T, R = 1600 mm), "GLD-like" (B=3.0 T, R = 2020 mm), "Small" (B=4.5 T, R = 1420 mm), and "SiD-like" (B=5.0 T, R = 1280 mm); i) variations in the ECAL inner radius from 1280 − 2020 mm with B = 3.5 T; and iii) variations in B from 2.5 − 4.5 T with R = 1825 mm. In total thirteen sets of parameters were considered spanning a wide range of B and R. In each case particle flow performance was evaluated for 45, 100, 180, and 250 GeV jets. Table 2.2-2 compares the jet energy resolutions for LDC, LDCPrime and LDC4GLD models. The differences between these models is small, ∼ 5 %,. This is not surprising; the parameters of the LDC and GLD concepts on which these models are based were chosen such

Model			σ_E/E [%] versus E_{jet}			
Name	B/T	R/m	45 GeV	100 GeV	180 GeV	250 GeV
SiD-like	5.0	1.25	4.19 ± 0.06	3.72 ± 0.06	3.70 ± 0.07	3.94 ± 0.10
Small	4.5	1.42	3.90 ± 0.08	3.34 ± 0.07	3.54 ± 0.06	3.75 ± 0.08
LDC	4.0	1.60	3.82 ± 0.06	3.14 ± 0.06	3.26 ± 0.08	3.37 ± 0.07
LDCPrime	3.5	1.82	3.70 ± 0.06	3.07 ± 0.05	3.15 ± 0.07	3.30 ± 0.06
LDC4GLD	3.0	2.02	3.60 ± 0.05	2.97 ± 0.05	3.16 ± 0.06	3.32 ± 0.06

TABLE 2.2-2
Jet energy resolutions (rms_{90}) for different detector parameters. All results are based on $Z \to u\bar{u}, d\bar{d}, s\bar{s}$ events using scaled versions of the Mokka LDCPrime detector model. The results are quoted for the barrel region of the detector $|\cos\theta_{q\bar{q}}| < 0.7$.

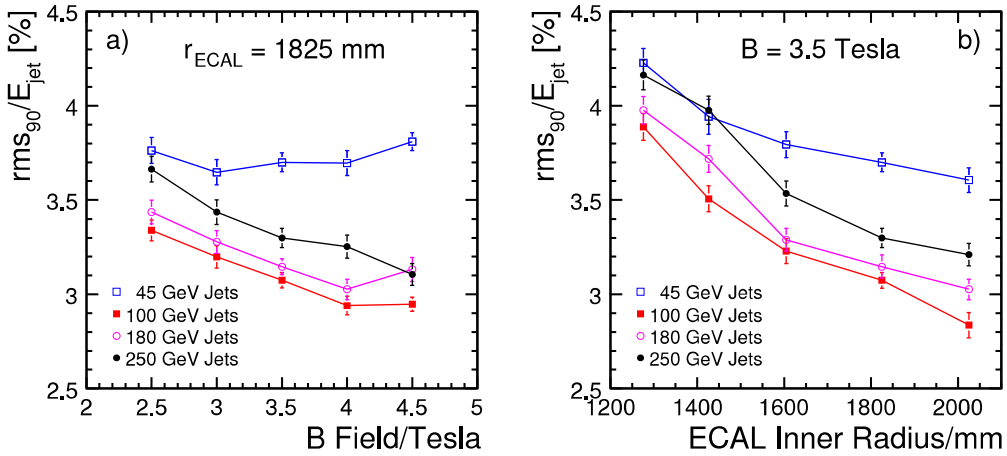

FIGURE 2.2-2. a) the dependence of the jet energy resolution (rms_{90}) on the magnetic field for a fixed ECAL inner radius (B=3.5 T corresponds to the LDCPrime model). b) the dependence of the jet energy resolution (rms_{90}) on the ECAL inner radius a fixed value of the magnetic field (R=1825 mm corresponds to the LDCPrime model).

that the smaller detector radius is compensated by a higher B. For the two smaller, higher B models listed in Table 2.2-2 degradations in performance are observed.

Figure 2.2-2 shows the dependence of the jet energy resolution ($\mathrm{rms}_{90}/\mathrm{E}_{\mathrm{jet}}$) on: a) magnetic field (fixed R) and b) ECAL inner radius (fixed B) for four different jet energies. For 45 GeV jets, the dependence of the jet energy resolution on B and R is weak; for these energies the intrinsic calorimetric energy resolution dominates, rather than the confusion term. For higher jet energies, where the confusion term dominates, the jet energy resolution shows a stronger dependence on R than B.

The jet energy resolutions listed in Table 2.2-2 and those shown in Figure 2.2-2 are reasonably well described by the function:

$$\frac{\sigma_E}{E} = \frac{21}{\sqrt{E/\mathrm{GeV}}} \oplus 0.7 \oplus 0.004E \oplus 2.1 \left(\frac{R}{1825\,\mathrm{mm}}\right)^{-1.0} \left(\frac{B}{3.5\,\mathrm{T}}\right)^{-0.3} \left(\frac{E}{100\,\mathrm{GeV}}\right)^{0.3} \%.$$

This is the quadrature sum of four terms: i) the estimated contribution to the jet energy resolution from the intrinsic calorimetric resolution; ii) the contribution from imperfect track reconstruction, estimated by comparing the jet energy resolutions with those using tracks obtained from the MC information; iii) leakage, estimated by comparing the jet energy resolutions with those for an $8\,\lambda_I$ HCAL; and iv) the contribution from confusion obtained empirically from a fit to the data of Table 2.2-2 and Figure 2.2-2. In fitting the confusion term, a power-law $\kappa B^{\alpha} R^{\beta} E^{\gamma}$ provides a reasonable parameterisation of the data [1]. From the perspective of the optimisation of the detector, these studies show that for the particle flow calorimetry using the PandoraPFA algorithm, that the confusion term scales as approximately $B^{-0.3}R^{-1}$. For particle flow performance (with the PandoraPFA algorithm) the detector radius is more important than the magnetic field. This forms part of the motivation for the choice of a large detector radius for the ILD conceptual design. Table 2.2-3 lists the

[1] The majority of the data points lie within 2.5σ of the parameterisation, the only exception being the 45 GeV and 100 GeV jet energy resolutions for the "SiD-like" detector where the fit underestimates the resolution.

relative values of $B^{0.3}R$ and relative jet energy resolutions from the parameterisation above for the LDC, LDCPrime and LDC4GLD detector models. The main conclusion of this study is that, in terms of particle flow performance, the differences between the LDC, LDCPrime, and LDC4GLD detector models are at the level of $\pm 5\,\%$, with the larger models being slightly prefered.

Model			$B^{-0.3}R^{-1}$	Relative σ_E/E versus E_{jet}			
Name	B/T	R/m	(relative)	45 GeV	100 GeV	180 GeV	250 GeV
LDC	4.0	1.60	1.08	1.02	1.04	1.05	1.06
LDC4GLD	3.0	2.02	0.95	0.99	0.97	0.96	0.96

TABLE 2.2-3
Expected jet energy resolutions (rms_{90}) of the LDC and LDC4GLD detector models relative to the LDCPrime resolution.

2.2.4 Detector Aspect Ratio

Although the cost of ILD will depend less strongly on length than on radius, it is, nevertheless, an important parameter in the detector optimisation. From the perspective of particle flow, the main effect will be on the performance of forward jets. For forward tracks, the importance of the B-field will be further diminished, and one might expect the confusion term to scale as L^{-1}, where L is the z-position of the endcap ECAL. Figure 2.2-3a shows the particle flow performance for jets in the endcap region ($0.80 < |\cos\theta_{\mathrm{q\bar{q}}}| < 0.95$). For particle flow reconstruction of forward jets it is beneficial to have the ECAL endcaps further from the interaction region. To maintain good jet energy resolution in the forward region of the detector the TPC drift length needs to be $\gtrsim 2000\,\mathrm{mm}$.

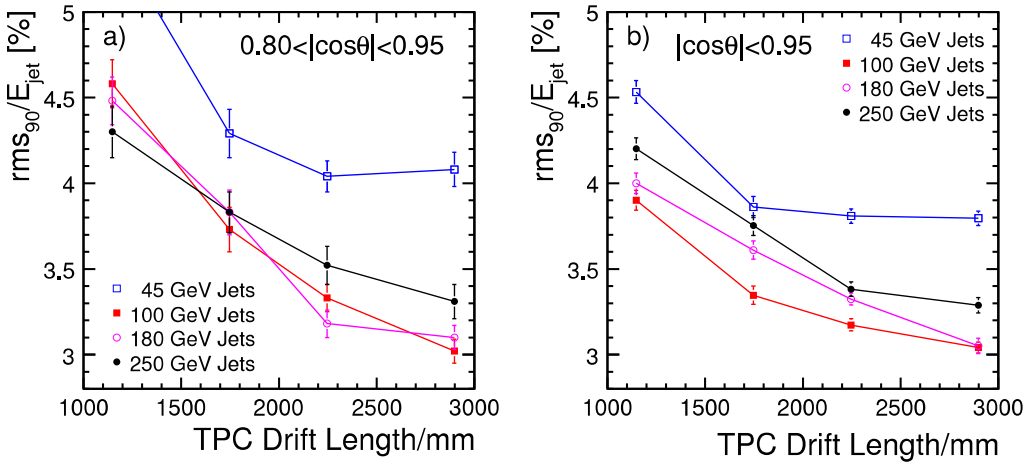

FIGURE 2.2-3. a) the dependence of the jet energy resolution in the "endcap" region ($0.80 < |\cos\theta_{\mathrm{q\bar{q}}}| < 0.95$) as a function of the TPC drift length in the LDCPrime model. b) the dependence of the jet energy resolution in the region ($|\cos\theta_{\mathrm{q\bar{q}}}| < 0.95$) as a function of the TPC drift length in the LDCPrime model.

Figure 2.2-3b shows the length dependence of the average jet energy resolution for jets with $|\cos\theta_{q\bar{q}}| < 0.95$. When considering all jets, the benefits to particle flow performance in going beyond a TPC drift length of 2200 mm are relatively small. From this study a TPC drift length of 2200 mm looks reasonable; the benefits of increasing the detector length are unlikely to justify the additional cost.

2.2.5 ECAL and HCAL Granularity

The dependence of particle flow performance on the transverse segmentation of the ECAL was studied using versions of the LDCPrime model with silicon pixel sizes of $5 \times 5\,\mathrm{mm}^2$, $10 \times 10\,\mathrm{mm}^2$, $20 \times 20\,\mathrm{mm}^2$, and $30 \times 30\,\mathrm{mm}^2$. The two main clustering parameters in the PandoraPFA algorithm were re-optimised for each ECAL granularity. The particle flow performance results are summarised in Figure 2.2-4a. For 45 GeV jets the dependence is relatively weak since the confusion term is not the dominant contribution to the resolution. For higher energy jets, a significant degradation in performance is observed with increasing pixel size. Within the context of the current reconstruction, the ECAL transverse segmentation has to be at least as fine as $10 \times 10\,\mathrm{mm}^2$ to meet the ILC jet energy requirement, $\sigma_E/E < 3.8\,\%$, for the jet energies relevant at $\sqrt{s} = 1\,\mathrm{TeV}$, with $5 \times 5\,\mathrm{mm}^2$ being preferred.

A similar study was performed for the HCAL using scintillator tile sizes of $1 \times 1\,\mathrm{cm}^2$, $3 \times 3\,\mathrm{cm}^2$, $5 \times 5\,\mathrm{cm}^2$, and $10 \times 10\,\mathrm{cm}^2$. The particle flow performance results are summarised in Figure 2.2-4b. From this study, it is concluded that the ILC jet energy resolution goals can be achieved with an HCAL transverse segmentation of $5 \times 5\,\mathrm{cm}^2$, although for higher energy jets there is a significant gain in going to $3 \times 3\,\mathrm{cm}^2$. There appears to be little motivation for $1 \times 1\,\mathrm{cm}^2$ over $3 \times 3\,\mathrm{cm}^2$ tiles.

2.2.6 ECAL and HCAL Detector Technology

The ILD concept incorporates two different technology options for both the ECAL and HCAL. The two ECAL technologies are: i) a Silicon-Tungsten (SiW) calorimeter where the baseline

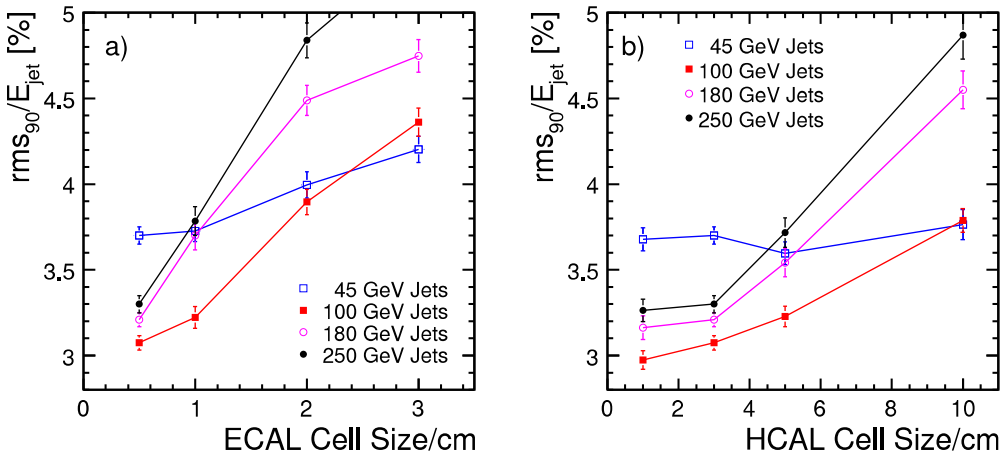

FIGURE 2.2-4. a) the dependence of the jet energy resolution (rms_{90}) on the ECAL transverse segmentation (Silicon pixel size) in the LDCPrime model. b) the dependence of the jet energy resolution (rms_{90}) on the HCAL transverse segmentation (scintillator tile size) in the LDCPrime model.

pixel size of $5 \times 5\,\mathrm{mm}^2$; and ii) a scintillator-Tungsten calorimeter where the $1 \times 4\,\mathrm{cm}^2$ scintillator strips in successive layers are perpendicular to each other with the aim of achieving a $1 \times 1\,\mathrm{cm}^2$ effective transverse granularity. The particle flow studies described above were obtained using the simulation of the SiW calorimeter. To extend these studies to the scintillator strip option requires additional step in the reconstruction, namely strip-based clustering. First studies[19] indicate that for 100 GeV jets the performance of the scintillator option with $1 \times 4\,\mathrm{cm}^2$ strips may approach that which would be obtained with a scintillator segmentation of $1 \times 1\,\mathrm{cm}^2$. However, at this stage, further work is needed to understand the limitations of the strip based ECAL for higher energy jets and whether it is possible to extend the approach to narrower strips to achieve an effective $5 \times 5\,\mathrm{mm}^2$ segmentation. The potential advantages of even finer segmentation, *e.g.* as provided by the MAPs-based ECAL, has yet to be studied in detail.

The two HCAL technologies under consideration are: i) an analogue steel-scintillator hadron calorimeter (AHCAL) with a tile size of $\sim 3 \times 3\,\mathrm{cm}^2$; and ii) a semi-digital calorimeter (DHCAL), *e.g.* using RPCs, with a readout pixel size of $1 \times 1\,\mathrm{cm}^2$ and a three level (2 bit per cell) readout. The particle flow studies described above used the AHCAL option. The particle flow performance of the semi-digital option is currently being studied in the context of the current PandoraPFA algorithm. Earlier studies (with the LDC detector model and a previous version of the PandoraPFA algorithm) found that the jet energy resolution for 100 GeV jets with a digital (single bit) readout was similar to that obtained with the AHCAL option. Further study is needed to establish the particle flow performance of the DHCAL option.

2.3 BACKGROUND CONSIDERATIONS

Beam-related backgrounds, and in particular e^+e^- pairs created by beam-beam interactions, are an essential input to the ILD design and optimisation. The e^+e^- pairs are produced at relatively low angles to the beam direction and spiral along the magnetic field lines parallel to the beam axis. As shown in Figure 2.3-5, the resulting pair-background tracks form a dense core with an approximately quadratic envelope. The radius of the dense core for a given value of z is roughly proportional to $\sqrt{B}$ [20]. The pair background determines the minimum radius of the beam pipe needed to avoid a large source of secondary background from electrons and positrons hitting the beam pipe. In turn, the radius of the beam pipe determines the radius of the innermost layer of the vertex detector, and consequently influences the impact parameter resolution for relatively low-momentum charged tracks. However, it has been shown [2], that if the magnetic field is $\gtrsim 3\,\mathrm{T}$, the required impact parameter resolution of $5\,\mu\mathrm{m} \oplus 10\,\mu\mathrm{m}/p(\mathrm{GeV})\sin^{3/2}\theta$ is achievable with a vertex detector layer thickness of $0.1 - 0.2\,\% X_0$/layer.

In terms of optimisation of ILD, the main effect of the pair background is to determine the inner radius of the vertex detector, which affects the impact parameter resolution and thus the flavour tagging performance. However, the difference between the radius of the core of the pair background between a 3T and a 4T magnetic field is only 15 %. In practice, the impact of the magnetic field on the inner radius of the vertex detector is less than this, as it is necessary to leave gaps between the dense core of the pair background and the beam pipe and between the beam pipe and the first layer of the vertex detector. These gaps are independent of the magnetic field, and when this is taken into account, the difference of inner radius of the vertex detector between a B-field of 3 T and 4 T is only $\sim 10\,\%$. The impact on the detector performance is discussed in the next two sections.

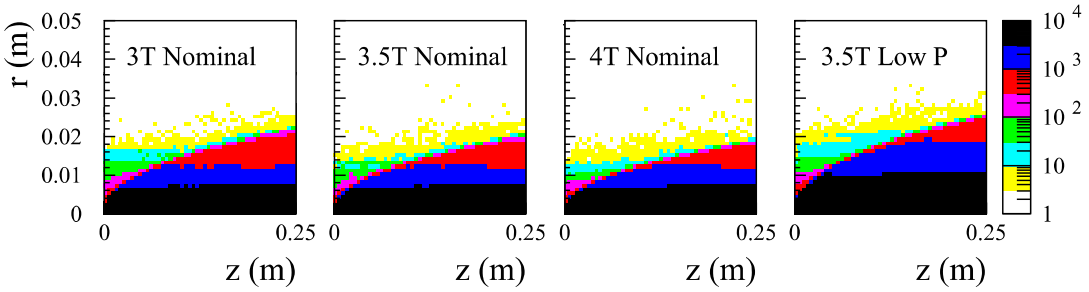

FIGURE 2.3-5. Track density of the e^+e^- pair background ($/cm^{-2}/BX$) with the nominal ILC beam parameters at $\sqrt{s} = 500\,\text{GeV}$ for the detector magnetic field of 3 T, 3.5 T, and 4 T. Also shown is the background with the lowP option for the ILC beam parameters at $\sqrt{s} = 500\,\text{GeV}$ with $B = 3.5\,\text{T}$.

Finally, it is worth noting that the inner radius of the vertex detector for the lowP option of the ILC machine parameters is about 20% larger than that for the nominal option. Therefore, it can be concluded that the machine parameters have a larger impact on the inner radius of the vertex detector than the magnetic field of the detector.

2.4 DETECTOR OPTIMISATION FOR TRACKING

The tracking system of the ILD detector concept consists of a vertex detector (VTX) and a large volume TPC, complemented by additional Silicon tracking layers (FTD/SIT). In addition, in the LDC-based models, silicon tracking layers immediately outside the TPC are considered (ETD and SET). The dependence of the performance of the tracking system on the magnetic field and detector size was an important consideration in optimising the ILD. Considerations of momentum resolution favour a larger detector and higher magnetic field. As discussed above, a higher magnetic field also allows the first layer of the vertex detector to be closer to the interaction point (IP). The optimisation of the tracking system is, again, a balance between the magnetic field and detector radius. The parameter space spanning the LDC (smaller R, higher B-field) and GLD (larger R, lower B) concepts is investigated using the six detector models summarised in Table 2.1-1.

2.4.1 Momentum Resolution

Figure 2.4-6(a) shows the $1/p_T$ resolution, as a function of p_T, for single muons in the GLD, GLDPrime and GLD4LDC models. The results were obtained using the Satellites Kalman Filter (Section 2.1.1). Figure 2.4-6(b) shows the relative $1/p_T$ resolution compared to the average of three detector models at a particular value of p_T, plotted as a function of p_T. Above approximately 50 GeV, the resolution obtained with the GLD4LDC model is ∼5 % worse than the larger detector models due to the shorter lever arm of the TPC. For lower energy tracks the situation is reversed with the higher magnetic field resulting in the resolution for 4 T being ∼10 % better than for 3 T. Similar results were obtained with the LDC-based models using Mokka and MarlinReco (Section 2.1.2). The relative performance does not depend strongly on angle. The differences in resolution for the range of B and R considered are small ($\lesssim 10\,\%$) compared to those arising from different layouts for the tracking system and the point resolutions of the components. For example, the use of hits in the silicon external

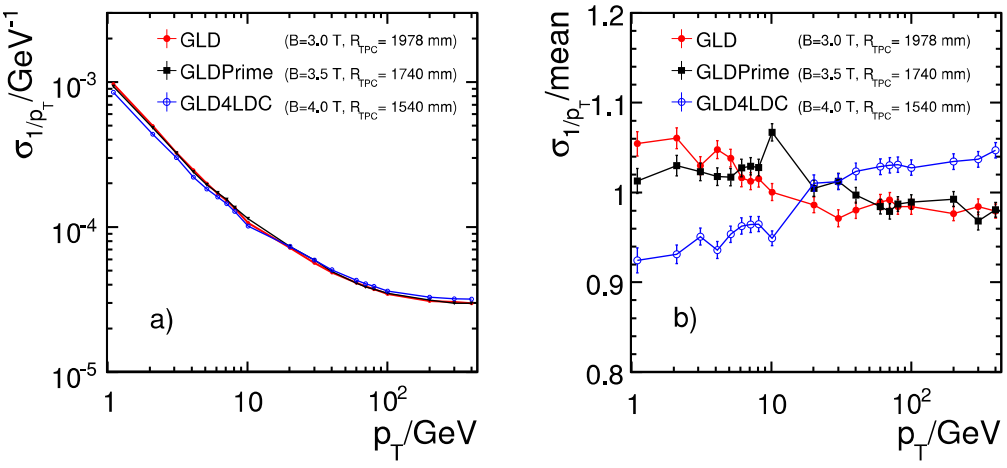

FIGURE 2.4-6. (a) σ_{1/p_T} for single muon tracks at 90° to the beam axis, as a function of transverse momentum, for the GLD, GLDPrime, and GLD4LDC models; and (b) the ratio of σ_{1/p_T} to the average of the three detector models as a function of transverse momentum. To avoid the TPC central membrane the generated muons were displaced from the IP by a few centimetres.

tracker (SET) outside the TPC in the LDCPrime model improves the momentum resolution by 15 % assuming an SET $r\phi$ hit resolution of 4 μm.

2.4.2 Impact Parameter Resolution

The impact parameter resolution, $\sigma_{r\phi}$, of the tracking system is an important input to the heavy flavour tagging capability of the detector. The most important detector considerations are the vertex detector design (point resolution and material budget) and the magnetic field which, as discussed in Section 2.3 affects the minimum distance of the first layer of the vertex detector from the interaction region, $R_{\rm min}$. Figure 2.4-7a shows $\sigma_{r\phi}$ as a function of $p_{\rm T}$ for the GDC-based detector models. The GLD4LDC model has the best resolution, because the higher B-field allows the innermost layer of the vertex detector to be closer to the interaction point (IP). However the differences between the detector models considered, Figure 2.4-7b, are relatively small $\lesssim 5-10\,\%$.

Figure 2.4-7c shows the $\sigma_{r\phi}$ resolution for 1 GeV muons for the GLD-based detector models, plotted as a function of the track angle. Whilst the higher magnetic fields are favoured, the differences between the detector models are $\lesssim 15\,\%$. For higher energy tracks, where the effect of multiple Coulomb scattering is negligible, the differences between the models are even smaller. Although the variations in magnetic field and the corresponding inner radii of the vertex detector lead to relatively small differences in impact parameter resolution, different detector layouts have a more significant impact. Figure 2.4-7d compares the impact parameter resolution for the GLDPrime and LDCPrime detector models. The GLDPrime detector assumes a vertex detector consisting of six layers arranged in three closely spaced doublets (see Section 4.1.4), whereas the LDCPrime model assumes five equally spaced layers. The three double layer layout results in a significantly better impact parameter resolution for high momentum tracks because it gives two, rather than one, high precision measurements close to the IP.

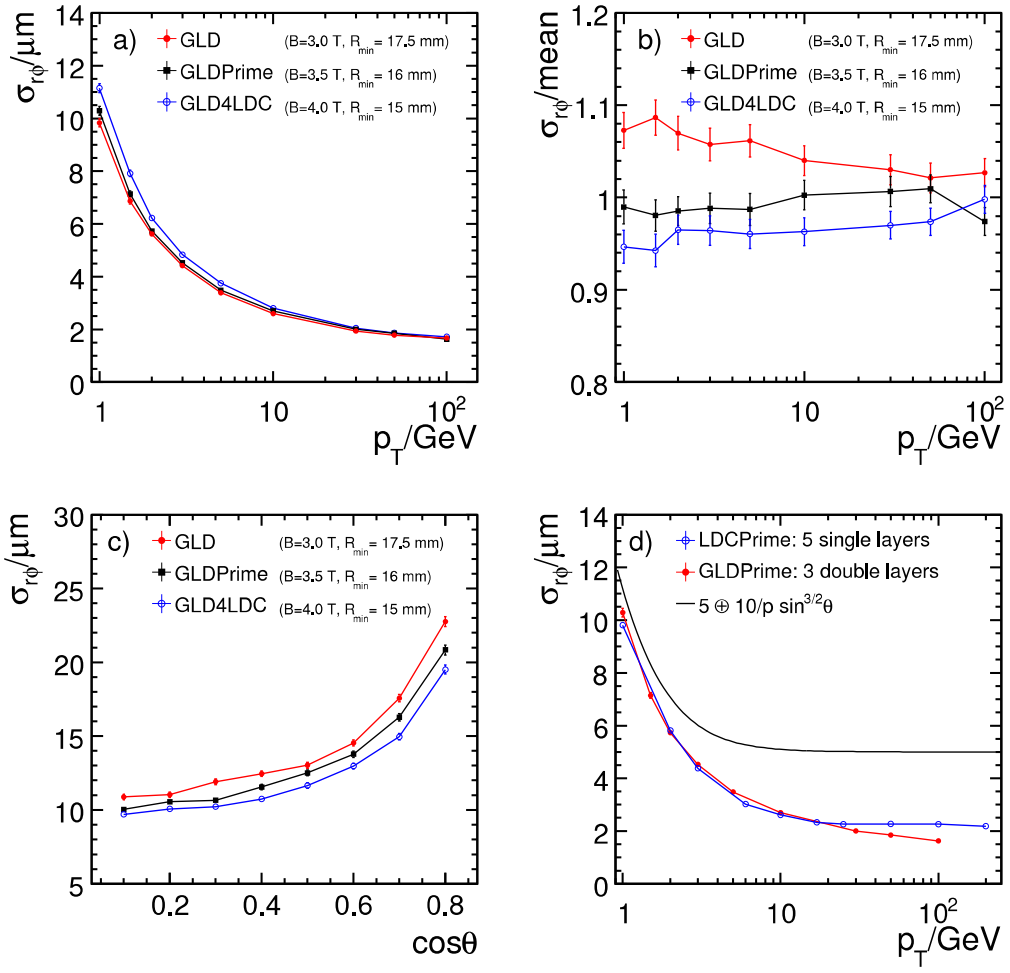

FIGURE 2.4-7. (a) $\sigma_{r\phi}$ as a function of p_{T} for GLD, GLDPrime, and GLD4LDC, and (b) the ratio of $\sigma_{r\phi}$ to the average of the three detector models. c) $\sigma_{r\phi}$ as a function of the track angle at the track energy of 1 GeV for GLD, GLDPrime, and GLD4LDC. d) the impact parameter resolution as a function of p_{T} for GLDPrime and LDCPrime. Also shown is the nominal ILC goal for impact parameter resolution.

2.4.3 Conclusions

For the range of B and R considered here, the differences in momentum resolution are $\lesssim 10\,\%$, with higher B-field preferred for low p_{T} tracks and a larger R preferred for high p_{T} tracks. The impact parameter resolution, $\sigma_{r\phi}$, is better for models with higher B as the first layer of the vertex detector can be placed closer to the IP. However, the differences in impact parameter resolution obtained with a 3 T and 4 T magnetic field are small, at most 15 % for low momentum tracks and $\lesssim 5\,\%$ for tracks above 2 GeV. It can be concluded that for the range of B and R spanned by the LDC and GLD detector concepts, the differences in impact parameter and momentum resolution are relatively small. It is also concluded that the tracking resolutions depend much more strongly on the subdetector technologies and tracking system layout than on the global parameters (B and R) of the detector.

2.5 FLAVOUR TAGGING

Heavy flavour tagging will be an essential tool in many physics analyses at the ILC. The flavour tagging performance depends primarily on the design of the vertex detector and, in particular, the impact parameter resolution. The flavour tagging performance is studied using MarlinReco for the full reconstruction of the simulated events and the sophisticated LCFIVertex package for heavy flavour tagging [21]. The LCFIVertex [17] flavour tagging uses three artificial neural networks (ANNs): i) a b-tag to discriminate b-quark jets from jets from charm and light quarks; ii) a c-tag to discriminate c-quark jets from b and light quark jets; and iii) a c/b-tag to discriminate between c-quark jets and b-quark jets. The ANNs use different sets of discriminant variables depending on whether either one, two, or more than two vertices are found in the jet. The ANN architecture is a multi-layer perceptron with $N = 8$ inputs, one hidden layer with $2N - 2$ nodes, and sigmoid activation functions. The weights were calculated using the back propagation conjugate gradient algorithm. Two of the most powerful inputs to the flavour tag are the joint likelihoods (in $r-\phi$ and in $r-z$) for all tracks in the jet to have originated from the primary vertex. The joint likelihoods depend on the respective $r-\phi$ and $r-z$ impact parameter significances of all the tracks in the jet. Consequently the impact parameter resolution of the vertex detector plays a central role in determining the flavour tagging performance. It was demonstrated in the previous section that the difference in $\sigma_{r\phi}$ in going from 3 T to 4 T is rather small. Consequently, one might expect the same to be true for flavour tagging performance.

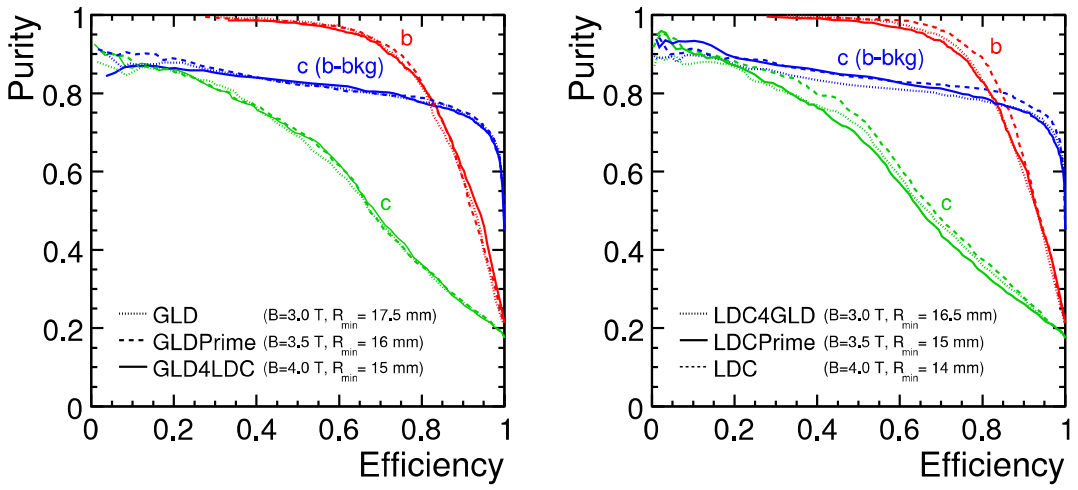

FIGURE 2.5-8. Flavour tagging performance for the (left) GLD-based and (right) LDC-based detector models.

The dependence of flavour tagging performance on the global detector parameters was investigated using the GLD- and LDC-based detector models. Separate ANNs were trained for each of the models. The samples used to evaluate the flavour tagging performance, which were generated with SM Z boson branching ratios, were independent of those used for the training. All the samples were generated at $\sqrt{s} = m_Z$. The results are shown in Figure 2.5-8. The observed differences in the flavour tagging performances between the GLD (LDC) models are $\lesssim 1\,\%$ ($\lesssim 4\,\%$). There is a preference for the 4.0 T configuration, in particular for

the b-tag at high efficiencies. However, the uncertainties on the efficiencies due to statistics and the ANN training procedure are $\sim 2\,\%$, and hence statistical significance of the observed differences are $\lesssim 2\sigma$. From this study it is concluded that the increased inner radius of the vertex detector when going from B=4 T to B=3 T, does not have a large impact on the flavour tagging performance of the detector.

2.6 PHYSICS PERFORMANCE

The previous sections of this chapter discuss the impact of the detector design on the low level measurements of jet energies, track momenta, impact parameters and flavour identification. Here the performance of the different detector models in Table 2.1-1 are compared for three physics analyses: the measurement of the Higgs mass, τ pair production and polarisation, and chargino/neutralino pair production.

2.6.1 Higgs Recoil Mass

One of the prime motivations for the unprecedented track momentum resolution at the ILC is the determination of the Higgs mass from the recoil mass distribution in $ZH \to \mu^+\mu^- X$ and $ZH \to \mathrm{e}^+\mathrm{e}^- X$ events. This sensitivity to this process was evaluated for the LDC, LDCPrime and LDC4GLD detector models. For this study only $\mathrm{e}^+\mathrm{e}^- \to ZZ \to \mathrm{e}^+\mathrm{e}^-/\mu^+\mu^- Z$ background was included. Figure 2.6-9 shows, for the LDCPrime model, the Higgs recoil mass distribution for selected events. To determine the Higgs mass and production cross section, the recoil mass distributions were fitted using a Gaussian for the peak region with an exponential component for the tails [22].

The results for the different detector models are summarised in Table 2.6-4. These numbers should not be compared with the physics sensitivity studies presented in Section 3.3.1 as only $\mathrm{e}^+\mathrm{e}^- \to ZZ \to \mathrm{e}^+\mathrm{e}^-/\mu^+\mu^- Z$ background is included and the events were generated with a different luminosity spectrum.

When interpreting the above results it is necessary to consider the relative importance of momentum resolution and the beam energy spread. For the assumed beam energy spread (a

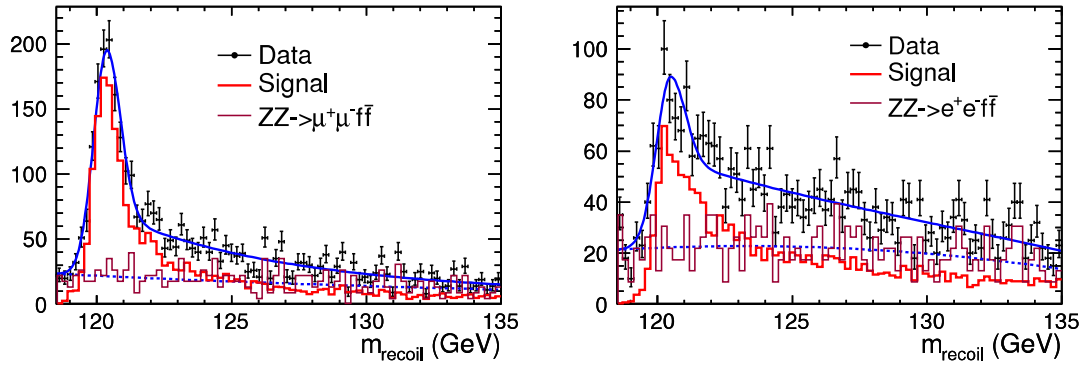

FIGURE 2.6-9. Distributions of the reconstructed Higgs recoil mass obtained with the LDCPrime model for (a) ZH $\to \mu^+\mu^- X$ and (b) ZH $\to \mathrm{e}^+\mathrm{e}^- X$. The events were generated with a top-hat beam energy distribution with a half width of 0.28% for the electron beam and 0.18% for the positron beam.

	$ZH \to \mu^+\mu^- X$		$ZH \to e^+e^- X$	
	$\Delta m_{\mathrm{recoil}}$	$\Delta\sigma$	$\Delta m_{\mathrm{recoil}}$	$\Delta\sigma$
LDCPrime	23 ± 0.4 MeV	0.28 fb	47±0.9 MeV	0.49 fb
LDC	23 ± 0.4 MeV	0.27 fb	47±0.9 MeV	0.52 fb

TABLE 2.6-4
The measurement precision of the Higgs recoil mass ($\Delta m_{\mathrm{recoil}}$) and cross section ($\Delta\sigma$) for ZH $\to$ $\mu^+\mu^- X$/e$^+$e^-X. The events were generated with a top-hat beam energy distribution with a half width of 0.28% for the electron beam and 0.18% for the positron beam.

top-hat distribution with half-widths 0.28 % and 0.18 % for the electron and positron beams respectively), the event-by-event recoil mass resolution in the peak region is ~ 400 MeV, where this includes contributions from the beam energy spread and from beamstrahlung. From MC studies, the other major contribution to the event-by-event recoil mass resolution arises, as expected, from the track momentum resolution. This is found to contribute ~ 350 MeV to the recoil mass resolution. For the detector models considered in this study, the differences in momentum resolution are $\lesssim 5\,\%$, for the relevant momentum range. Even these small differences are diluted by the contribution from the beam energy spread and, as verified in this study, significant differences in the m_{H} mass resolution are not expected.

2.6.2 Tau Pairs

The reconstruction of tau pair events at $\sqrt{s} = 500$ GeV provides a powerful test of a number of aspects of the detector performance, *e.g.* π^0 reconstruction and the tracking efficiency for nearby tracks in three-prong tau decays. The performances of the GLD, GLDPrime, GLD4LDC and LDCPrime models are compared for the measurement of the τ polarisation, P_τ which is primarily sensitive to the ability to resolve photons from π^0 decay from the charged hadron in $\tau \to \rho\nu$ decays. Figure 2.6-10 shows the reconstructed π^0 and $\rho^\pm$ invariant mass distributions used in the tau decay selections. The numbers of events in the π^0 mass peak reflect the efficiency for reconstructing both photons from $\pi^0 \to \gamma\gamma$ decays. The LDCPrime detector model gives the highest $\pi^0 \to \gamma\gamma$ reconstruction efficiency, demonstrating the advantages of smaller ECAL pixel size ($5 \times 5\,\mathrm{mm}^2$). For the GLD models, all with an ECAL pixel size of $10 \times 10\,\mathrm{mm}^2$, the π^0 reconstruction efficiency increases with detector radius due to the increased spatial separation of the two photons.

Table 2.6-5 summarises the impact of the different detector models on the P_τ measurement from from $\tau \to \pi\nu$ decays. The $\tau \to \pi\nu$ selection requires that a tau jet consists of a single track and at most 1 GeV of energy not assigned to the track. Cuts to remove $\tau \to e\nu\overline{\nu}$ and $\tau \to \mu\nu\overline{\nu}$ decays are also applied. The P_τ is determined from the cosine of the $\pi^\pm$ decay angle in the τ rest-frame (which is determined by the charged pion energy). The differences in the different detector models are most evident in the purities of the $\tau \to \pi\nu$ selection. The advantages of smaller ECAL pixels (LDCPrime compared to GLDPrime) are clear and it can be seen that higher purities are obtained for larger detector radii. However, similar sensitivities to P_τ are obtained from the $\tau \to \pi\nu$ channel. One should not draw too strong a conclusion from this as the measurement of P_τ from $\tau \to \rho\nu$ and $\tau \to a_1\nu$ decays could show a stronger dependence on the detector model.

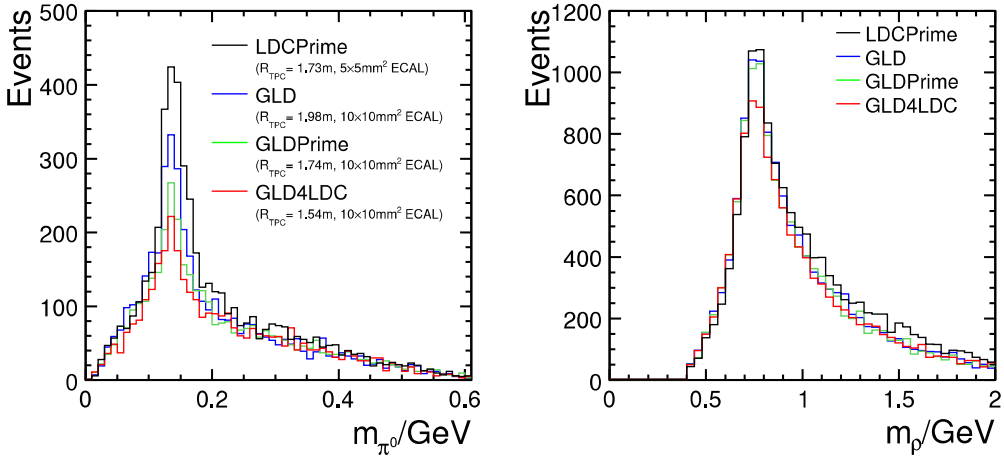

FIGURE 2.6-10. a) The reconstructed π^0 invariant mass distribution in the selected $\tau^+\tau^-$ events at $\sqrt{s} = 500\,\text{GeV}$. Only events where more that one photon is reconstructed are shown. b) The corresponding reconstructed $\rho^\pm \to \pi^\pm\pi^0$ mass distribution for decays where ≥ 1 photon cluster is reconstructed. For both plots the distributions include all tau decay modes.

Detector	ECAL/mm^2	R_{TPC}/m	Eff	Purity	σ_{P_τ}
GLD	10×10	1.98	84.5 %	85.7 %	0.0454 ± 0.0005
GLDPrime	10×10	1.74	85.2 %	83.6 %	0.0452 ± 0.0005
GLD4LDC	10×10	1.54	84.9 %	80.8 %	0.0460 ± 0.0006
LDCPrime	5×5	1.73	84.1 %	88.5 %	0.0430 ± 0.0005

TABLE 2.6-5
Summary of $\tau^\pm \to \pi^\pm\nu$ selection efficiencies and purities for events generated with the GLD, GLDPrime, GLD4LDC, and LDCPrime detector models. The efficiencies are calculated with with respect to the $\tau^+\tau^-$ selection and the purities only include the background from the different tau decay modes. The statistical uncertainties on the efficiencies and purities are all $\pm 0.5\,\%$. The uncertainty on the tau polarisation measurement assumes an electron-positron polarisation of $(-80\,\%, +30\,\%)$ and corresponds to 80 fb^{-1} of data.

2.6.3 Chargino and Neutralino Production

Chargino and neutralino pair production at $\sqrt{s}$ =500 GeV is studied in the context of the SUSY point-5 benchmark scenario. The main signal is jets plus missing energy from $\chi_1^+\chi_1^- \to \text{W}^+\text{W}^-\chi_1^0\chi_1^0$ and $\chi_2^0\chi_2^0 \to \text{ZZ}\chi_1^0\chi_1^0$. The process $\chi_2^0\chi_2^0 \to \text{ZZ}\chi_1^0\chi_1^0$ is the main background to study $\chi_1^+\chi_1^- \to \text{W}^+\text{W}^-\chi_1^0\chi_1^0$ and *vice versa*. The identification of the separate chargino and neutralino final states relies on the ability to distinguish W^+W^- from ZZ and thus is sensitive to the jet energy resolution of the detector. Figure 2.6-11a shows the reconstructed invariant masses of hadronically decaying $W^\pm$ and Z bosons from decays of $\chi_1^\pm$ and χ_2^0, respectively. Neutralino and chargino event samples were separated based on the consistency of the reconstructed di-jet masses with the Z and W boson hypotheses. The selection efficiencies for $\chi_1^\pm$ and χ_2^0 events for the GLD-based detector models are summarised in Table 2.6-6. The different detector models give statistically compatible selection efficiencies. This is consistent with the fact that the differences in the jet energy resolutions for the three

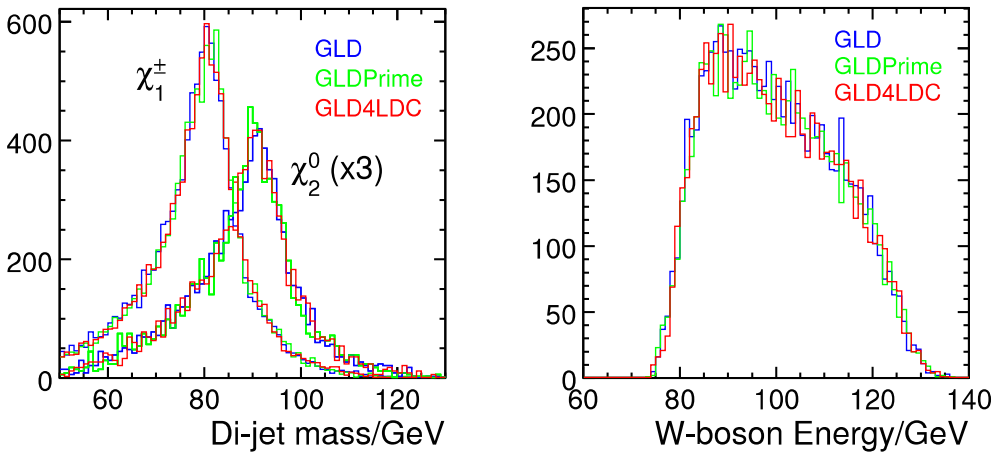

FIGURE 2.6-11. (a) The reconstructed masses of W and Z bosons from the decays of $\chi_1^\pm$ and χ_2^0. (b) The energy distribution of the reconstructed W bosons from $\chi_1^\pm$ decays.

	Chargino selection		Neutralino selection	
	Efficiency ($\chi_1^\pm$)	Efficiency (χ_2^0)	Efficiency ($\chi_1^\pm$)	Efficiency (χ_2^0)
GLD	$47.9 \pm 0.3\,\%$	$1.0 \pm 0.1\,\%$	$11.2 \pm 0.5\,\%$	$33.8 \pm 0.6\,\%$
GLDPrime	$48.4 \pm 0.3\,\%$	$1.0 \pm 0.1\,\%$	$11.4 \pm 0.5\,\%$	$33.3 \pm 0.6\,\%$
GLD4LDC	$48.8 \pm 0.3\,\%$	$1.1 \pm 0.1\,\%$	$11.4 \pm 0.5\,\%$	$34.1 \pm 0.6\,\%$

TABLE 2.6-6
The efficiency for $\chi_1^\pm$ and χ_2^0 selection.

detector models considered are at the level of $3-4\,\%$ for the jet energy range $50-100\,\mathrm{GeV}$ (Table 2.2-2).

Because $\chi_1^\pm \to W^\pm\chi_1^0$ and $\chi_2^0 \to Z\chi_1^0$ are two body decays, the masses of $\chi_1^\pm$, χ_2^0, and lightest SUSY particle (LSP), χ_1^0, can be derived by using the energy distributions of the W and Z bosons. The energy distributions of the reconstructed W bosons are shown in Figure 2.6-11b. The different detector models result in very similar distributions and, consequently, have the same sensitivity to the $\chi_1^\pm$, χ_2^0 and LSP masses.

2.7 CONCLUSIONS

The studies described above informed the choice of parameters for the baseline ILD concept. The conclusions of these studies are:

- **B-field (vertex reconstruction):** The radius of the beam background envelope scales as $B^{-0.5}$. This determines that the minimum acceptable inner radius of the vertex detector goes from $\sim 14\,\mathrm{mm} \to 16\,\mathrm{mm}$ for $B = 4\,\mathrm{T} \to 3\,\mathrm{T}$. The effect on impact parameter resolution is $\lesssim 10\,\%$ and the resulting differences in flavour tagging efficiency are small ($\sim 2\,\%$).
- **B-field versus Radius (particle flow):** The confusion term in particle flow reconstruction scales as R^{-1}. This can be partially compensated by the magnetic field,

although the dependence is weak, $B^{-0.3}$. For the entire range of detector parameters spanning the GLD and LDC concepts, the ILC jet energy resolution requirements can be met. The differences in particle flow performance between the LDC and GLD parameters are small, $\lesssim 6\,\%$, with the larger radius/lower field option being preferred.

- **B-field versus Radius (momentum resolution):** In terms of momentum resolution, the differences between the models considered are small $\lesssim 10\,\%$. For high p_{T} tracks, larger radius/lower field detector is preferred. For low p_{T} tracks the opposite is true. All detector models considered here meet the ILC momentum resolution goals.
- **TPC aspect ratio (particle flow):** the aspect ratio of the TPC ($R : z = 1 : 1.3$) used in the studies is close to optimum for particle flow; there is no significant advantage in a longer TPC and a shorter TPC would significantly degrade the performance in the forward region.
- **ECAL Segmentation (particle flow):** The ECAL pixel size should be no greater than $10 \times 10\,\mathrm{mm}^2$ in order to meet the ILC jet energy resolution goals for the jets relevant at $\sqrt{s} = 500\,\mathrm{GeV}$. Within the context of the current reconstruction, $5 \times 5\,\mathrm{mm}^2$ gives significant advantages over $10 \times 10\,\mathrm{mm}^2$, particularly for higher energy jets.
- **ECAL Segmentation (physics):** For the reconstruction of tau decays, a $5 \times 5\,\mathrm{mm}^2$ ECAL pixel size is favoured over $10 \times 10\,\mathrm{mm}^2$.
- **Physics Performance:** The models considered give comparable physics performance. This is not surprising; the differences in the underlying detector performance measures are small because the models trade-off R against B in such a way that *each* represents a reasonable detector choice.
- **HCAL Segmentation/Depth (particle flow):** For sufficient containment of jets at $\sqrt{s} = 500\,\mathrm{GeV}$, the HCAL should be between $5 - 6\lambda_I$. The baseline for the ILD was chosen to be $6\lambda_I$ to ensure good jet containment for the highest energy jets and to allow for possible differences between the simulation of hadronic showers and reality. For the current reconstruction, there appears to be no significant advantage in going below $3 \times 3\,\mathrm{cm}^2$.
- **Vertex Detector:** two detector layouts were considered: five single layers and six layers arranged in three doublets. Both conceptual designs meet the ILC goals for impact parameter resolution, with the doublet structure giving an impact parameter resolution which is better, particularly for high momentum tracks.
- **SiW versus Scintillator-W ECAL:** results from studies of the strip reconstruction and the resulting jet energy resolution of the Scintillator/Tungsten option, whilst promising, have yet to reach the level of sophistication where the performance of the strip based ECAL option can be fully evaluated. For this reason, the SiW ECAL is used in the simulation of the ILD for the physics studies in the next section.
- **AHCAL versus DHCAL:** results from studies of the digital HCAL option are not yet at the level where its performance has been demonstrated. For this reason the AHCAL option with $3 \times 3\,\mathrm{cm}^2$ tiles is used in the simulation of ILD.
- **Cost:** From the studies presented in this section it is clear any of the detector models listed in Table 2.1-1 are viable detectors for the ILC. For the same subdetector technologies, the differences in the costs for the detector parameters considered are estimated to be $\sim 10 - 20\,\%$; a large $B = 3\,\mathrm{T}$ detector is disfavoured on grounds of cost. However, given the large fluctuations in raw material costs (as seen in the last year) and the difficulty extrapolating detector sensor costs to the future, it is not yet possible to choose between the models on this basis.

2.8 CHOICE OF ILD PARAMETERS

On the basis of the considerations above, the ILD detector parameters (listed Table 2.1-1) are chosen to be close to those of the LDCPrime/GLDPrime models. The main arguments for the choices are as follows:

- **Choice of B-field:** The operational magnetic field is chosen to be 3.5 T, although it is assumed that the solenoid would be designed for 4.0 T to allow a safety margin in the mechanical design. This can be achieved without extrapolating significantly beyond the current CMS design. The arguments for a higher field are relatively weak: the benefits are marginal, and it would increase the cost of the detector. Whilst a lower B-field is not excluded, it is felt that until the likely ILC backgrounds and their impact on the ILD concept are better understood, it would be unwise to go to 3 T.
- **Choice of Radius:** The ECAL inner radius is chosen to be 1.85 m. The ILD concept is designed for particle flow calorimetry and the jet energy performance is the main motivation for this choice. For B=3.5 T the gain in going to an ECAL radius of 2.0 m is modest and may not justify the increase in cost. For a B=3.5 T, the ILC jet energy goals suggest that the radius should be greater than $1.5 - 1.6$ m. However, the studies presented above rely on the simulation of hadronic showers. By selecting a detector radius of 1.85 m, it is likely that the ILD concept will meet the ILC jet energy goals, even if the current performance estimates are on the optimistic side.
- **Choice of Sub-detector Technologies:** At this stage we are not in a position to choose the ECAL, HCAL and vertex detector technologies. All options are considered on an equal basis. Nevertheless, for the physics studies that follow it is necessary to define a baseline for the simulation. The six layer (three doublets) vertex detector layout is used on the basis that it gives the best impact parameter resolution. For the calorimetry, the SiW ECAL and the AHCAL are used in the simulation as they have been well studied and we are confident that they give the desired jet energy resolution. The strip-based ECAL and DHCAL will be actively supported in simulation and software with the intention of evaluating their ultimate performance.

The optimisation of the ILD parameters was performed in a rigorous manner using information from a number of detailed studies. On this basis, we are confident that the ILD concept is well optimised for physics at the ILC operating in the energy range 200 GeV−1 TeV.

CHAPTER 3

Physics Performance

The performance of ILD is established using a detailed GEANT4 model and full reconstruction of the simulated events. Both detector performance measures and physics analyses are studied. Whilst the simulation and reconstruction are not perfect, they are at least as sophisticated as those used in the majority of studies for previous large collider detector TDRs.

3.1 SOFTWARE FOR ILD PERFORMANCE STUDIES

To demonstrate the physics capabilities of ILD, more than 30 million Monte Carlo (MC) events have been fully simulated and reconstructed for the benchmark reactions [23] and other physics channels of interest at the ILC. Signal samples typically correspond to an integrated luminosity of 500 fb^{-1} or more. These are combined with sufficiently large sets of SM events for background estimation. The "simulation reference ILD detector model", ILD_00, is implemented in Mokka. The silicon based tracking detectors are modelled with the appropriate material thicknesses and support structures without specifying the exact readout technology. Instead, in the digitisation stage, simulated hits are smeared by the effective point resolutions listed in Table 3.1-1. These represent the most realistic estimates from the relevant subdetector R&D groups. The SiW option with 5×5 mm^2 transverse cell size and the Steel-Scintillator option with $3 \times 3\,\text{cm}^2$ tiles are used for the ECAL and HCAL respectively. As discussed in Section 2.2.6, these are the most mature of the technology options in terms of simulation and reconstruction; this does not imply any pre-decision on the ultimate technology choice. The main parameters of the ILD_00 model are listed in Table 2.1-1 and a drawing of this model is shown in Figure 3.1. Further details of the geometrical parameters can be found in [24].

	$\sigma_{r-\phi}/\mu\text{m}$	$\sigma_z/\mu\text{m}$		$\sigma_{r-\phi}/\mu\text{m}$	$\sigma_z/\mu\text{m}$
VTX	2.8	2.8	FTD	5.8	5.8
SIT/SET	7.0	50.0	ETD	7.0	7.0
TPC	$\sigma^2_{r\phi} = 50^2 + 900^2 \sin^2\phi + \left((25^2/22) \times (4/B)^2 \sin\theta\right) z\,\mu\text{m}^2$ $\sigma^2_z = 40^2 + 8^2 \times z\,\mu\text{m}^2$				

TABLE 3.1-1
Effective point resolutions used in the digitisation of the MC samples.

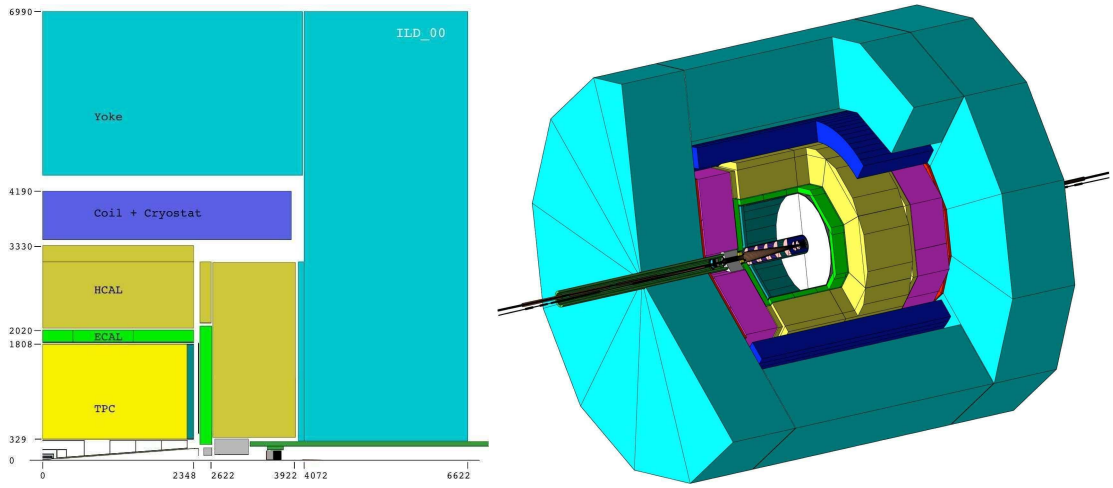

FIGURE 3.1-1. The ILD_00 detector model as implemented in Mokka. From the inside to the outside, the detector components are the: VTX, SIT, TPC, SET, ECAL, HCAL and Yoke. In the forward region the FTD, ETD, LCAL, LHCAL and BCAL are shown.

Most of the subdetectors in the ILD_00 model have been implemented including a significant amount of engineering detail such as mechanical support structures, electronics and cabling as well as dead material and cracks. This provides a reasonable estimate of the material budget and thus the effect of multiple scattering in the tracking detectors; it is also crucial for a realistic demonstration of particle flow performance. In the simulation, the vertex detector has a staggered layout of six 50 μm thick silicon ladders and corresponding support structures. The additional silicon tracking detectors, FTD/ETD (forward Si tracking) and SIT/SET (inner and outer Si tracking), are modelled as disks and cylinders respectively. The material thicknesses for these detectors give the effective radiation lengths listed in Table 4.2-3. The TPC model includes the material in the inner and outer field cage, this corresponds to a total of 4.5 % X_0 including the drift gas mixture. The hits from charged particles were simulated according to an end-plate layout with 224 rows of pads, 1 mm wide and 6 mm high. The ECAL simulation includes the alveolar structure and also the dead regions around the silicon pixels and between the modules. The HCAL simulation include steel and aluminium support structures which result in dead regions. The energy response of the scintillator tiles was corrected according to Birks' law. The simulation of the forward region includes realistic support structures and the shielding masks. All subdetectors are enclosed by a dodecagonal iron yoke, instrumented in the simulation with ten layers of RPCs. The superconducting coil and cryostat are simulated as a 750 mm thick aluminium cylinder, corresponding to 1.9 λ_I.

All events are reconstructed using the Kalman-Filter based track reconstruction in MarlinReco, the PandoraPFA particle flow algorithm and the LCFIVertex flavour tagging. The flavour tagging artificial neural networks (ANNs) have been trained using fully simulated and reconstructed ILD_00 MC events. The boost resulting from the 14 mrad crossing angle is taken into account in the analyses that use BCAL hit distributions as an electron veto.

3.2 ILD DETECTOR PERFORMANCE

3.2.1 ILD Tracking Performance

The tracking system envisaged for ILD consists of three subsystems each capable of standalone tracking VTX, FTD and the TPC. These are augmented by three auxiliary tracking systems the SIT, SET and ETD, which provide additional high resolution measurement points. The momentum resolution goal[25] is

$$\sigma_{1/p_T} \approx 2 \times 10^{-5}\,\mathrm{GeV}^{-1},$$

and that for impact parameter resolution is

$$\sigma_{r\phi} = 5\,\mu\mathrm{m} \oplus \frac{10}{\mathrm{p(GeV)}\sin^{3/2}\theta}\,\mu\mathrm{m}.$$

3.2.1.1 Coverage and Material Budget

Figure 3.2-2a shows, as a function of polar angle, θ, the average number of reconstructed hits associated with simulated 100 GeV muons. The TPC provides full coverage down to $\theta = 37°$. Beyond this the number of measurement points decreases. The last measurement point provided by the TPC corresponds to $\theta \approx 10°$. The central inner tracking system, consisting of the six layer VTX and the two layer SIT, provides eight precise measurements down to $\theta = 26°$. The innermost and middle double layer of the VTX extend the coverage down to $\theta \sim 16°$. The FTD provides up to a maximum of five measurement points for tracks at small polar angles. The SET and ETD provide a single high precision measurement point with large lever arm outside of the TPC volume down to a $\theta \sim 10°$. The different tracking system contributions to the detector material budget, including support structures, is shown in Figure 3.2-2b.

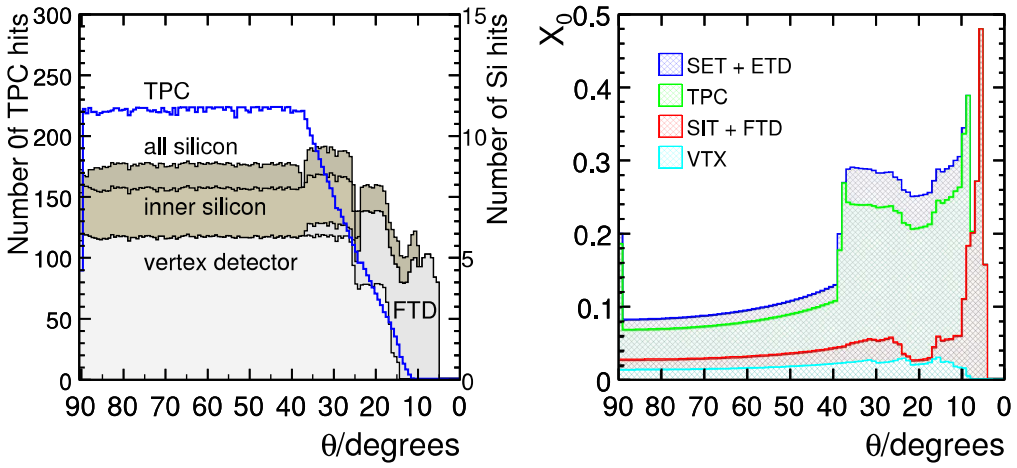

FIGURE 3.2-2. a) Average number of hits for simulated charged particle tracks as a function of polar angle. b) Average total radiation length of the material in the tracking detectors as a function of polar angle.

3.2.1.2 Momentum Resolution for the Overall Tracking System

The momentum resolution achieved with the ILD simulation and full reconstruction is shown in Figure 3.2-3a. The study was performed using muons generated at fixed polar angles of $\theta = 7°, 20°, 30°$ and $85°$, and the momentum was varied over the range $1 - 200\,\mathrm{GeV}$. For two polar angles, this is compared to the expected parametric form of, $\sigma_{1/p_T} = a \oplus b/(p_T \sin\theta)$, with $a = 2 \times 10^{-5}\,\mathrm{GeV}^{-1}$ and $b = 1 \times 10^{-3}$. As can be seen, at a polar angle of 85°, the required momentum resolution is attainable over the full momentum range from 1 GeV upwards, this remains true over the full length of the barrel region of the detector, where the TPC in conjunction with the SET is able to provide the longest possible radial lever arm for the track fit. For high momentum tracks, the asymptotic value of the momentum resolution is $\sigma_{1/p_T} = 2 \times 10^{-5}\,\mathrm{GeV}^{-1}$. At $\theta = 30°$, the SET no longer contributes, the effective lever-arm of the tracking system is reduced by 25 %. Nevertheless, the momentum resolution is still within the required level of performance. In the very forward region, the momentum resolution is inevitably worse due to the relatively small angle between the B-field and the track momentum.

3.2.1.3 Impact Parameter Resolution

Figure 3.2-3b shows $r\phi$ impact parameter resolution as a function of the track momentum. The required performance is achieved down to a track momentum of 1 GeV, whilst it is exceeded for high momentum tracks where the asymptotic resolution is $2\,\mu\mathrm{m}$. The rz impact parameter resolution (not shown) is better than $\sim 10\,\mu\mathrm{m}$ down to momenta of 3 GeV and reaches an asymptotic value of $< 5\,\mu\mathrm{m}$ for the whole barrel region. Because of the relatively large distance of the innermost FTD disk to the interaction point, the impact parameter resolution degrades for very shallow tracks, $\theta < 10°$. It should be noted that these studies do not account for the possible mis-alignment of the tracking systems.

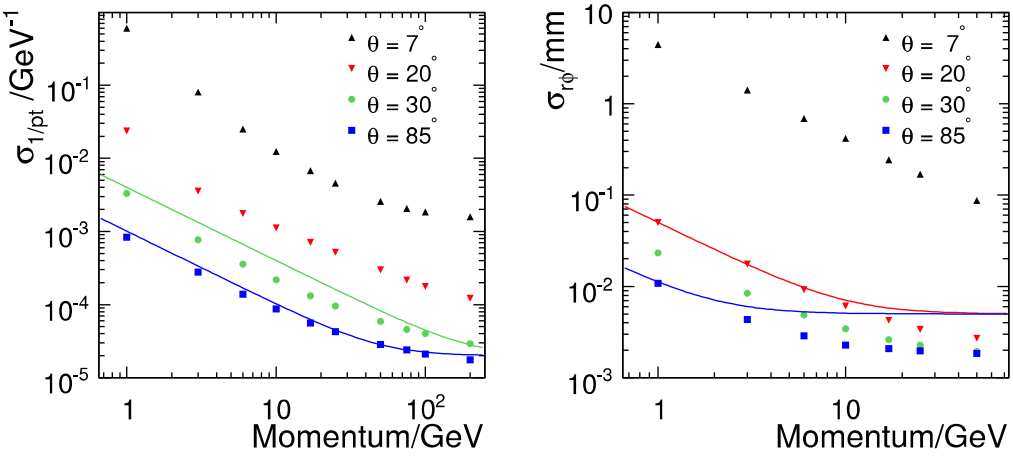

FIGURE 3.2-3. a) Transverse momentum resolution for muons plotted versus polar angle for four different simulated muon momenta. The lines show $\sigma_{1/p_T} = 2\times10^{-5} \oplus 1\times10^{-3}/(p_T \sin\theta)$ for $\theta = 30°$ (green) and $\theta = 85°$ (blue). b) Impact parameter resolution for muons versus polar angle for four different simulated muon momenta.

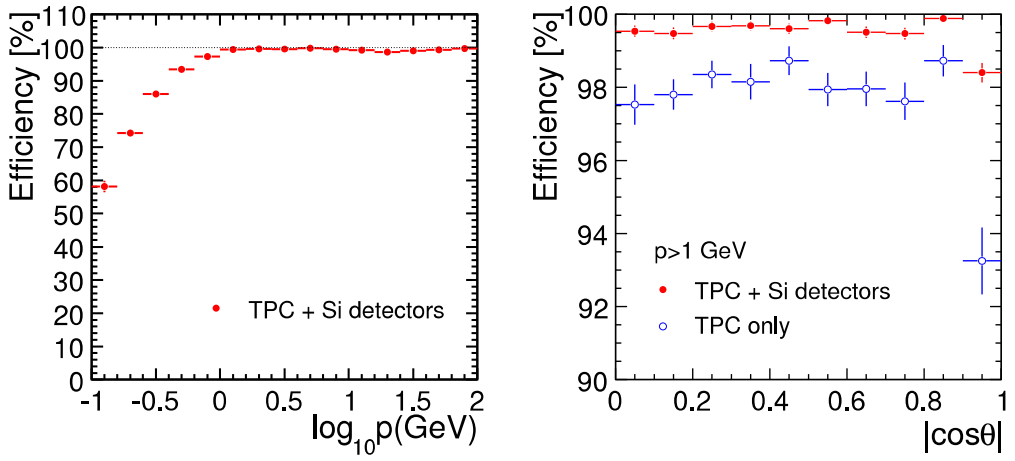

FIGURE 3.2-4. Tracking Efficiency as a function for $t\bar{t} \rightarrow$ 6 jets at 500GeV plotted against a) momentum and b) $\cos\theta$. Efficiencies are plotted with respect to MC tracks which leave at least 4 hits in the tracking detectors including decays and V^0s.

3.2.1.4 Tracking Efficiency

With over 200 contiguous readout layers, pattern recognition and track reconstruction in a TPC is relatively straightforward, even in an environment with a large number of background hits. In addition, the standalone tracking capability of the VTX enables the reconstruction of low transverse momentum tracks which do not reach the TPC. Hermetic tracking down to low angles is important at the ILC [26] and the FTD coverage enables tracks to be reconstructed to polar angles below $\theta = 7°$.

Figure 3.2-4 shows, as a function of momentum and polar angle, the track reconstruction efficiency in simulated (high multiplicity) $t\bar{t} \rightarrow$ 6 jet events at $\sqrt{s}$ =500 GeV. For the combined tracking system, the track reconstruction efficiency is approximately 99.5 % for tracks with momenta greater than 1 GeV across almost the entire polar angle range. The effects of background from the machine and from multi-peripheral $\gamma\gamma \rightarrow$ hadrons events are not yet taken into account; dedicated studies form part of the ongoing simulation R&D effort. Nevertheless, a study of the TPC reconstruction efficiency as a function of the noise occupancy is described in Section 4.3.3. This demonstrates that there is no loss of efficiency for 1 % noise occupancy.

3.2.2 ILD Flavour Tagging Performance

Identification of b-quark and c-quark jets plays an important role within the ILC physics programme. The vertex detector design and the impact parameter resolution are of particular importance for flavour tagging. The LCFIVertex flavour tagging (see Section 2.5) uses ANNs to discriminate b-quark jets from c and light-quark jets (b-tag), c-quark jets from b and light-quark jets (c-tag), and c-quark jets from b-quark jets (bc-tag).

The flavour tagging performance of ILD is studied [21] for the two vertex detector geometries considered, three double-sided ladders (VTX-DL) and five single-sided (VTX-SL) ladders. No significant differences in the input variables for the ANNs are seen for two geometries, and therefore the ANNs trained for the VTX-DL option were used for both VTX

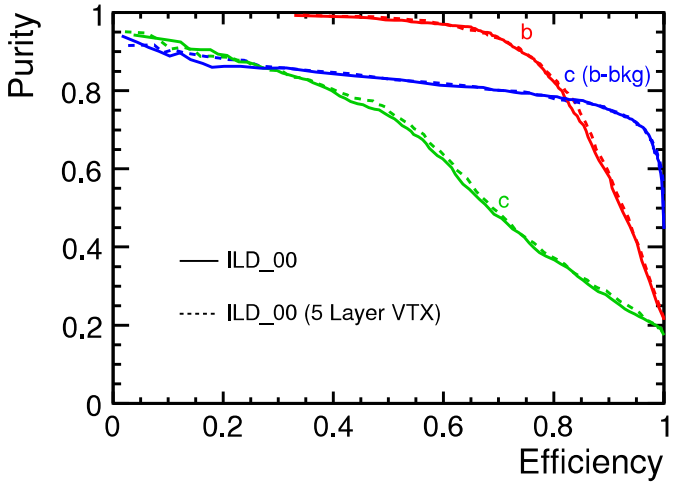

FIGURE 3.2-5. Flavour tagging performance of the ILD detector with three double-sided ladders (VTX-DL) and with five single-sided ladders (VTX-SL).

configurations. The samples used in the training consisted of 150000 $Z \to q\bar{q}$, at the Z pole energy, equally distributed among the three decay modes $q = b, c$ and light quarks. The test sample used to evaluate the flavour tagging performance was generated independently and consists of 10000 events of $Z \to q\bar{q}$ with the SM flavour mix of hadronic final states. The ILD flavour tagging performances for the two vertex detector options are shown in Figure 3.2-5. The performance differences between the two VTX geometries are small ($\lesssim 1\%$). Uncertainites due to the statistical fluctuations of the test sample and in those introduced in the ANN training are estimated to be $\lesssim 2\%$.

3.2.3 ILD Particle Flow Performance

Many important physics channels at the ILC will consist of final states with at least six fermions, setting a "typical" energy scale for ILC jets as approximately 85 GeV and 170 GeV at $\sqrt{s} = 500$ GeV and $\sqrt{s}$ =1 TeV respectively. The current performance of the PandoraPFA algorithm applied to ILD Monte Carlo simulated data is summarised in Table 3.2-2. The observed jet energy resolution (rms_{90}) is not described by the expression $\sigma_E/E = \alpha/\sqrt{E/\text{GeV}}$. This is not surprising, as the particle density increases it becomes harder to correctly associate the calorimetric energy deposits to the particles and the confusion term increases. The single jet energy resolution is also listed. The jet energy resolution (rms_{90}) is better than 3.8 % for the jet energy range of approximately $40 - 400$ GeV. The resolutions quoted in terms of rms_{90} should be multiplied by a factor of approximately 1.1 to obtain an equivalent Gaussian analysing power[27].

Figure 3.2-6 shows the jet energy resolution for Z →uds events plotted against the cosine of the polar angle of the generated $q\bar{q}$ pair, $\cos\theta_{q\bar{q}}$, for four different values of $\sqrt{s}$. Due to the calorimetric coverage in the forward region, the jet energy resolution remains good down to $\theta = 13°$ ($\cos\theta = 0.975$).

Jet Energy	raw rms	rms_{90}	$\mathrm{rms}_{90}/\sqrt{E_{jj}/\mathrm{GeV}}$	σ_{E_j}/E_j
45 GeV	3.3 GeV	2.4 GeV	25.0 %	(3.71 ± 0.05) %
100 GeV	5.8 GeV	4.1 GeV	29.5 %	(2.95 ± 0.04) %
180 GeV	11.2 GeV	7.5 GeV	40.1 %	(2.99 ± 0.04) %
250 GeV	16.9 GeV	11.1 GeV	50.1 %	(3.17 ± 0.05) %

TABLE 3.2-2
Jet energy resolution for Z →uds events with $|\cos\theta_{\mathrm{q\bar{q}}}| < 0.7$, expressed as, rms_{90} for the di-jet energy distribution, the effective constant α in $\mathrm{rms}_{90}/E = \alpha(E_{jj})/\sqrt{E_{jj}/\mathrm{GeV}}$, and the fractional jet energy resolution for a single jets, σ_{E_j}/E_j. The jet energy resolution is calculated from rms_{90}.

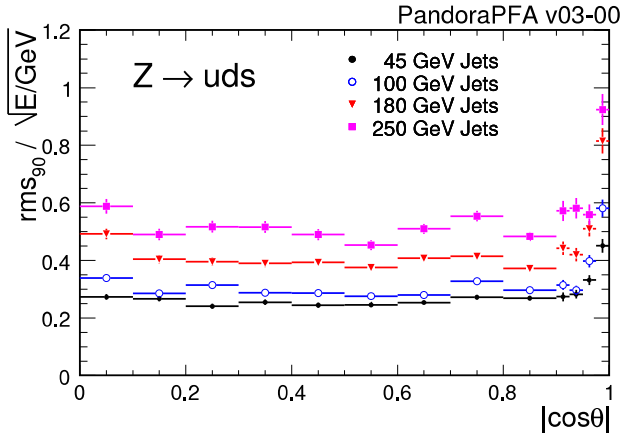

FIGURE 3.2-6. The jet energy resolution, defined as the α in $\sigma_E/E = \alpha\sqrt{E/\mathrm{GeV}}$, plotted versus $\cos\theta_{\mathrm{q\bar{q}}}$ for four different jet energies.

3.3 PHYSICS PERFORMANCE

The ILD detector performance has been evaluated for a number of physics processes. The analyses, described below, all use the full simulation of ILD and full event reconstruction. Jet finding is performed using the Durham algorithm[28] with the hadronic system being forced into the appropriate number of jets for the event topology. The benchmark physics analyses[23] are studied at $\sqrt{s} = 250\,\mathrm{GeV}$ and $\sqrt{s} = 500\,\mathrm{GeV}$. Unless otherwise stated, the results for $\sqrt{s} = 250\,\mathrm{GeV}$ ($\sqrt{s} = 500\,\mathrm{GeV}$) correspond to an integrated luminosity of $250\,\mathrm{fb}^{-1}$ ($500\,\mathrm{fb}^{-1}$) and a beam polarisation of $P(\mathrm{e}^+,\mathrm{e}^-) = (+30\,\%, -80\,\%)$.

3.3.1 Higgs Boson mass

The precise determination of the properties of the Higgs boson is one of the main goals of the ILC. Of particular importance are its mass, m_{H}, the total production cross section, $\sigma(\mathrm{e}^+\mathrm{e}^- \to \mathrm{HZ})$, and the Higgs branching ratios. Fits to current electroweak data[29] and direct limits from searches at LEP and at the Tevatron favour a relatively low value for m_{H}. Studies of these measurements with ILD are described below. A data sample of $250\,\mathrm{fb}^{-1}$ at $\sqrt{s} = 250\,\mathrm{GeV}$ is assumed and m_{H} is taken to be 120 GeV. For these values, the dominant Higgs production process is Higgs-strahlung, $e^+e^- \to \mathrm{ZH}$.

The Higgs boson mass can be determined precisely from the distribution of the recoil mass, m_{recoil}, in $\mathrm{ZH} \to \mathrm{e^+e^-}X$ and $\mathrm{ZH} \to \mu^+\mu^-X$ events, where X represents the Higgs decay products. The recoil mass is calculated from the reconstructed four-momentum of the system recoiling against the Z. The $\mu^+\mu^-X$-channel yields the most precise measurement as the $\mathrm{e^+e^-}X$-channel suffers from larger experimental uncertainties due to bremsstrahlung from the electrons and the larger background from Bhabha scattering events. The study is performed for two electron/positron beam polarisations: $P(e^+, e^-) = (-30\,\%, +80\,\%)$ and $P(e^+, e^-) = (+30\,\%, -80\,\%)$. In the simulation, the Gaussian energy spread for both incoming beams is 0.3%.

The first stage in the event selection is the identification of leptonically decaying Z bosons. Candidate lepton tracks are required to be well-measured, removing tracks with large uncertainties on the reconstructed momentum. Lepton identification is performed using the associated calorimetric information resulting in an event efficiency of 95.4 % for identifying both in $\mu^+\mu^-X$ events and 98.8 % for both electrons in $\mathrm{e^+e^-}X$ events. Candidate Z decays are identified from oppositely charged pairs of identified leptons within a mass window around m_Z. Background from $\mathrm{Z} \to \ell^+\ell^-$ is rejected using cuts on the transverse momentum of the di-lepton system and the acollinearity of the two lepton tracks. Additional cuts reject $\mathrm{Z} \to \ell^+\ell^-$ events with initial and final state radiation. The backgrounds from $e^+e^- \to \mathrm{ZZ}$ and $e^+e^- \to \mathrm{W^+W^-}$ are reduced using a multi-variate likelihood analysis based on the acoplanarity, polar angle, transverse momentum and the invariant mass of the di-lepton system.

The reconstructed m_{recoil} distributions are shown in Figure 3.3-7. The combination of signal and background is fitted using a function which assumes a Gaussian-like signal and that the background can be approximated by a polynomial function. The results of the fit for m_{H} and $\sigma(\mathrm{e^+e^-} \to \mathrm{ZH})$ are listed in Table 3.3-3. Also shown are the results obtained when assuming the SM decay modes and branching fractions. In this case, labelled "Model Dependent", the background is further reduced by requiring charged particle tracks in addition to those generated by the Z boson decay products.

From Figure 3.3-7 and Table 3.3-3 the following conclusions can be drawn: i) using the

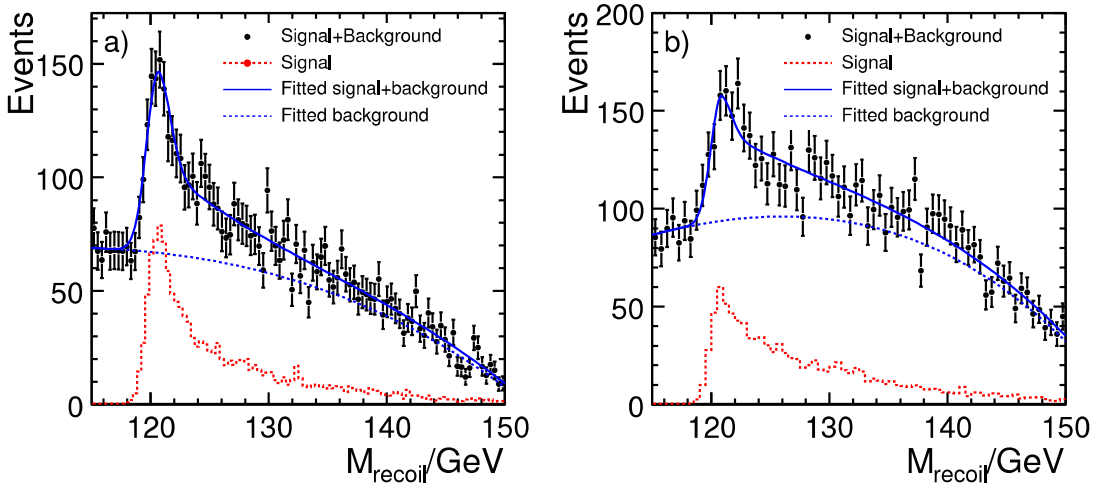

FIGURE 3.3-7. Results of the model independent analysis of the Higgs-strahlung process $\mathrm{e^+e^-} \to \mathrm{HZ}$ in which a) $\mathrm{Z} \to \mu^+\mu^-$ and b) $\mathrm{Z} \to \mathrm{e^+e^-}$. The results are shown are for the $P(e^+, e^-) = (+30\,\%, -80\,\%)$ beam polarisation.

Analysis	Polarisation (e^-, e^+)	Channel	σ_{m_H}	Cross section	
Model Independent	(+80 %, −30 %)	$\mu^+\mu^- X$	90 MeV	±0.50 fb	(7.0 %)
		$e^+e^- X$	182 MeV	±0.87 fb	(12.2 %)
	(−80 %, +30 %)	$\mu^+\mu^- X$	85 MeV	±0.70 fb	(6.6 %)
		$e^+e^- X$	150 MeV	±1.15 fb	(9.8 %)
Model Dependent	(+80 %, −30 %)	$\mu^+\mu^- X$	84 MeV	±0.45 fb	(6.4 %)
		$e^+e^- X$	204 MeV	±0.74 fb	(10.3 %)
	(−80 %, +30 %)	$\mu^+\mu^- X$	77 MeV	±0.55 fb	(5.4 %)
		$e^+e^- X$	135 MeV	±0.85 fb	(8.0 %)

TABLE 3.3-3
Expected statistical uncertainties on m_H from the recoil mass distribution in Higgs-strahlung events where the Z decays into either e^+e^- or $\mu^+\mu^-$. Results are listed for both the model independent and model dependent analyses. Also listed are the experimental uncertainties on the Higgs-strahlung cross section. The results are given for two different beam polarisations.

recoil mass distributions in the $e^+e^- X$ and $\mu^+\mu^- X$ final states, m_H can be determined with a statistical uncertainty of about 70 MeV and the Higgs-strahlung cross section can be measured with a precision of about 5%; ii) the precision on m_H obtained in the $e^+e^- X$ channel is approximately a factor two worse than that obtained from the $\mu^+\mu^- X$ channel; iii) for the current analysis, the reduction in background in the Model Dependent analysis reduces the error on m_H by $\sim 10\,\%$.

3.3.1.1 Influence of Beam Energy Uncertainties

The width of the peak of the recoil mass distribution is a convolution of the detector response and the luminosity spectrum of the centre-of-mass energy from the intrinsic beam energy spread and beamstrahlung. For the $\mu^+\mu^- X$ channel, the contribution from the detector response is primarily due to the momentum resolution, whereas for the $e^+e^- X$ channel bremsstrahlung dominates. Figure 3.3-8 shows the recoil mass spectrum for the $\mu^+\mu^- X$ channel obtained from the generated four momenta of the muon pair compared to that obtained from the reconstructed momenta. The detector response leads to a relatively small additional broadening of the recoil mass peak; an increase from 730 MeV to 870 MeV. Hence, for the beam energy spectrum used in the simulation, the dominant contribution to the observed width of the $\mu^+\mu^- X$ recoil mass arises from the incoming beams rather than the response of ILD. It should be noted that the differences between the above results and those of Section 2.6.1 are mainly caused by the different sets of beam parameters used in the event generation. Here the beam energy spreads are Gaussians with width 0.3 % and the beamstrahlung spectrum is broader than that used in Section 2.6.1. This issue will be investigated in future studies.

3.3.2 Higgs Boson Branching Fractions

The determination of the Higgs boson branching fractions is central to the ILC physics programme. In the context of the SM, this allows a test of the hypothesis that the strength of the Higgs coupling depends linearly on the particle masses. The statistical uncertainties on the branching ratios are estimated, for an integrated luminosity of $250\,\mathrm{fb}^{-1}$ at $\sqrt{s} = 250\,\mathrm{GeV}$, based on the analysis of the Higgs-strahlung process $e^+e^- \to ZH$ for the three possible Z

CHAPTER 4

The ILD Sub-Detector Systems

The ILD detector is strongly influenced by two basic assumptions about experimentation at a linear collider: particle flow as a way to reconstruct the overall event properties, and high resolution vertexing. Particle flow calorimetry requires a reliable and redundant tracking system which enables charge particle momenta to be reconstructed with high precision, and in particular, with very high efficiency. ILD is built around a calorimeter system with very good granularity both in the transverse and in the longitudinal direction, and a combination of Silicon and gaseous tracking systems. Vertexing, the other great challenge, is addressed by a high precision pixelated detector very close to the interaction point.

In this section the different sub-detectors are described in more detail, proposed technological solutions are outlined, and necessary development work is highlighted, particularly where it is essential to advance the concept to a point where this detector could be built.

Development of technologies for a detector at a linear collider is an active field, with many ideas being pursued, and great advances in technology are being made. ILD therefore does not at this moment exclude any promising technology from its consideration. Wherever possible, ILD supports that more than one avenue is followed to eventually identify the best solution possible. Therefore, at this stage, all promising technologies are considered as possible candidates for the ILD detector. Consequently for a number of subdetectors more than one option are described.

4.1 VERTEX DETECTOR

The Vertex Detector (VTX) is the key to achieving very high performance flavour tagging by reconstructing displaced vertices. It also plays an important role in the track reconstruction, especially for low momentum particles which don't reach the main tracker or barely penetrate its sensitive volume because of the strong magnetic field of the experiment, or due to their shallow production angle.

The flavour tagging performance needed for physics implies that the first measured point on a track should be as close as possible to the IP. This creates a major technical challenge because of the rapidly increasing beam-related background when approaching the IP. The sensor technology best adapted to the high background environment is not yet defined. It is however clear that existing technologies are not able to satisfy all of the requirements defined by the physics goals (granularity, material budget) and those imposed by the running conditions near the IP (*e.g.* occupancy and radiation dose). Several alternative, innovative, pixel

technologies are being considered and actively developed to satisfy the VTX requirements.

The VTX flavour tagging performances relies on a low material budget for the detector sensors and the support structures. The VTX is also necessary in some physics studies to measure the vertex charge (the net charge of all tracks from the decay chain) which implies distinguishing between the tracks from the primary vertex and the decay chain. This is particularly challenging for low momentum tracks in the jet. Finally, secondary particle production and trajectory kinks due to secondary interactions with the detector material need to be mitigated because of their impact on the particle flow reconstruction. Minimising the VTX material budget therefore motivates an ambitious R&D programme.

4.1.1 Physics Driven Requirements and Running Constraints

To identify the flavor (b or charm) of heavy-flavor jets, to measure the associated vertex charge, and to recognize tau-lepton decays, the VTX design needs to be optimised in terms of single point resolution and distance between the first measured point of tracks and the IP. The high granularity necessary to achieve the single point resolution needs to be complemented with a particularly low material budget allowing high precision pointing with low momentum tracks. A high granularity is also required to separate neighboring tracks in a jet, a constraint which applies predominantly to the detector elements closest to the IP.

Following the usual convention, the performances of the VTX in terms of impact parameter resolution are summarised in a compact way by its well known gaussian expression:

$$\sigma_{ip} = a \oplus b/p \cdot \sin^{3/2}\theta \qquad \text{(i)}$$

The parameters a and b are required to be below 5 μm and 10 μm·GeV/c, respectively. Monte-Carlo studies show that these specifications are met with the following inputs:

- a single point accuracy of $\lesssim 3$ μm,
- a vertex detector geometry providing a first measured point of tracks at ~ 15 mm from the IP, combined with a lever arm between the first and last measured points of about 3 times this distance,
- a material budget between the IP and the first measured point restricted to a few per mill of radiation length.

The values of a and b significantly exceed those achieved so far, as illustrated by the comparison made in table 4.1-1, which provides values of a and b obtained with vertex detectors operated at LEP, SLC and LHC as well as planned at RHIC.

To achieve this new tagging performance standard, a beam pipe radius of 14 mm is envisaged, which is still compatible with the need to contain the core of the beam-related pair background within the vacuum pipe. The pipe is assumed to be made of machined beryllium, 250 μm thick, potentially covered with a 25 μm thin foil of titanium against background from synchrotron radiation. Beam-related background, which ultimately sets the performance limits for the VTX, is expected to be dominated by beamstrahlung e^+e^- pairs. Most of these have low transverse momentum and remain trapped inside the vacuum pipe by the 3.5 T solenoid field. Extensive Monte-Carlo simulations, based on the GuineaPig [53] and CAIN generators [54], were performed to estimate the rate of $e^{\pm}$ reaching the vertex detector. The predicted rates amount to $5.3/4.4 \pm 0.5$ hits/cm^2 per bunch crossing (BX) at 15/16 mm radii, including $e^{\pm}$ backscattered from elements located near the outgoing beam

Accelerator	a (μm)	b ($\mu m \cdot GeV/c$)
LEP	*25*	*70*
SLC	*8*	*33*
LHC	*12*	*70*
RHIC-II	*13*	*19*
ILD	< 5	< 10

TABLE 4.1-1
Values of the parameters a and b entering the expression of σ_{ip} foreseen for the ILD, compared to those achieved with past, present or upcoming experiments at existing colliders.

lines [55]. Since most of these $e^{\pm}$ have a transverse momentum close to the cut-off value of $\lesssim$ 10 MeV/c, they tend to penetrate the sensitive volume of the VTX sensors at rather shallow angle, and generate pixel clusters which are elongated in the beam direction. This feature may be used offline to reject a large fraction of the beamstrahlung clusters. It also impacts the radiation dose. The annual dose was calculated to be in the order of 500 Gy ionising dose per year, with a corresponding fluence of $\lesssim 10^{11}$ n_{eq}/cm^2 at 15 mm radius. To account for the limited accuracy of the simulated beamstrahlung $e^{\pm}$ rate, the latter was multiplied by a safety factor of 3 to derive the sensor specifications. Other backgrounds, such as photon and neutron gas, are expected to add marginal contributions. Overall, the annual radiation levels the sensors have to comply with are in excess of 1 kGy and of 10^{11} n_{eq}/cm^2.

Another environmental concern entering the specifications of the VTX is related to the electrical interference associated with leakage of the beam-related RF from ports used for beam position monitors and other equipment in the interaction region. Their potential effect is motivating specific (delayed) signal processing read-out architectures of the sensors, taking advantage of the ILC beam time structure.

4.1.2 Global Design Aspects

The VTX design is still evolving, but its prominent aspects are well defined. It is made of 5 or 6 cylindrical layers, all equipped with $\lesssim 50$ μm thin pixel sensors providing a single point resolution of 2.8 μm all over the sensitive VTX area (see sub-section 4.1.3.1). The innermost layer has a radius of 15-16 mm, a value for which the beam-related background rate is expected to still be acceptable. As a consequence, the innermost layer intercepts all particles produced with a polar angle (θ) such that $|\cos\theta| \lesssim 0.97$.

Two alternative geometries are being considered, one (called VTX-SL) featuring 5 equidistant single layers (i.e. equipped with one layer of sensors only), and an alternative option (called VTX-DL) featuring 3 double layers (i.e. each layer being equipped with two, $\lesssim 2$ mm apart, arrays of sensors). They are not associated with a specific sensor technology. The double layer option allows spatial correlations between hits generated by the same particle in the two sensor layers equipping a ladder, even if the occupancy is high. It is therefore more robust against (low momentum) beamstrahlung background. It is also expected to provide additional pointing accuracy. Moreover, it should facilitate the internal alignment, allowing the use of a large fraction of tracks traversing the overlapping bands of neighbouring ladders. Finally, it is expected to improve the modeling with tracks reconstructed at shallow angle in

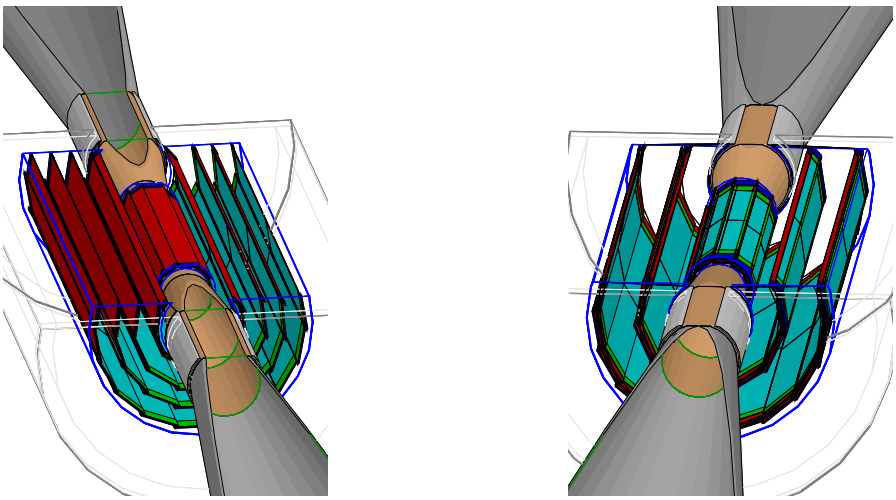

FIGURE 4.1-1. Vertex detector geometries of the two design options. Left: 5 single ladders (VTX-SL). Right: 3 double ladders (VTX-DL).

the very forward region. This geometry may however be less efficient in reconstructing long lived B mesons decaying outside of the beam pipe. It is also technically more challenging because of the additional difficulty to realise double ladders as compared to single ones. It may however be robust against mechanical distortions resulting from power pulsing the sensors inside the solenoid field. The two VTX geometries are displayed on figure 4.1-1. Some of their main geometrical parameters are listed in table 4.1-2.

	radius [mm]		**ladder length [mm]**		**read-out time [μs]**	
geometry	VTX-SL	VTX-DL	VTX-SL	VTX-DL	VTX-SL	VTX-DL
layer 1	15.0	16.0/18.0	125.0	125.0	25–50	25–50
layer 2	26.0	37.0/39.0	250.0	250.0	50–100	100-200
layer 3	37.0	58.0/60.0	250.0	250.0	100-200	100-200
layer 4	48.0		250.0		100-200	
layer 5	60.0		250.0		100-200	

TABLE 4.1-2
Radius and ladder length for each layer of the two vertex detector geometries. For the double layer option (VTX-DL), the radii are provided for each of both pixel arrays equipping a ladder.The read-out times are provided for each layer in the specific case of a continuous sensor read-out (see subsection 4.1.3).

The complete VTX-SL ladder thickness is equivalent to 0.11 % X_0, while the double ladders of VTX-DL represent 0.16 % X_0. These values assume 50 μm thin silicon pixel sensors. The length of the innermost ladder (125 mm) is limited due to the radial expansion of the pair background envelope as it diverges from the IP. It would shrink significantly when considering the so-called "low-P" option of the machine parameter. In this case, the innermost ladders should be shortened to < 100 mm and/or the inner radius should be increased in

ordre to accommodate the increased beam-beam disruption. The loss in physics performance consecutive to the geometrical acceptance shrinkage and to the potential impact parameter resolution degradation is still being evaluated.

Both device options are enclosed in a $\sim$ 500 μm thick (0.14 % X_0), 65 mm radius, cylindrical beryllium support. The latter is surrounded by a light foam cryostat (0.05 % X_0), complemented with a 0.5 mm aluminum foil (0.55 % X_0) which acts as a Faraday cage. The whole system, including support, cryostat and cage adds up to 0.74 % X_0. While the ladders of the three (resp. two) external layers of VTX-SL (resp. VTX-DL) are mounted on the beryllium support, the ladders composing the inner layers are supported by straight sections of the vacuum pipe.

The detector alignment is expected to proceed through two main steps. The ladders will first be aligned inside their layer. An overlap of $\lesssim$ 500 μm between the sensitive areas of neighbouring ladders is foreseen for this purpose. Tracks with momentum in excess of a couple of GeV/c traversing these overlapping bands will be used. Next the layers will be aligned with respect to the rest of the detector using straight tracks such as those of $\mu^+\mu^-$ final states.

The pros and cons of each design option are still being assessed. Moreover, the concept itself, which assumes extended cylinders, rather than shorter ones complemented with disks at small polar angle, is based on the present understanding of the minimal material budget which would separate the barrel from the disks. Depending on the evolution of technologies and materials, the choice between both alternatives may be reconsidered.

4.1.3 Pixel Technology and System Integration Studies

4.1.3.1 R&D on Pixels and Read-out Architectures

Intensive R&D has been under way for several years, addressing the numerous challenging issues underlying the vertex detector specifications. Because of the scale of the challenge and of its complexity, several alternative sensor technologies are being developed in parallel, aiming for the best suited ones. The goal of the development is to optimise the charge sensing system and the charge to electrical signal conversion, as well as the read-out, steering and control micro-circuits. The technologies presently concentrating most of the R&D effort within the ILD group are CMOS sensors [56, 57, 58, 59], DEPFETs [60, 61], FPCCDs [62, 63], and ISIS [60]. Since recently, CMOS sensors exploiting vertical integration technology [64] are also developed. Alternative technological approaches mentioned in [60] may also be considered, though not currently developed inside ILD group. The R&D achieved so far has already demonstrated that the goal of a single point resolution of ($\lesssim$ 3 μm), double hit separation of ($\lesssim$ 40 μm) and sensor thickness of ($\lesssim$ 50 μm) are achievable.

The most demanding requirement for all technologies is to comply with the occupancy generated by the beam related background in the innermost layers. Two alternative approaches are being investigated, one where the sensors are read out continuously, and one where the signal is stored during the whole train duration and read out during the beamless period separating two consecutive trains.

In the continuous read-out approach, most of the R&D effort is invested in achieving the low noise high read-out frequency required for the inner layers, while keeping the power consumption at an affordable level. Typical read-out time target values are summarised in table 4.1-2 for each layer. Present R&D achievements indicate that the upper bounds of each time interval can already be considered as within reach.

Power dissipation estimates, based on fabricated sensors and accounting for power cycling, were performed. It was assumed that the beam time structure can be used to suppress the power during a large fraction of the inter-train time by about two orders of magnitude, estimating to about $1 - 2$ milliseconds before and after the train the transient time needed to switch on and off all sensors in a well controlled way. In this case, Lorentz forces applied to the ladders are expected to remain acceptable. With a rather conservative duty cycle of 2% (while the machine duty cycle is 0.5%), the average power dissipation would amount to a few tens of watts only (e.g. 30 W for CMOS sensors [56]). Such values are compatible with modest cooling, based on air flow, which does not require introducing additional material in the VTX fiducial volume.

Power consumption may even be mitigated more with the delayed read-out approach because of the very low read-out clock frequency it allows for, a feature which also translates into reduced Lorentz forces on the ladders. Moreover, if the signal charge is converted into an electrical signal only after the end of the train (e.g. like in FPCCD or ISIS devices), immunity against EMI can be reinforced.

Most pixel technologies and read-out architectures still need at least a couple of years until all main VTX specifications have been addressed. The recently considered vertical integration approach, which may have the highest potential, is likely to need more time to reach maturity. It may be a technological solution for a second generation VTX, to be used a couple of years after the start of the ILC programme. It is in particular a promising solution for the machine operation near 1 TeV, where the beam-related background may call for sensors substantially faster than those needed at 500 GeV.

4.1.3.2 System Integration Studies

The R&D on the sensors and their read-out circuits is complemented with studies addressing their main system integration issues. One of the main aims of these studies is to tackle the design goal of $\lesssim 0.1$ % X_0 thickness per layer over their active area. Attempts are made to find materials which combine low density and high rigidity against potential vibrations generated by the air cooling system and by power cycling (temperature gradient, Lorentz forces). The latter also requires good thermal expansion compatibility between the support and the sensors. Low density materials were tested [60], such as silicon carbide foam, which have a thermal expansion coefficient close to silicon, and feature a density of a few per-cent only. They may actually also be used for the structural material of the entire VTX assembly.

Trials to use silicon as a support material are also made [61]. They consist in using the silicon substrate of the sensors, excavating the silicon bulk wherever it is not essential for the ladder stability. The latter is provided by "window frames" left after the bulk excavation. This approach is currently followed for the upgrade of the SuperBELLE vertex detector [65].

Finally, a third approach consists in extrapolating from the current state-of-the-art. It relies on the ladders equipping the upcoming PIXEL vertex detector of the STAR experiment at RHIC [66]. With a total material budget of ~ 0.3 % X_0, its concept may be extended to the ILD with an ultimate budget of $\lesssim 0.2$ % X_0.

4.1.4 Outlook

Definite choices concerning the sensor technology, the read-out architecture and the ladder design still have to wait until full-scale fully-serviced ladders, as well as still more realistic simulation studies are available. For instance, a detailed understanding of the handling of

the beam-related background will impact the maximal background rate acceptable, with direct consequences on the read-out architecture and the sensor technology. The validation of the VTX concept will follow, including the outcome of current studies of servicing issues, presumably around 2012.

4.2 SILICON TRACKING

The tracking system of the ILD has been optimised to deliver outstanding resolution together with excellent efficiency and redundancy. The choice of ILD is a combination of gaseous tracking, giving a large number of hits, and the redundancy this gives, with a sophisticated system of silicon based tracking disks and barrels. Together the system achieves excellent resolution, and covers the solid angle down to the very forward region.

An important consideration is the ability of the system to be calibrated to the desired precision. Here the combination of gaseous and silicon based tracking offers some unique advantages due to the very different nature of possible systematic distortions, and due to the possibility to cross-calibrate the different systems. For example, the Silicon tracker will help in monitoring possible field distortions in the TPC, as well as contributing to alignment and time stamping (bunch tagging). Silicon tracking is relatively easy to calibrate and as such it is expected to provide robustness, redundancy, and ease in the calibration of the overall tracking system.

The silicon tracking system of the ILD has been developed by the SiLC collaboration. Detailed descriptions of the wide ranging R&D activities conducted within the SiLC collaboration can be found in the latest documents and presentations issued by the SiLC Collaboration, and references therein [67, 68, 69, 70, 71, 72].

4.2.1 Baseline Design of the Silicon Trackers

Combined with the Silicon vertex detector and the central gaseous tracker TPC, a Silicon Tracking system is proposed for the ILD. It is based on modern Silicon detector technology, deep sub micron CMOS technology for the front-end (FE) electronics with a new on-detector electronics connection and new material technology for the support architecture. Special challenges for the ILD are a significant reduction in material compared to the most recent examples of large scale silicon detectors (*e.g.* LHC detectors), operating at very low power, and reaching excellent point resolution and calibration. The Silicon tracker is made of two sets of detectors:

- The first set is located in the central barrel and is made of the SIT (Silicon Internal Tracker), and the SET (Silicon External Tracker). Both devices have false double-sided Silicon strip detectors, together providing three precision space points.
- The second set is located in the forward region and is constituted of the FTD (Forward Tracking Detector) in the very forward region, and the ETD (end cap Tracking Detector), providing a space point between the TPC endplate and the calorimeter in the endcap region.

The complete silicon tracking system is implemented in the MOKKA simulation of the ILD, including estimates of support structures.

4.2.1.1 The Silicon Tracker in the Barrel: SET and SIT

The SIT is positioned in the radial gap between the vertex detector and the TPC. The role of the SIT is to improve the linking efficiency between the vertex detector and the TPC; it improves the momentum resolution and the reconstruction of low p_T charged particles and improves the reconstruction of long lived stable particles.

The SET is located in the barrel part between the TPC and the central barrel electromagnetic calorimeter (ECAL). The SET gives an entry point to the ECAL after the TPC end wall (3% X_0). It acts as the third Silicon layer in the central barrel and also improves the overall momentum resolution. The SIT and SET, in addition to improving momentum resolution (Fig. 4.2-3), provide time-stamping information for separation between the bunches and thus allowing the bunch-tagging of each event. These two central Silicon components may serve in monitoring the distortion of the TPC and for the alignment of the overall tracking.

4.2.1.2 The Endcap and Forward Silicon Tracking: ETD and FTD

The FTD is positioned in the innermost part of the tracking region, and covers the very forward region down to about 0.15 radians. In total seven disks are foreseen in this region.

The ETD is positioned between the TPC end cap and the end cap calorimeter system. The role of the ETD is to serve as entry point for the calorimeter and to improve the momentum resolution for the charged tracks with a reduced path in the TPC. Moreover it helps reducing the effect of the material of the TPC End Plates (currently estimated to be 15% X_0). It thus might improves the matching efficiency between the TPC tracks and the shower clusters in the EM calorimeter. It also contributes to extending the lever arm and angular coverage of the overall tracking system at large angle. Both the ETD and the FTD ensure the full tracking hermeticity.

4.2.2 Performances of the Silicon tracking system

The main detector performances of the Silicon tracking ILD system are summarized in terms of its contribution to i) full angular coverage, ii) momentum and impact parameter resolution, iii) calibration of distortions, iv) alignment, v) time stamping (bunch tagging), and vi) redundancy and robustness of the overall tracking system. Full simulation studies are being performed in order to best understand the performances of the Silicon tracking system in terms of momentum and spatial reconstruction and pattern reconstruction. These detailed simulations are completing the already available performance studies based on fast simulation (LiC Detector Toy Monte Carlo "LDT" and SGV) [67].

4.2.2.1 Angular Coverage

Combining the Silicon components with the vertex detector and the TPC ensures efficient tracking over the full angular coverage down to very small angles close to the beam. It helps in crucial regions such as: i) the transition from the central barrel to the End Cap region, ii) the end cap regions and iii) the very forward regions (Fig. 4.2-2).

4.2.2.2 Momentum and Impact Parameters Performances

To demonstrate the contribution of the various Si tracking components to the improvement of the overall tracking performances in terms of momentum and impact parameter resolution,

SIT characteristics (current baseline = false double-sided Si microstrips)					
Geometry			Characteristics		Material
R[mm]	Z[mm]	cosθ	Resolution R-ϕ[μm]	Time [ns]	RL[%]
165	371	0.910	R: σ=7.0,	307.7 (153.8)	0.65
309	645	0.902	z: σ=50.0	σ=80.0	0.65
SET characteristics (current baseline = false double-sided Si microstrips)					
Geometry			Characteristics		Material
R[mm]	Z[mm]	cosθ	Resolution R-ϕ[μm]	Time [ns]	RL[%]
1833	2350	0.789	R: σ=7.0,	307.7 (153.8)	0.65
1835	2350	0.789	z: σ=50.0	σ=80.0	0.65
FTD characteristics (current baseline = pixels for first 3 disks, microstrips for the other 4))					
Geometry			Characteristics		Material
R[mm]	Z[mm]	cosθ	Resolution R-ϕ[μm]		RL[%]
39-164	220	0.985-0.802			0.25
49.6-164	371.3	0.991-0.914			0.25
70.1-308	644.9	0.994-0.902			0.25
100.3-309	1046.1	0.994-0.959	σ=7.0		0.65
130.4-309	1447.3	0.995-0.998			0.65
160.5-309	1848.5	0.996-0.986			0.65
190.5-309	2250	0.996-0.990			0.65
ETD characteristics (current baseline = single-sided Si micro-strips, same as SET ones)					
Geometry			Characteristics		Material
R[mm]	Z[mm]	cosθ	Resolution R-ϕ[μm]		RL[%]
419.3-1822.7	2426	0.985-0.799	x:σ=7.0		0.65
419.3-1822.7	2428	0.985-0.799	y:σ=7.0		0.65
419.3-1822.7	2430	0.985-0.799	z:σ=7.0		0.65

TABLE 4.2-3
The projected values of basic SIT, SET, FTD, and ETD characteristics.

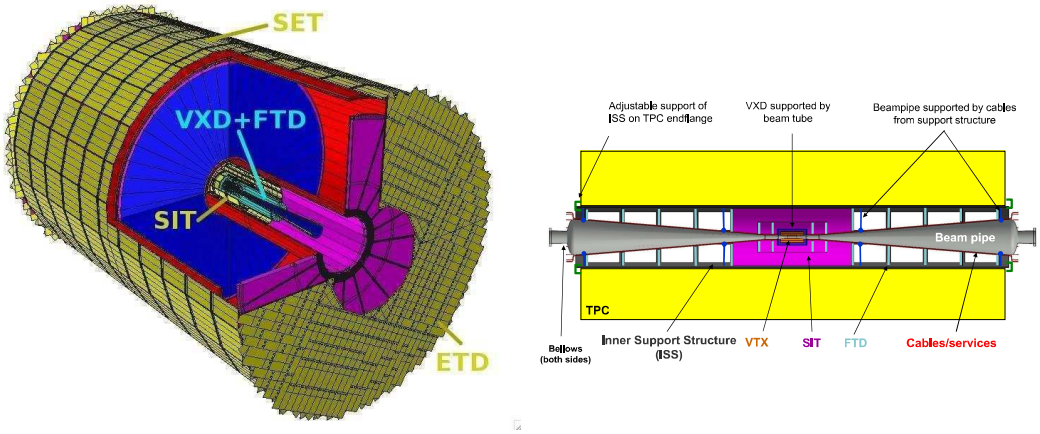

FIGURE 4.2-2. Silicon tracking components as described in the Table 4.2-3 (GEANT 4-based simulation). The plot on the right shows a side-view of the inner silicon tracking system, including the support structure.

a number of studies have been performed based on both fast simulation and the MOKKA-Marlin and GEANT 4 simulation. Some of the most relevant results (evaluation using fast Monte Carlo, muon tracking) are shown in Figure 4.2-3.

For tracks in the barrel region the present combined Silicon and TPC tracking system

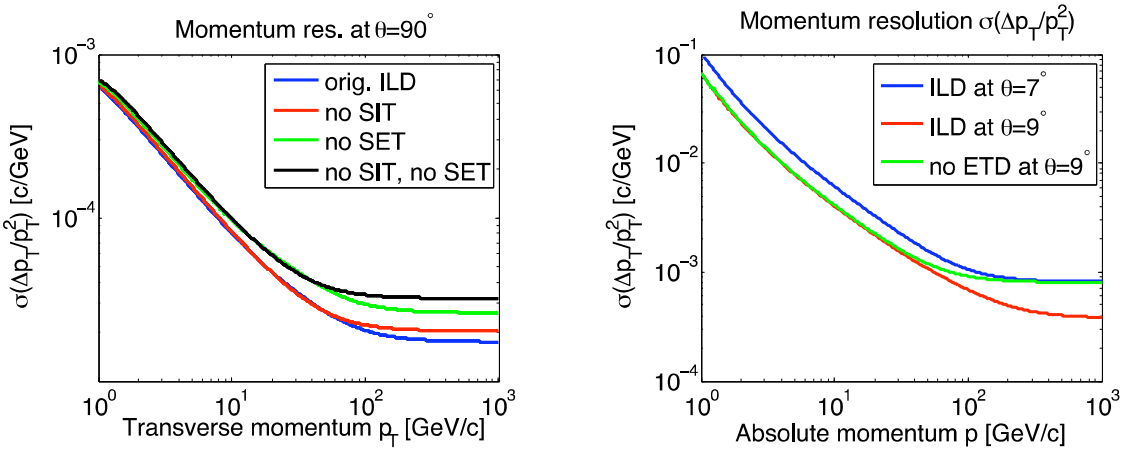

FIGURE 4.2-3. Left plot: barrel region, transverse momentum reduced resolution as function of p_T. Right plot: forward region, transverse momentum reduced resolution as function of absolute momentum p. The different scenarios are described in the text.

	VTX ($3 \times 3\mu m^2$)	VXD ($5 \times 5\mu m^2$)	VTX ($3 \times 3\mu m^2$) + SIT ($5 \times 10\mu m^2$)	VTX ($3 \times 3\mu m^2$) + SET ($5 \times 50\mu m^2$)
σ(R-ϕ)@ R = 150cm	1.3 cm	2.2 cm	0.6 mm	78 μm
σ(z)@ R = 50cm	35 μm	60 μm	16 μm	28 μm
σ(z)@ R = 100cm	77 μm	126 μm	39 μm	30 μm
σ(z)@ R = 118cm	118 μm	192 μm	50 μm	39 μm

TABLE 4.2-4
The precision of the extrapolated R-ϕ and z-coordinates for a 100 GeV track at $\theta = 90°$, at three radii in the TPC volume.

delivers an outstanding momentum resolution of $\sigma(\Delta p_T/p_T^2) < 2 \cdot 10^{-5}$ GeV 4.2-3(left). The plots compare four different arrangements: the ILD setup as described above (blue), a setup without the inner tracker SIT (red), a setup without the external tracker SET (green), and a setup without SIT and SET (black).

Figure 4.2-3(right) shows the momentum resolution for very forward going tracks, for three different angular ranges. While the addition of the silicon tracking system improves the momentum resolution, the impact parameter resolution remains virtually unchanged.

Table 4.2-4 offers an alternative illustration to the improvement generated by both SIT and SET on spatial resolution.

4.2.2.3 Distortion Monitoring and Handling

The Silicon trackers are mechanically stable devices which will help improve the absolute alignment of the overall tracking system, and of the ILD as a whole. This alignment is sensitive in particular to temperature fluctuations, which will need to be understood to the 2 μm level. These alignment systematics will be very different from the TPC ones. The TPC is sensitive to ambient temperature and to atmospheric pressure variations, to non-homogeneities in E and B fields, etc. In particular the E drift field in the TPC may depend on space charge transient effects due to variations in the machine backgrounds. The SIT and SET give an independent and effective means to monitor accurately such effects on real data.

Experience at LEP has shown that this capability gives an invaluable redundancy during data analysis, and a unique mean to disentangle and understand anomalous behaviours. It is a necessary complement to the unique pattern recognition capabilities of the TPC.

4.2.2.4 Electronic Time Stamping

Based on the performances of the front end (FE) chip currently developed, currently a bunch crossing tagging with a precision of 160 ns can be obtained corresponding to a shaping time around 0.5-0.7 μs and 8 sampling cells. This precision depends on the sampling frequency. A more refined estimate based on the Cleland and Stern algorithm [73], and function of the signal to noise, the number of samples, and the shaping time, indicates that the currently developed framework could allow identifying the bunch crossing with a resolution of order of 20 to 40 ns.

4.2.3 Calibration Procedures

The Front End Electronics as currently available in the current 130nm CMOS technology includes a full readout electronic chain with a high level digital control of the functionality of the overall chip. In particular a fully programmable test pulse system is included. It will allow calibrating and monitoring of this signal processing device and play a crucial role in the silicon DAQ.

Environmental conditions around the detector due to local temperature gradients, humidity changes, etc. will induce some instability of the support structures comparable in size to the precision of the detectors. Consequently, independent alignment systems monitoring these changes will be needed. For the case of silicon trackers one can profit from the weak (but non-zero) absorption of infrared light in Silicon and use laser beams as pseudo-tracks that traverse consecutive sensors.

For the SIT and FTD subdetectors, which have several Silicon layers, the alignment procedure is based on the use of their own tracking detectors as photo-sensors; the transmittance of Silicon to infrared beams compared to the existing AMS and CMS tracker systems can be improved by a further 20-30%, leading to a transmittance value between 70 to 80%. Resolutions on the order of 2 microns can be obtained with this procedure [74].

The SET and ETD are single layer detectors; the SET can be aligned with respect to fiducial marks on the outer cage of the TPC at the level of 100 microns by standard procedures. The monitoring of the SIT position could be done one order of magnitude better [75]. Similar procedures can be done for the ETD. Finally, tracks will be used for internal alignment at the precision level of few microns, by using adequate χ^2 minimisation algorithms already employed in the LHC and other experiments.

4.2.4 Silicon Tracker Material Budget

A crucial concern of the design of the silicon tracking system has been to minimise the material budget. New silicon sensors and modern material technology based on carbon fibre composite materials (CFC) provide optimal solutions for the silicon tracking components. New front end electronics based on DSM CMOS feature less power dissipation (see already achieved performance of the newly developed FE chip) and allow a direct connection onto the detector, thus removing the need for cooling. All these facts allow a reduction of the sensitive thickness of the sensors to at least 250 μm, or 0.25% X0. Engineering studies have

shown that a support structure for the envisioned silicon detectors equivalent to a 1 mm thick CFC layer are possible, corresponding to a contribution of 0.4%X0 per layer. Together with services etc a thickness of 0.65% X0 per layer seems in reach (see table 4.2-3). The final goal is 0.5% RL per layer in the innermost part of the detector, which will need further R&D. A further reduction might be possible if new sensor and support technologies become available.

4.2.5 Baseline construction and Integration of Silicon components

The baseline design to construct the ILD Silicon system is an unified design for all the components apart from the very small FTD disks. The SIT, SET and ETD components will be made of Silicon strip sensors with a unique sensor type. The current baseline are sensors of square shape from a 6″ wafer, 200μm thick, 50μm readout pitch (true pitch of 25μm). The modules will be made of one up to a few sensors depending on the location of the module in the detector. The readout chip will be directly connected onto the sensor. The chip will be made in deep sub-micron technology (current prototypes are in 130nm technology), most probably in 90 nm. It is a mixed analogue-digital FE and readout chip with a full processing of the analogue signal, long shaping time (1μs), sparsification, digitisation and a high level of digital processing allowing full programmability of the chip. A full prototype is presently developed [76]. The power dissipation of at most 1m W per channel is achieved and power cycling is included. The goal is to avoid a dedicated liquid cooling system, but instead to rely on a forced gas cooling as is also considered for the VTX and the TPC systems. Details of this however are not yet worked out.

The integration of the silicon tracking components depends critically on the neigbbouring detectors. The SET will be made of 24×2 identical super-modules, each covering 2.35×0.5 m^2 supported by a light structure made from composite material. The support structure will be supported from the TPC end-flange, and might also rest at intermediate z-positions on the TPC field cage. The two SIT layers will be made in the same way as the SET, namely 18 and 12 super-modules for the external and the innermost layers, respectively. Together with the outer four FTD disks the SIT layers will be supported by a CFC support structure, fixed to the TPC end-flange at their inner radius. The ETD, thanks to its XUV geometry is built in the same way as the barrel components and will be fixed to the electromagnetic end cap calorimeter.

The support architecture of SIT, SET and ETD will be designed in the same way focusing on robust, very light and easy to mount structures. The design for the FTD disks is currently based on pixels (same type as the vertex detector) for the first three disks and false double sided strips for the other four disks. These four disks will be made of trapezoidal sensors and altogether 16 petals as in the present ATLAS forward detector.

4.2.6 R&D needs and prospects for Silicon tracking

The Silicon technology for large-area tracking systems will continue to evolve over the next years because of the stringent needs of the Large Collider experiments (LHC upgrades, ILC and CLIC). The SiLC R&D collaboration takes an active part in these worldwide efforts dedicated to novel and high technology. The group will continue to develop novel sensors. Options include, as a first step, the edgeless planar micro-strip sensors followed by the 3D planar micro-strips sensors. The goal is to have thinner, lower voltage biased strip sensors and larger wafer size (8″). In addition, the application of pixel technology to at least dedicated regions of the Silicon tracking, including 3D based pixel technology is part of this

R&D objective. The ongoing development of Front End and readout electronics based on ASICs in very deep sub micron CMOS technology, with a high degree of processing of digital information on the detector, low noise, low power consumption, robustness (redundancy and fault tolerance), will be further pursued. New interconnection technologies of the ASIC directly onto the sensors by bump bonding and then by 3D vertical interconnect as well as new cabling techniques will be addressed. Challenging aspects on mechanics in order to build light, robust, and large area mechanical structures, with stringent mechanical constraints on alignment, stability (ex: push pull) and quality control will impact the final design and construction of these devices. A reduced material budget resulting in improved tracking performance, robustness, reliability, easy to build (and not expensive) are the main goals of this ambitious R&D program [67].

4.3 THE TIME PROJECTION CHAMBER

4.3.1 Motivation

The subdetectors for the linear collider detector must be designed coherently to cover all possible physics channels because the their roles in reconstructing these channels are highly interconnected. Two important aspects for tracking are, (a) precision-physics measurements require that the momentum of charged tracks be measured an order of magnitude more precisely than in previous experiments, and (b) high resolution measurements of the jet-energy using the particle-flow technique require efficient reconstruction of individual particles within dense jets. Aspects (a) and (b) for the ILD detector are demonstrated in Section 3.2.1 and 3.2.3. of this document.

A TPC as the main tracker in a linear collider experiment offers several advantages. Tracks can be measured with a large number of three-dimensional $r\phi$,z space points. The point resolution, σ_{point}, and double-hit resolution, which are moderate when compared to silicon detectors, are compensated by continuous tracking. The TPC presents a minimum amount of material X_0 as required for the best calorimeter performance. Low material budget also minimizes the effect due to the $\sim 10^3$ beamstrahlung photons per bunch-crossing which traverse the barrel region. Topological time-stamping in conjunction with inner silicon detectors is precise to $\sim$2 ns so that tracks from interactions at different bunch-crossings or from cosmics can readily be distinguished. To obtain good momentum resolution and to suppress backgrounds, the detector will be situated in a strong magnetic field of several Tesla, for which the TPC is well suited since the electrons drift parallel to $\vec{B}$. The strong B-field improves σ_{point} and the two-hit resolution by compressing the transverse diffusion of the drifting electrons to $\mathcal{O}(1$ mm) [77].

Continuous tracking facilitates reconstruction of non-pointing tracks, e.g. from V^0s or certain Susy (GMSB) channels, which are significant for the particle-flow measurement and in the reconstruction of physics signatures in many standard-model-and-beyond scenarios. The TPC gives good particle identification via the specific energy loss dE/dx which is valuable for the majority of physics analyses and for electron identification. The TPC will be designed to be robust while easy to maintain so that an endcap readout module can readily be accessed if repair is needed.

A Time Projection Chamber (TPC) is chosen for the central tracker because of its demonstrated performance in past collider experiments [78]. The main design issues at the linear collider are covered in Section 4.3.2. In Section 4.3.3, the R&D by the LCTPC groups[79, 80]

to determine the best state-of-the-art technology for the TPC is described.

4.3.2 Design

There are important, and interconnected, design issues related to the performance, endcap, electronics, fieldcage, robustness in backgrounds, corrections and alignment. Since methods of investigating these issues have been established from past operational experience, the LCTPC groups have been actively investigating all aspects since 2001.

Performance

Main goals for the TPC performance at the linear collider are given in Table 4.3-5. Understanding the properties and achieving the best possible point resolution have been the object of R&D studies of Micro-Pattern Gas Detectors (MPGD), MicroMegas[81] and GEM[82] (Section 4.3.3), and results from this work are reflected in Table 4.3-5. More details about the issues are explained in the following paragraphs.

TABLE 4.3-5
Goals for performance and design parameters for an LCTPC with standard electronics.

Size	$\phi = 3.6$m, L = 4.3m outside dimensions
Momentum resolution (3.5T)	$\delta(1/p_t) \sim 9 \times 10^{-5}$/GeV/c TPC only ($\times$ 0.4 if IP incl.)
Momentum resolution (3.5T)	$\delta(1/p_t) \sim 2 \times 10^{-5}$/GeV/c (SET+TPC+SIT+VTX)
Solid angle coverage	Up to $\cos\theta \simeq 0.98$ (10 pad rows)
TPC material budget	$\sim 0.04X_0$ to outer fieldcage in r
	$\sim 0.15X_0$ for readout endcaps in z
Number of pads/timebuckets	$\sim 1{\times}10^6/1000$ per endcap
Pad size/no.padrows	$\sim$ 1mm$\times$4–6mm/$\sim$200 (standard readout)
σ_{point} in $r\phi$	$< 100\mu$m (average over $L_{sensitive}$, modulo track ϕ angle)
σ_{point} in rz	$\sim$ 0.5 mm (modulo track θ angle)
2-hit resolution in $r\phi$	$\sim$ 2 mm (modulo track angles)
2-hit resolution in rz	$\sim$ 6 mm (modulo track angles)
dE/dx resolution	$\sim$ 5 %
Performance	$>$ 97% efficiency for TPC only ($p_t > 1$GeV/c), and
	$>$ 99% all tracking ($p_t > 1$GeV/c) [83]
Background robustness	Full efficiency with 1% occupancy,
	simulated for example in Fig. 4.3-4(right)
Background safety factor	Chamber will be prepared for 10 $\times$ worse backgrounds
	at the linear collider start-up

Endcap

The two TPC endcaps will have an area of 10 m^2 each. The readout pads, their size, geometry and connection to the electronics and the cooling of the electronics, are all highly correlated design tasks. The material of the endcap and its effect on ECAL for the particle-flow measurement in the forward direction must be minimized, and the goal is to keep it

below 15%X_0. Designing for the finest possible granularity will minimize the occupancy arising from the TPC drifttime integrating over about 100 bunch-crossings[84]. The sensitive volume will consist of several$\times 10^9$ 3D-electronic standard-readout voxels (two orders of magnitude more than at LEP) or 10^{12} voxels in case of pixel readout. Development of the layout of the endcaps, i.e. conceptual design, stiffness, division into sectors and dead space, has started, and first ideas are shown below (Section 4.3.3).

Electronics

For the readout electronics, one of the important questions is the density of pads that can be accommodated while maintaining a stiff, thin, coolable endcap. The options being studied are (1) standard readout of several million pads or (2) pixel readout of a thousand times more pads using CMOS techniques. Table 4.3-5 assumes standard readout electronics; a similar table for pixel electronics will be made when the R&D is further advanced [79] [80]. A basic ingredient for the front-end electronics will be the use of power-pulsing which is possible due to the bunch-train time structure and is assumed to give a power reduction of order 100; what can be achieved in practice is an important R&D issue (Section 4.3.3).

(1) Standard readout:

Small pads, $\sim$ 1mm$\times$5mm, have been found to provide good resolution from the R&D work and to guarantee the low occupancy in Table 4.3-5. Studies have started to establish the realistic density of pads that can be achieved on the endcap. A preliminary look at the FADC approach (à la Alice[85][86]) using 130 nm technology indicates that even smaller sizes might be feasible. An alternative to the FADC-type is the TDC approach (see [80][86]) in which time of arrival and charge per pulse by time-to-charge conversion are measured. In preparation for the possibility that the material budget requires larger pads, the resistive-anode charge-dispersion readout technique[87] is being studied as an option to maintain the good point resolution. Since this technique could compromise the two-track resolution, more R&D is required.

(2) CMOS pixel readout:

A new concept for the combined gas amplification and readout is under development [80][88]. In this concept the "standard" MPGD is produced in wafer post-processing technology on top of a CMOS pixel readout chip, thus forming a thin integrated device of an amplifying grid and a very high granularity endcap with all necessary readout electronics incorporated. For a readout chip with $\sim 50\mu$m pixel size, this would result in $\sim 2 \cdot 10^9$ pads ($\sim 4 \cdot 10^4$ chips) per endcap. This concept offers the possibility of pad sizes small enough to observe the individual primary electrons formed in the gas and to count the number of ionisation clusters per unit track length, instead of measuring the integrated charge collected. The R&D program (Section 4.3.3) will determine on what time scale this technology will become feasible for a large TPC[79].

Fieldcage

The design of the inner and outer fieldcages involves the geometry of the potential rings, the resistor chains, the central HV-membrane, the gas container and a laser system. These must be laid out to sustain at least 100kV at the HV-membrane with a minimum of material. The goals for the inner and outer fieldcage thicknesses are about 1%X_0 and 3%X_0, respectively, while the chamber gas adds another 1%X_0. For alignment purposes the laser system is foreseen and may be integrated into the fieldcage [85][89]. The non-uniformities due to the fieldcage design and fabrication can be minimized using the experience gained in past TPCs.

Backgrounds and robustness

The issues are the space-charge, covered in the next item below, and the track-finding effi-

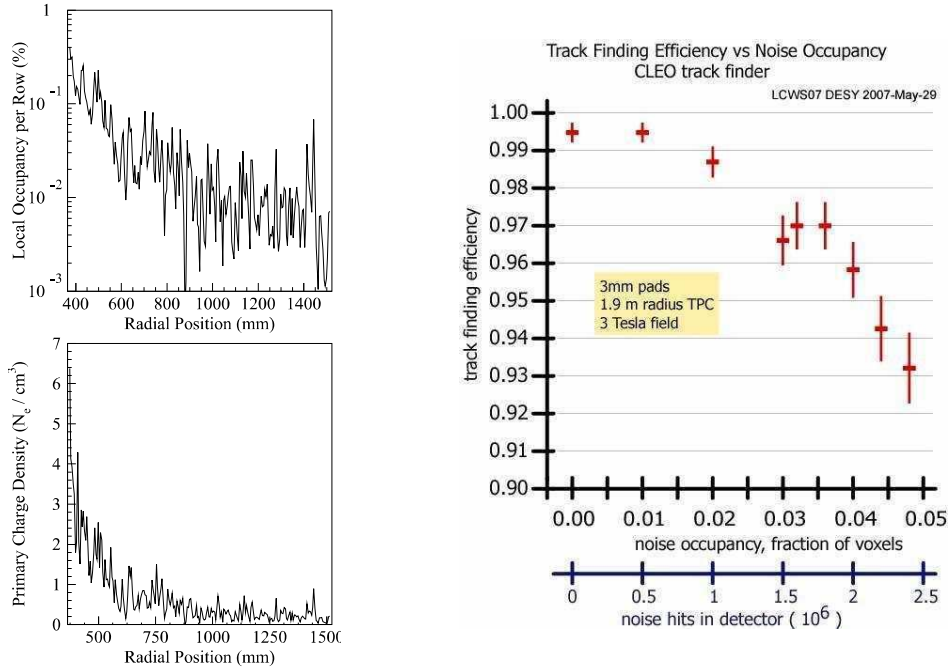

FIGURE 4.3-4. Occupancy for xyz $= 1 \times 5 \times 5\text{mm}^3$ voxels (left, top) and space charge(left, bottom) due to the major beam-beam effects (beamstrahlung photons, electron-positron pairs and neutrons) as simulated in [84]. Study of the tracking efficiency in the presence of backgrounds (right); this study [90] assumed a conservative voxel size of $3 \times 10 \times 40\text{mm}^3$.

ciency in the presence of backgrounds which will be discussed here. There are backgrounds from the collider, from cosmics or other sources and from physics events. The main source is the collider, which gives rise to gammas, neutrons and charged particles due to $\gamma\gamma$ interactions and beam-halo muons being deposited in the TPC at each bunch-crossing [79]. Simulations of the main sources [84] arising from beam-beam effects–gammas, pairs and neutrons–under nominal conditions indicate an average occupancy of the TPC of less than 0.1%, Fig. 4.3-4 (left). The TPC track finding remains robust at these occupancies; the continuous 3D-granularity tracking is inherently simple and suffers no loss in efficiency with a uniform 1% noise occupancy as demonstrated by the study in Figure 4.3-4(right).

Since the backgrounds at the beginning of operation could be much larger until the linear collider machine is well understood, the LCTPC is preparing for an occupancy of 10%.

Corrections for non-uniform fields

Both fields, (A) magnetic and (B) electric, can have non-uniformities which must be corrected. The (C) chamber gas will play a crucial role in minimizing corrections.

(A) Magnetic field

Non-uniformity of the magnetic field of the solenoid will be by design within the tolerance of $\int_{\ell_{\text{drift}}} \frac{B_r}{B_z} dz < 2-10\text{mm}$ as used for previous TPCs. This homogeneity is achieved by corrector windings at the ends of the solenoid. At the ILC, larger gradients will arise from the fields of the DID (Detector Integrated Dipole) or anti-DID, which are options for handling the beams inside the detector at an IR with ±7 mrad crossing-angle. This issue was studied intensively and summarized in [91], where it is concluded that the TPC performance will not be degraded if the B-field is mapped to around 10^{-4} relative accuracy and the procedures outlined below (under **Alignment**) are followed. These procedures will lead to an overall systematic error

due to the field components of $\sim$ 30 μm over the whole chamber which has been shown to be sufficient [91] and was already achieved by the Aleph TPC. Based on past experience, the field-mapping gear and methods will be able to accomplish the goal of 10^{-4} for the relative accuracy. The B-field should also be monitored during running since the currents in the DID or corrector windings may differ from the configurations mapped.

(B) Electric field

Three sources of space charge are (*i*) primary ion build-up in the drift volume, (*ii*) ion build-up at the readout plane and (*iii*) ion backdrift, where ions created at the readout plane could drift back into the TPC volume.

(*i*) Primary ion build-up in the drift volume. An irreducible positive-ion density due to the primary ionisation collected during about 1s (the time it takes for an ion to drift the full length of the TPC) will be present in the drift volume. The positive-ion density will be higher near the cathode, where the local volume integrates over backgrounds from up-to-five bunch trains, and using Fig. 4.3-4(middle)[1], the charge will reach $\sim$1 fC/cm^3 at the inner fieldcage and $\sim$0.02 fC/cm^3 at the outer fieldcage. The effect of the charge density will be established by the R&D program, but the experience of the STAR TPC [89] indicates that 100 fC/cm^3 is tolerable[79] and is two orders of magnitude larger than expected for the LCTPC.

(*ii*) Ion build-up at the readout plane. At the surface of the gas-amplification plane during an ILC bunch train of about 3000 bunch crossings spanning 1 ms, there will be few-mm sheet layer of positive ions built up due to the gas amplification of the incoming charge followed by ion backflow. An important property of MPGDs is that they suppress naturally the backflow of ions produced in the amplification stage; studies show that this backflow can be reduced to about 0.25% [79]. Using the results from Fig. 4.3-4 (middle), this layer of readout-plane ions will attain a density of $\mathcal{O}(80)$ fC/cm^3 at the inner radius and $\mathcal{O}(2)$ fC/cm^3 at the outer radius of the TPC. Its effect will be simulated, but it should affect coordinate measurement only by a small amount since the incoming drift electrons experience this environment during only the last few mm of drift. The TPC must plan to run with the lowest possible gas gain, meaning of order $\sim 2 \times 10^3$ or less, in order to minimize this effect.

(*iii*) Ion backdrift and gating. The ion buildup described in (*ii*) will drift as an "ion sheet" back through the TPC volume unless eliminated by a gating plane. In the drift volume, an ion sheet would be followed by sufficient drift distance to result in track distortions. Thus an intra-train gate is foreseen to guarantee a stable and robust chamber operation. The ILC bunch train structure requires an open-gate operation, without intra-train gating between bunch crossings, to optimally utilize the delivered luminosity. The gate will remain open throughout one full train and be closed between bunch trains. As the ion drift velocity is much less than that of the electrons, the gate timing allows collection of all of the ions. The added amount of material for a gating plane will be small (e.g., $< 0.5\%X_0$ was the average thickness for the Aleph TPC gate).

(C) Chamber gas

The choice of the gas for the LCTPC is crucial for efficient and stable operation at the linear collider[77]. The σ_{point} resolution achievable in $r\phi$ is dominated by the transverse diffusion, which should be as small as possible; this implies that $\omega\tau$ for the gas should be large so that the transverse diffusion is compressed by the B-field. Large $\omega\tau$ means that the drifting electrons follow the B-field, for which there is a program to measure well[91], and has the added advantage of making the chamber less sensitive to space-charge effects and other

[1] The numbers in the text derived from this figure have been multiplied by a safety factor of two to account for other sources of backgrounds.

sources of electric field non-uniformities. Simultaneously a sufficient number of ionisation electrons should be created for the position and dE/dx measurements. The drift velocity at a drift field of at most a few times 100 V/cm should be around 5–10 cm/μs to limit the central cathode voltage and the event overlap. The choice of operating voltage must also take into account the stability of the drift velocity due to fluctuations in temperature and pressure.

Alignment

Achieving a momentum resolution an order of magnitude better than any of the collider detectors to date will be a challenge. The systematics of alignment of tracking subdetectors must be well thought through from the beginning to guarantee the integrity of tracking over a radius of two meters. Redundant tools for solving this issue are Z-peak running, the laser system, the B-field map as described in [91] and monitored by a matrix of Hall-plates/NMR-probes outside the TPC, and Si-layers inside the inner fieldcage and outside the outer fieldcage. In general based on experience at LEP[92], about 10 pb^{-1} of data at the Z peak are requested during commissioning for the alignment of the different subdetectors, and typically 1 pb^{-1} during the year may be needed depending on the backgound and operation of the linear collider machine (e.g., after push-pull or beam loss).

The strategy learned at LEP for aligning the tracking subdetectors is also applicable for the ILD. Needed to start with are: a common alignment software package for all subdetectors, the fabrication tolerances for each subdetector $\simeq$ 10–20μm internal and $\simeq$ 0.1–0.2mm external (with respect to the other subdetectors) and the B-field mapped to the requirements outlined in [91]. Then the steps are: first pass through a subset of data (hadronic tracks or μ pairs from Z-peak or from $\sqrt{s}$ running), each tracking detector is aligned internally; second pass, the tracking subdetectors are lined up with respect to one another using a subset of data; finally the preceeding two steps are iterated until the correct momentum for $Z \rightarrow \mu\mu$ events is achieved.

4.3.3 R&D Effort for the LCTPC

All of the issues affecting the TPC performance are being addressed by the R&D program; a recent status report with extensive references to past and on-going work is contained in [80]. As described in the LCTPC-Collaboration MoA, the R&D is proceeding in three phases: (1) Small Prototypes (SP), (2) Large Prototypes (LP), and (3) Design.

Up to now during Phase(1), about 6 years of MPGD experience has been gathered, gas properties have been well measured, the best achievable point resolution is understood, the resistive-anode charge-dispersion technique has been demonstrated, CMOS pixel RO technology has been demonstrated, the proof of principle of TDC-based electronics has been shown and commissioning has started for the LP.

The Phase(2) LP and SP work is expected to take another two–three years. Regular bi-weekly WP phone meetings started in May 2006 where details for the LP design were worked out and next R&D steps developed. The LP commissioning is well advanced as evidenced by Fig. 4.3-5(left), while the fruits of the SP work resulting in the expected resolution are shown in Fig. 4.3-5(center) and Fig. 4.3-5(right).

The following list gives an overview of the currently envisioned timeline for completing the studies and the construction of the ILD TPC.

• 2009-12: Continue R&D on technologies at LP, SP, pursue simulations, verify performance goals (details are available in [80]).

• 2009-11: Plan and do R&D on advanced endcap; power-pulsing, electronics and mechanics

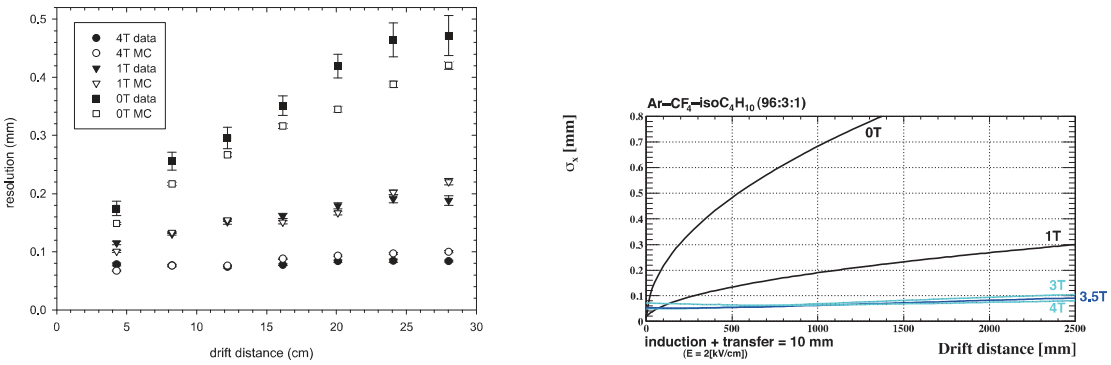

FIGURE 4.3-5. (left): Example of resolution results from a small prototype [93] measurements with TDR gas, $ArCH_4CO_2$ (95-3-2); other candidate gases are e.g. P5 and $ArCF_4$Isobutane. (Right): Theoretical resolution for $ArCF_4$Isobutane (96-3-1) gas (right), based on an algorithm [80] verified during SP studies.

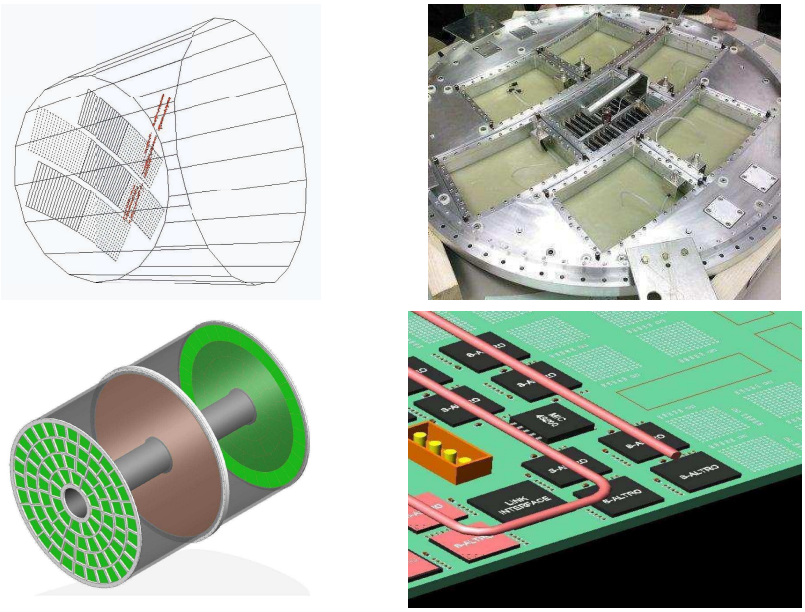

FIGURE 4.3-6. (Top left): Event display from the LP beam tests. (Top right) View of the Endcap subdivision as used for the Large Prototype. (Bottom left)Conceptual design of enplate for LCTPC. (Bottom right) Possible layout of PCB, electronics and cooling for the LCTPC.

are critical issues.

- 2011-12: Test advanced-endcap prototype at high energy and power-pulsing in high B-field.
- 2012-18: Design and build the LCTPC.

Construction of endplates that satisfy the material requirements of the ILD, as well as the structural requirements of the TPC, will require extensive R&D.

This work has started with first ideas having been developed in a series of "advanced-endcap" meetings during the past year. Examples are presented in Fig. 4.3-6, and the groups agree that there will be an evolution of endcaps towards a true prototype for the LCTPC.

During the R&D period 2009-2011, engineering studies of detailed computer models of advanced endplate designs will be performed. The models will be evaluated relative to the

requirements of material limits and distribution, space limits, rigidity in response to applied forces, manufacturing complexity and manufacturing precision. Possible endcap designs fall into two general groups. The first group is the evolution of a traditional machined endplate, as used in the first endcap of the LP, Fig. 4.3-6 (left), but with significant use of lighter materials; in addition, unnecessary material must be removed from the machined structure. The second group is the simulation of true space-frame designs which can be constructed utilizing various techniques, e.g., fully machined, bonded composites and assembly of individual components.

During the period 2011-2012, further study of designs that were successful as computer models will follow. Several prototypes of the advanced endplate will be manufactured; both scale-models (20-50% full size) and sections of the full size endplate will be used to evaluate the manufacturing integrity and uncover sources of loss of precision or rigidity in the design. Finite element analysis will be used to predict the strength of the full size endplate; this analysis will be calibrated by comparison with measurements on the prototypes.

At the beginning of the period 2012-18, the selection must be made from the different technological options – GEM, MicroMegas, resistive anode, pixel, electronics, endcap structure – to establish a working model for the design of the LCTPC. This design will be used for the ILD proposal in 2012 and include pad segmentation, electronics, mechanics, cooling and integration, so that performance, timeline and cost can be estimated reliably. [2] For the technology selection, a scenario could be that questions must be answered as to which options give the best performance based on R&D results from LP, SP, electronics and endcap studies. Main performance criteria could be endcap thickness and σ_{point}, double-hit and momentum resolution for single tracks and for tracks in a jet environment. Choice of criteria to use will be decided over the next two years.

Finally, as to the $\sqrt{s}$ coverage, a question posed by the Research Director and IDAG, simulations in Chapter 2 of this LOI have shown that, with the performance goals in Table 4.3-5, the LCTPC will give good performance up to and well beyond 1 TeV.

,

4.4 THE CALORIMETER SYSTEM

4.4.1 Introduction to calorimeters

Tagging of electroweak gauge bosons at the ILC, based on di-jet mass reconstruction, makes the reconstruction of multijet events a major goal for detectors at the ILC. The particle flow approach (see e.g. [94]), which consists of individual particle reconstruction dictates many fundamental aspects of the calorimeter design, most notably the requirement for very fine transverse and longitudinal segmentation of the calorimeters, as studied in Section 2.2. It has to be noted that a highly granular calorimeter, optimised for PFA, leads also to a way to have a very efficient software compensation, as it is shown in 4.4.4.2. The choice of technology for the ECAL and HCAL are driven by the requirements of pattern recognition more than the intrinsic single particle energy resolution, although the latter is still an important consideration.

Several technologies for electromagnetic and hadronic calorimeters are being pursued, with a number of prototypes in test beams. Next generation prototypes are being constructed with dimensions and integration issues very close to those of final ILD detector modules. The research and development work is carried out in the context of the CALICE collaboration [95].

[2] Upgrades can be made where evolving improvements are warrented by R&D studies and the timeline.

4.4.2 General Layout

The calorimeter system is divided in depth into an electromagnetic section, optimised for the measurement of photons and electrons, and a hadronic section dealing with the bulk of hadronic showers. The two parts are installed within the coil to minimise the inactive material in front of the calorimeters. To follow the symmetry imposed by the beams and the coil, the calorimeter is divided into a cylindrical barrel and two end-caps.

The electromagnetic calorimeter consists of tungsten absorber plates interleaved with layers of Silicon (pads or pixels), or Scintillator detectors with very fine segmentation of the readout. The hadronic calorimeter is planned as a sampling calorimeter with steel absorber plates and fine grained readout. Two options are currently proposed. The first uses scintillator cells with fine granularity and multi-bit (analogue) readout. The second is based on gaseous detectors and uses even finer granularity. Due to the large number of cells, in the second case one- or two-bit (semi-digital) readout is sufficient.

4.4.3 The Electromagnetic Calorimeter

For the electromagnetic calorimeter the requirements on granularity, compactness and particle separation lead to the choice of a sampling calorimeter with tungsten (radiation length $X_0 = 3.5\,\mathrm{mm}$, Molière Radius $R_M = 19\,\mathrm{mm}$ and interaction length $\lambda_I = 99\,\mathrm{mm}$) as absorber material. This allows for a compact design with a depth of roughly $24\,X_0$ within 20 cm and, compared to e.g. lead, a better separation of EM showers generated by near-by particles.

To achieve an adequate energy resolution, the ECAL is longitudinally segmented into around 30 layers, possibly with varying tungsten thicknesses. The active layers (either silicon diodes or scintillator) are segmented into cells with a lateral size of $5 - 10\,\mathrm{mm}$ to reach the required pattern recognition performance.

4.4.3.1 Geometry and Mechanical Design

One of the requirements for the calorimeter is to ensure the best possible hermeticity. Three regions are of particular concern for this question: the boundaries between mechanical modules, the overlap between barrel and end-cap, and the small angle region with the connection to the luminosity monitor. To minimise the number and effect of cracks in the barrel, a design with large modules is preferred, with inter-module boundaries not pointing back to the IP. The cylindrical symmetry of the coil has been approximated by an eight-fold symmetry and the modules are designed in a such a way (c.f. fig. 4.4-7 that the cracks are at very large angle with respect to the radial direction. This octagonal shape optimises the barrel module sizes and their mechanical properties without diverging too far from a circle. One eighth of the barrel calorimeter is called a stave. Each stave is fastened to the HCAL front face with a precise system of rails. Some space is left between the ECAL and the HCAL to accommodate different services such as cooling, electrical power and signal distribution. Along the beam axis, a stave is subdivided into five modules. The ECAL end-caps are attached to the front face of the hadronic end cap calorimeters using a similar rail system.

A detailed mechanical design of the modules has been prepared, and is tested under real conditions in several test beam experiments. More details can be found in [96].

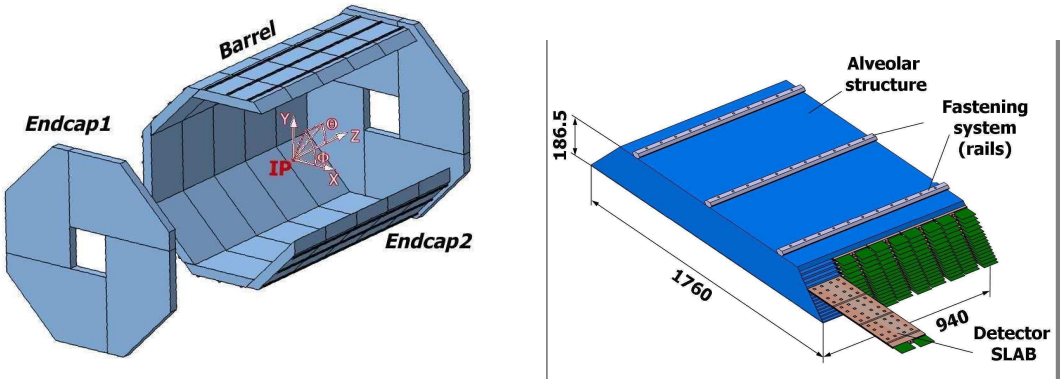

FIGURE 4.4-7. Global layout of the ECAL (left) and layout of one module (right).

4.4.3.2 Optimisation

For the final detector, a global optimisation study of the longitudinal profile has to be performed, by varying the thickness of the Silicon and Tungsten layers as a function of the depth, in order to minimise cost, lateral spread and energy resolution.

The dependence of the ECAL energy resolution as a function of the longitudinal sampling scheme has been studied in simulation [97]. For a given number of sampling layers, the energy resolution improves if the first part of the calorimeter is more finely segmented than the latter part. The effect of the silicon cell size on ECAL performance has been studied in simulation, focusing on the photon reconstruction capability in di-jet events and hadronic τ decays. Three different cell-sizes ($5\times5\,\mathrm{mm}^2$, $10\times10\,\mathrm{mm}^2$ and $20\times20\,\mathrm{mm}^2$) have been investigated. In both cases a specialised photon reconstruction algorithm (GARLIC [98]) has been applied. The algorithm was separately tuned for each cell-size.

Figure 4.4-8 shows the mean ratio of calorimetric energy reconstructed as photons to the true photon energy, in simulated di-jet events at $E_{\mathrm{CM}} = 400\,\mathrm{GeV}$ for a variety of cell sizes. A cell-size of $5\times5\,\mathrm{mm}^2$ is clearly to reconstruct the correct fraction of photon energy inside jets. The interpretation of these result, which is based on a dedicated photon finding algorithm, requires care. It can not be applied directly to full particle flow reconstruction, which in general shows a weaker dependence.

Studies of τ reconstruction have been performed in ZH ($\mathrm{H}\rightarrow\tau\tau$) events at $E_{\mathrm{CM}} = 230\,\mathrm{GeV}$ with $m_{\mathrm{H}} = 120\,\mathrm{GeV}$. The three decay modes $\tau\rightarrow\nu\pi$, $\tau\rightarrow\nu\rho$ and $\tau\rightarrow\nu a_1$ have been considered. The reconstructed invariant mass of the visible τ decay products is shown in Fig. 4.4-9 for the three different cell sizes. A simple selection based on particle flow (reconstructed photons) and jet mass (cut at 200 MeV) allows one to reach good efficiency and purity, without the need for the more sophisticated analysis. The efficiencies and purities of the reconstruction of the various decay channels are given in Table 4.4-6. Again a cell size of $5\times5\,\mathrm{mm}^2$ is favoured although the performance loss with respect to $10\times10\,\mathrm{mm}^2$ cells is smaller than in high-energy jets.

To study the effect of material in front of the ECAL on the particle flow performance, 4 GeV single charged pion events have been simulated. The π^0's produced in interactions in the tracker region may give rise to additional reconstructed photons in the ECAL. The GARLIC photon identification algorithm [98] has been applied to the single pion events. For the approximately six percent of pions which interact in the tracking volume, Fig. 4.4-10 shows the position of the pion interaction point inside the detector for events in which

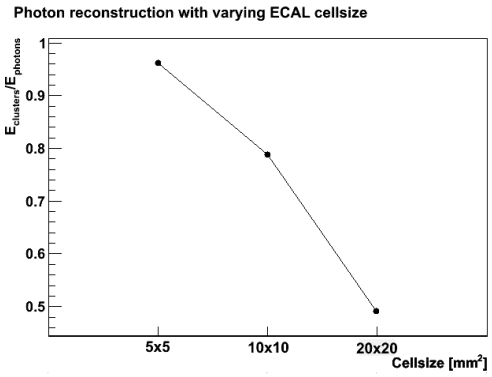

FIGURE 4.4-8. Fraction of energy identified as photon induced to true photon energy (Monte Carlo truth) in di-jet events at $E_{\mathrm{CM}} = 400\,\mathrm{GeV}$.

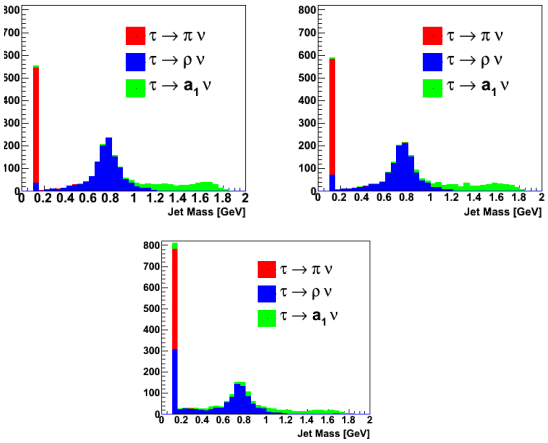

FIGURE 4.4-9.]
Reconstructed invariant mass of hadronic τ decay products in ZH $\rightarrow \mu\mu\tau\tau$ events for different ECAL cell sizes (starting at top left: $5 \times 5\mathrm{mm}^2$, $10 \times 10\mathrm{mm}^2$, and $20 \times 20\mathrm{mm}^2$.

	$5 \times 5\,\mathrm{mm}^2$			$10 \times 10\,\mathrm{mm}^2$			$20 \times 20\,\mathrm{mm}^2$		
	π_{sim}	ρ_{sim}	$a1_{\mathrm{sim}}$	π_{sim}	ρ_{sim}	$a1_{\mathrm{sim}}$	π_{sim}	ρ_{sim}	$a1_{\mathrm{sim}}$
π_{rec}	98.8	2.8	1.9	98.7	5.9	1.6	98.6	27.1	7.0
ρ_{rec}	1.2	96.5	9.2	1.3	93.4	15.0	1.4	72.3	54.4
$a1_{\mathrm{rec}}$	0	0.7	88.9	0	0.7	83.4	0	0.6	38.6

TABLE 4.4-6
Reconstruction efficiencies and purities of hadronic τ decays in $ZH \rightarrow \mu\mu\tau\tau$ events with various ECAL cell-sizes

photon clusters are (red points, 55%) or are not (black points, 45%) found. The TPC endplates and gas give the largest contribution to the total number of pion interactions in front of the ECAL. When only those interactions which give rise to identified photon clusters are considered, the detector components at the centre of the detector, that is, the vertex detector, SIT, beam tube and FTD support, also give significant contributions. Even though ILD has been designed with with minimum material in the tracker in mind, there is still about one pion per event which interacts in the tracker volume. This underlines the need for continued R&D and continued care toward further material reduction in the tracker.

4.4.3.3 Silicon - Tungsten Electromagnetic Calorimeter

The general requirement about compactness (small Molière radius) has led to a sandwich calorimeter with a tungsten radiator and silicon for the sensitive medium. To reach an adequate energy resolution the first 12 radiation lengths are filled with 20 layers of $0.6\,\mathrm{X}_0$ thick tungsten absorbers (2.1 mm), followed by another 11 radiation lengths made from 9 layers of tungsten $1.2\,\mathrm{X}_0$ thick. The calorimeter starts with an active layer. For the chosen geometry the Molière radius is 19 mm. The choice of silicon technology for the readout layer

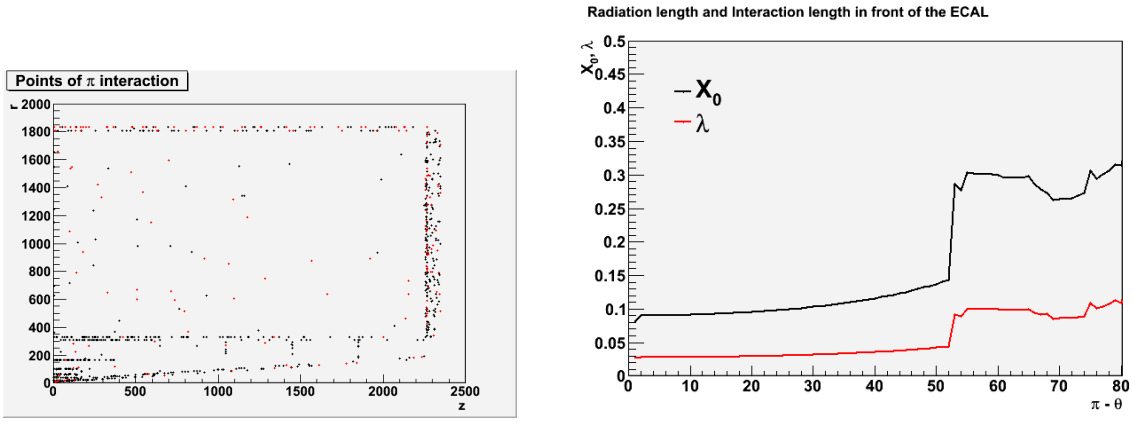

FIGURE 4.4-10. Left: Interactions points of single photons in the tracker region of ILD. The black points correspond to interactions that lead to the creation of clusters in the calorimeter found with the GARLIC photon reconstruction while the red points correspond to interactions that did not create any clusters. Right: Number of radiation and interaction length in front of the ECAL as a function of the polar angle.

	% of total interactions	% with clusters	% of total events with clusters
VTD	11.9	64.5	13.9
SIT	11.8	68.7	14.6
Beam pipe	10.4	62.9	11.8
FTD	8.9	66.1	10.6
TPC inner field cage	5.4	63.8	6.2
TPC gas	17.1	23.0	7.1
TPC outer field cage	6.5	50.6	5.9
TPC endplate	22.3	61.4	24.8
SET	3.1	58.0	3.3
ETD	2.8	35.1	1.8

TABLE 4.4-7
Interaction of pions in the different parts of the tracker region.

permits a very high transverse granularity, now fixed at $5 \times 5\,\mathrm{mm}^2$.

The final calorimeter will contain around 10^8 readout cells in total. To keep the final system as compact as possible, and reduce dead areas, the very front end electronics will be embedded into the detector layers.

The challenging construction of the SiW ECAL is currently tested by a large scale R&D program pursued by the CALICE Collaboration. Results from test beam measurements demonstrating the feasibility to realise the detector have been published in [96, 99]. The energy resolution has been determined to be $(16.6 \pm 0.1)/\sqrt{E(\mathrm{GeV})} \oplus (1.1 \pm 0.1)\,\%$ with a MIP signal over noise ratio $S/N \approx 7.5$.

At present, the CALICE collaboration is preparing the construction of a prototype module with a size and shape close to the modules envisaged for the final calorimeter.

The detector slabs are built around an H-shaped supporting structure incorporating a

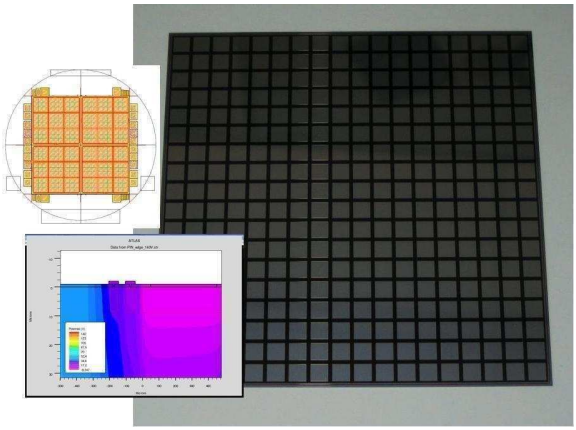

FIGURE 4.4-11. $5 \times 5\,\mathrm{mm}^2$ pad Hamamatsu sensor (right). Layout of prototype sensors with optimised edges (upper left). In depth simulation of the potential near a guard ring (lower left).

layer of tungsten absorber. An active layer is placed on each side of this structure. This active layer is a chain of identical Active Sensor Units (ASUs), which consist of a printed circuit board (PCB) integrating the Silicon sensors, Front-End electronics and electrical infrastructure. Each ASU can run as a standalone unit, allowing testing of each piece before, during and after slab assembly, resulting in a high detector yield, and thus a reduced cost.

Since the electronics are deeply embedded in the detector volume, and no space is available for active cooling, their power consumption must be kept to a minimum to prevent overheating. By power-pulsing the electronics according to the duty-cycle of the ILC machine, the consumption can be kept below $25\,\mu\mathrm{W}$ per channel.

The sensors are based on high resistivity silicon ($5\,\mathrm{k}\Omega/\mathrm{cm}$) with individual pin-diodes of $5 \times 5\mathrm{mm}^2$ size. This size is also feasible for the readout electronics. A test batch of sensors based on 6" wafers has been used by Hamamatsu to produce $9 \times 9\,\mathrm{cm}^2$ matrices. The bonding of the sensors onto the PCB is performed using a well controlled gluing technique.

The silicon sensors are built and integrated using well known, widely used and well controlled technologies. The matrix of PIN diodes is burned onto 330 μm thick raw silicon wafers using standard manufacturing processes from the microelectronics industry such as acceptor/donator ion implantation, oxide growth or metal deposit. The bonding of the sensors onto the PCB is performed using a well controlled gluing technique: standard glue (EPOTEK 410) applied by a robotic gluing machine. Prototypes of sensors have been ordered to various companies and academic centres with two different sizes of PIN diodes. No problems due to the gluing technique have been observed over a time span of several years.

The total surface of sensors for the whole ECAL is about $2500\,\mathrm{m}^2$. The sensors and their integration are kept as simple as possible to avoid any dependence on a proprietary technique owned by a single manufacturer; allowing for a variety of suppliers and manufacturers to share the production will decrease the inherent financial risks and enable a competitive downscaling of the costs.

4.4.3.3.1 Calibration The charge produced by a MIP in the silicon depends only on the silicon thickness, and is therefore expected to be stable with time. A single calibration before detector assembly will therefore be sufficient. The ASUs will be calibrated in a muon beam before the assembly of detector slabs and their integration into detector modules.

The VFE electronics will be calibrated by means of the VFE chips' charge injection

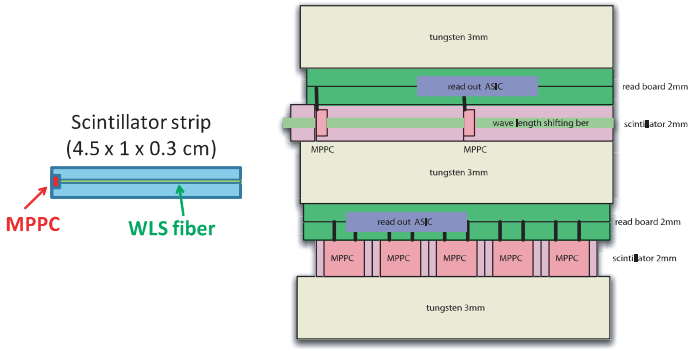

FIGURE 4.4-12. Dimension of the scintillator-strip (left, view from top) and side view of the ScECAL layer structure (right).

calibration system.

Since the tracks of muons and non-interacting charged pions in the ECAL can easily be identified due to the ECAL's high granularity, they can be used to monitor the calibration during the lifetime of the detector.

4.4.3.4 Scintillator - Tungsten Electromagnetic Calorimeter

The scintillator-tungsten sandwich ECAL (ScECAL) is proposed to realise a fine-segmented calorimetry in a stable, robust and cost effective way. The fine grained readout is realised by planes of 1 cm wide and 4.5 cm long strips, arranged in orthogonally in adjacent layers. Thanks to the strip structure, the number of necessary readout channels is significantly reduced ($\sim 10^7$ channels) relative to the Si-W option. Scintillator strips can be cheaply produced by the extrusion method. Compact photo-sensors (MPPC) and highly integrated readout electronics make dead area in the ScECAL almost negligible. Keeping the required granularity and these merits, the ScECAL has good energy resolution and linearity.

The ScECAL consists of 24 super-layers. A schematic view of a few super-layers of the ScECAL is shown in Figure 4.4-12. They will be mounted in an alveolar structure similar to the case of the SiW ECAL. A super-layer is made of a tungsten plate (3 mm thick), scintillator strips (2 mm thick), and a readout/service layer (2 mm thick). Scintillator strips in adjacent super-layers are arranged to be orthogonal aiming for better effective granularity. The thickness of a super-layer is 7 mm. The total ScECAL thickness is 172 mm, or 20.6 X_0 in radiation length.

4.4.3.4.1 The active layers The dimension of an individual scintillator strip (see Fig. 4.4-12) is $1 \times 4.5 \times 0.2\,\mathrm{cm}^3$. Although a strip width of 5 mm, to realise an effective granularity of $5 \times 5\,\mathrm{mm}^2$, is thought to be feasible, further R&D is necessary. Each strip is covered by a mirror reflector film to improve collection efficiency and uniformity of the scintillation light. Photons from each scintillator strip are read out via an 1 mm diameter wavelength shifting fibre (WLSF) embedded in a straight groove by a very compact photon sensor, MPPC, attached at the end of the strip.

The MPPC is a version of a novel semiconductor photo-sensors consisting of a matrix of micro APD pixels operated in Geiger mode. Photo-detection performance and amplification power is comparable with conventional photomultiplier tubes. The dynamic range of an MPPC is limited by the number of APD pixels. A MPPC with 1600 APD pixels in an area

of $1\,\mathrm{mm}^2$ is already commercially available. However MPPC with ~ 3000 pixels should be developed to precisely measure up to $\sim 100\,\mathrm{GeV}$ electromagnetic clusters.

Signals from about 80 MPPC are fed into a readout chip through micro-strip lines. They are arranged on one identical flexible readout board (FPC) (c.f. Fig. 4.4-13). After shaping, digitisation and zero-suppression of the analog signals on the chip, signals are taken out serially from the detector and brought to a digitisation board by a thin FPC cable ($\sim 200\,\mu\mathrm{m}$) through detector gap.

4.4.3.4.2 Calibration systems

A light distribution system has been designed to monitor possible gain drifts of MPPCs by monitoring photo-electron peaks. The system consists of a pulse generator, a chip LED, and a notched fibre. A schematic structure of the system is shown in Figure 4.4-14. The pulse generator circuit and the chip LED are arranged on a thin ($\sim 200\,\mu\mathrm{m}$) FPC board. The chip LED is directly connected to the notched fibre to distribute lights to ~ 80 strips through its notches.

Each scintillator strip can be calibrated with data by monitoring the MIP peak using multi-hadron events at the ILC. Monte Carlo simulation shows that more than 100 MIP hits per strip will be obtained if running at the Z^0. With this method the strips can be calibrated to better than 5 % with $1\,\mathrm{fb}^{-1}$ of $\mathrm{Z}^0 \to jj$ events).

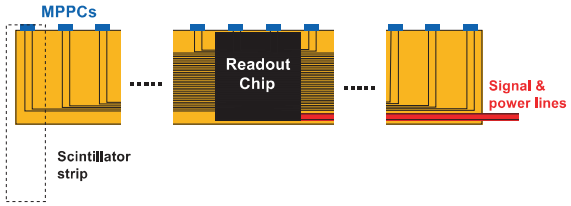

FIGURE 4.4-13. Layout of the MPPC, micro-strip line and readout chip on the FPC board.

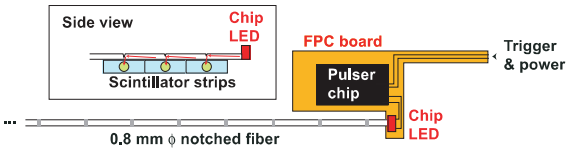

FIGURE 4.4-14. Schematics of the MPPC gain monitoring system with LED and notched fibre. Light pulses from the LED are scattered and distributed into each strip.

4.4.3.4.3 Status and Future R&D plans

The feasibility of the ScECAL has been proven by a test of a small prototype using $1 - 32\,\mathrm{GeV}$ electron beams. At the test clean MIP signal and electron energy spectra are observed with negligible contamination from electrical noise. The energy resolution is measured to be $\sigma_E/E = 14/\sqrt{E} \oplus 2\,\%$ which is consistent with expectation from simulation.

In order to fully establish the feasibility of the ScECAL, further extensive R&D efforts are necessary to clarify the remaining technical issues as follows:

- Photon sensors: properties of the MPPC have to be further studied and improved. The increase of the dynamic range is especially important.
- Development of readout electronics: A highly integrated readout chip is needed due to the limited space in the detector.
- Strip clustering: The strip structure is chosen in order to improve the effective granularity of the calorimeter. A clustering algorithm has been developed which can cope with the strip structure as well as the usual square-tile structure. The algorithm is being further improved, and performance of the strip structure must be demonstrated.

4.4.3.5 Digital (MAPS) Silicon-Tungsten Electromagnetic Calorimeter

The silicon-tungsten digital ECAL (DECAL) is an alternative to the analogue silicon design described in Section 4.4.3.3. The basic principle is to replace the high resistivity pad diodes with CMOS based binary readout pixels sufficiently small in size that, even in the core of high energy electromagnetic showers where the density is typically equivalent to $\sim 100\,\mathrm{MIPs/mm^2}$, the probability of a pixel being hit by more than a single particle will be low. This allows the shower energy to be measured by the number of binary pixels above threshold. To ensure that linearity of response is preserved even at higher energies, pixels are required to be $O(50 \times 50\,\mu\mathrm{m}^2)$, leading to $O(10^{12})$ pixels in the complete ECAL. A very high level of integration of the readout in the pixel is therefore mandatory.

The active layers are based on CMOS Monolithic Active Pixel Sensors (MAPS) which allow data reduction and processing logic to be contained within each pixel. The target noise level is 10^{-6}. A new process ("INMAPS" [100], developed by the CALICE UK groups) ensures efficient charge collection by using deep p-wells and charge collection by diffusion in the sensor. Signals (time stamp and pixel address) are stored on the sensor during a bunch train and read out in the interval between bunch trains. By using industry standard CMOS processes available from a large number of foundries, costs are potentially lower per unit area than analogue silicon diodes, with reduced risk to production schedules.

The performance of the DECAL has been studied using Mokka in the context of LDC [101, 102, 103], including effects of dead area, digitisation and clustering. A preliminary study of the energy resolution of the DECAL to single photons, implemented by adapting only the ECAL sensitive region in the ILD00 silicon-tungsten model in Mokka, gives $\sigma_E/E = 19.7\,\%/\sqrt{(E)}$. A first prototype sensor (TPAC1.0) was designed in 0.18 µm process, having 28224 $(50 \times 50\,\mu\mathrm{m}^2)$ pixels [100]. This $9 \times 9\,\mathrm{mm}^2$ sensor was fabricated and characterised, e.g. [104, 105, 106] during 2007–8. A second revision of the sensor is expected for 2009. A proof-of-principle R&D project is in progress to develop and test a 16 layer DECAL prototype large enough to contain electromagnetic showers [107] by 2012.

The DECAL option is designed to work with the same mechanical structure as the Si-W ECAL, thus profiting from the large R&D done in this area. A topic for future R&D is the reduction and control of the power consumption, which at the moment is expected to be larger though uniformly distributed across the sensor unlike the analogue SiW sensor.

4.4.4 The Hadronic Calorimeter

In a particle flow calorimeter the HCAL plays a crucial role in separating and measuring the energy deposits of charged and neutral hadrons. Since the energy deposited by neutral hadrons fluctuates widely, its precise measurement is a key component of a well performing particle flow calorimeter. Consequently, the imaging capabilities of the HCAL are of prime importance and demand high transverse and longitudinal segmentation and a design with a minimum of uninstrumented ("dead") regions. However, a very good hadronic energy resolution is also mandatory, both to assist the topological assignment of clusters and tracks, and to optimise the precision of the hadronic energy part characterised as neutral. The high granularity allows the application of weighting techniques to compensate for differences between hadronic and electromagnetic response and for "invisible" energy depositions ("software compensation") and improves the hadronic energy resolution further.

4.4.4.1 Geometry and Mechanical Design

The HCAL is conceived as a sampling calorimeter with steel as absorber and scintillator tiles (analogue HCAL) or gaseous devices (digital HCAL) as active medium. As the HCAL must be located within the coil, the absorber has to be non-magnetic. Stainless Steel has been chosen both for mechanical and calorimetric reasons. Due to its rigidity, a self-supporting structure without auxiliary supports (and thus dead regions) can be realised. Moreover, in contrast to heavier materials, iron with its moderate ratio of hadronic interaction length ($\lambda_I = 19\,\mathrm{cm}$) to electromagnetic radiation length ($X_0 = 1.8\,\mathrm{cm}$) allows a fine longitudinal sampling in terms of X_0 with a reasonable number of layers in a given total hadronic absorption length, thus keeping the detector volume and readout channel count small. This fine sampling is beneficial both for the measurement of the sizable electromagnetic energy part in hadronic showers as for the topological resolution of shower substructure, needed for particle separation and weighting.

4.4.4.1.1 Overall architecture The overall structure follows the "short barrel" concept, with two large endcaps with about the same outer radius as the barrel. The total hadronic absorption length corresponds to a minimum of $5.5\,\lambda_I$ in addition to the ECAL. The endcaps are subdivided into four quadrants, their absorber plates are oriented perpendicular to the beam line. The mechanical engineering of the absorber structure has so far concentrated on the barrel. It is assumed that the solutions can be transferred to the endcaps later-on. Compared with existing hadron calorimeters, the ILD HCAL has a rather fine longitudinal sampling, with a correspondingly high pressure on the thickness of the active layer gaps, but also on mechanical tolerances. This, together with the requirement of minimum dead zones represents a challenge to the large scale engineering which is presently being addressed with prototypes within the EUDET/CALICE framework.

For the barrel, two design approaches are being followed: one with long barrel modules, subdivided only once in z, and with electronics and service connections at the end faces, and a second, with 5 rings and interfaces situated at the outer barrel perimeter. The main advantages of the first are the accessibility of the electronics and a maximum filling of the detector volume limited by the coil radius, whereas the second provides better rigidity in the transverse plane, eliminates pointing cracks and allows for a tighter barrel end-cap transition. In principle, each concept can be instrumented with both scintillator and gaseous devices. In practice, the detailed engineering is presently being worked out for scintillator in the first, and for gaseous readout in the second approach.

4.4.4.1.2 Design 1 In the first version of the HCAL design, the barrel is subdivided into two sections in z and eight octants in φ, each octant has two halves which constitute the basic modules, 32 in total. Each module has a weight of almost 20 tons, which is manageable with standard installation techniques. The modules are constructed independently of the active layers, which can be inserted before or after installation of the modules. There are 48 absorber plates, 16 mm thick each, held together by 3 mm thick side panels in the rz planes; no additional spacers are foreseen. The active layers will contribute 4 mm of steel to each absorption layer, and require 5.5 mm for instrumentation (3 mm thick scintillator plus readout and calibration devices). A drawing of the structure is shown in figure 4.4-15(left). The HCAL structure has been extensively simulated using finite element methods, including the integration of the heavy ECAL structure. Maximum deformations are found to be less than 3 mm, if the barrel structure is supported by two rails in the cryostat.

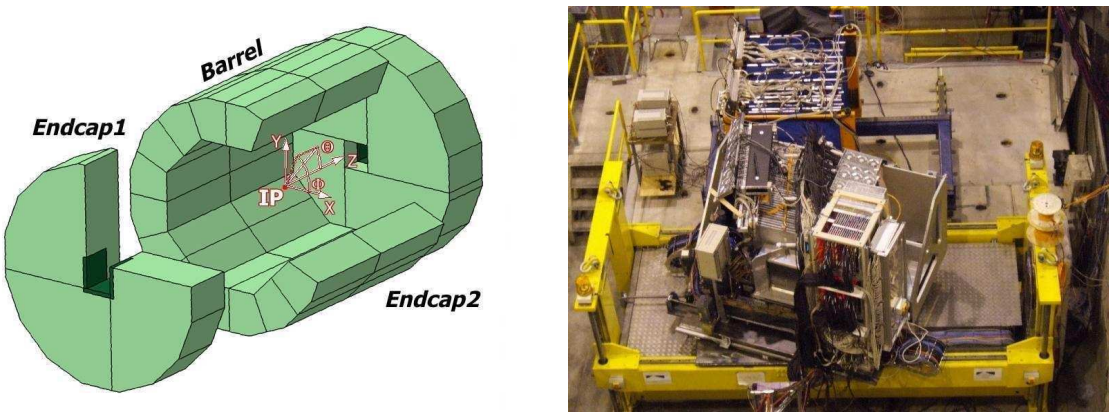

FIGURE 4.4-15. Layout 1 of the HCAL (left), and view of the integrated ECAL and HCAL beam test setup (right).

Presently the boundaries between modules are pointing in φ and in z. Variants with non-pointing boundaries have been validated in finite element calculations as well, but are disfavoured to ease the mechanical construction. The pointing geometry does not degrade the performance as long as the cracks are filled with absorber material, and if the active instrumentation extends up to the boundary within tolerances, which is the case in the present scintillator layer design.

4.4.4.1.3 Design 2 This design intends to reduce cracks both in φ and θ and to reduce the distance between the barrel and the endcaps. The barrel part is made of 5 independent and self supporting wheels along the beam axis which eliminates the θ=90 degree crack. The

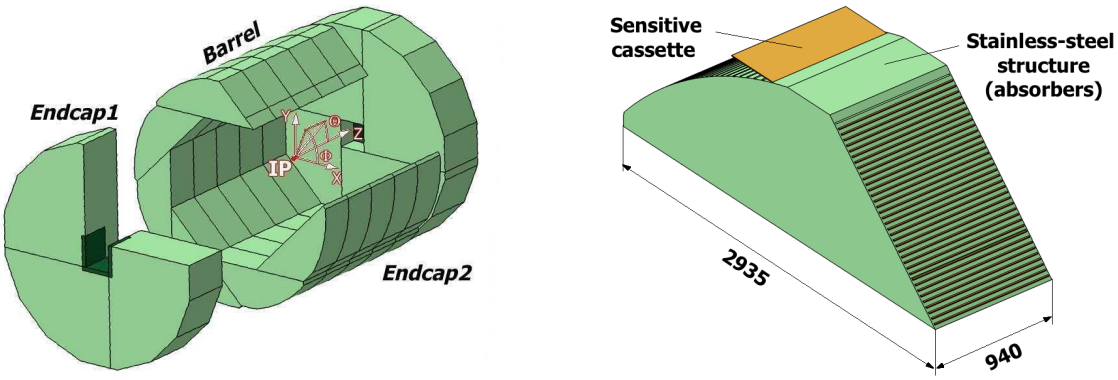

FIGURE 4.4-16. Design 2 layout of the HCAL (left) and layout of one module (right).

segmentation of each wheel in 8 identical modules is directly linked with the segmentation of the ECAL barrel. A module is made of 48 stainless steel absorber plates (welded with 2 transverse 10 mm stainless steel plates) with independent readout cassettes inserted between the plates. They define the rigid structure on to which the corresponding ECAL modules are mounted. A drawing of the structure is shown in figure 4.4-16(right). The absorber plates consist of a total of 20 mm stainless steel: 16 mm absorber from the welded structure and 4 mm from the mechanical support of the detector layer.

Each wheel is independently supported by two rails on the inner wall of the cryostat of the magnet coil. The cables as well the cooling pipes will be routed outside the HCAL in the space left between the outer side of the barrel HCAL and the inner side of the cryostat. The HCAL endcaps the same geometrical structure proposed in design 1. The distance between the barrel and the endcaps, which have the same structure as in design 1, is thus reduced, as only space to ensure inner detector cabling is required.

4.4.4.2 Analogue Hadronic Calorimeter

With the advent of novel, multi-pixel Geiger mode silicon photo-diodes, so-called SiPMs, high granularities as required for a particle flow detector can be realised with the well-established and robust scintillator technology at reasonable cost. The scintillator tiles provide both energy and position measurement and thus allow to trade amplitude versus spatial resolution. The transverse segmentation suggested by simulations is about $3\times3\,\mathrm{cm}^2$ and leads to a number of read-out channels an order of magnitude smaller than in the digital case with $1\times1\,\mathrm{cm}^2$ cells.

4.4.4.2.1 The Active Layers The arrangement of the active layers with internal and external electronics components is sketched in Figure 4.4-17. The layer consists, from bottom to top, of a 2 mm thick steel support plate covered with reflector foil, the scintillator tiles (3 mm), the printed circuit board with electronics components (2 mm), covered with reflector foil from underneath, and a polymide foil for insulation. The PCB carries the SPIROC

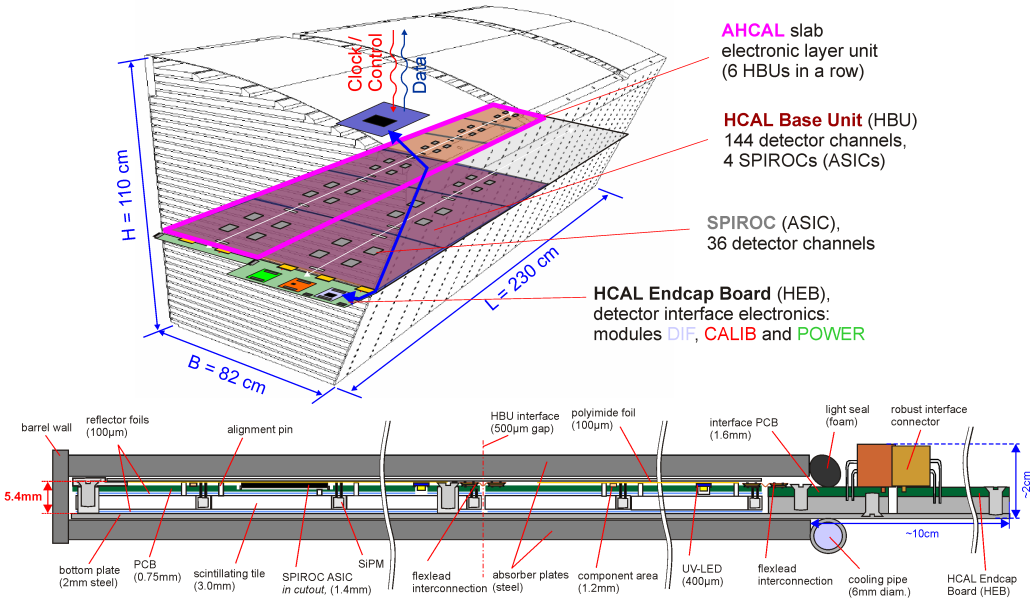

FIGURE 4.4-17. Arrangement of AHCAL layers with electronic components (top), cross section of an active layer (bottom).

readout ASICs (described in section 4.4.5.1)and auxiliary components as well as an LED based optical calibration system, whilst interfaces for data acquisition, clock and control, for power distribution and for calibration system steering are accessible at the end face. Since the ASICs are operated in power-pulsed mode, no cooling is needed inside the detector volume.

The PCB is subdivided into units (HCAL base units, HBUs) of smaller size, manageable for automated mounting and soldering techniques. The standard unit is 12 by 12 tiles, $36 \times 36\,\mathrm{cm}^2$, so six units are aligned along z to fill a half barrel. In order to accommodate the variation in layer width with increasing radius, 4 different HBUs, 8 to 12 tiles wide, are needed. At the layer edges, tiles with smaller size, e.g. $2 \times 3\,\mathrm{cm}^2$, are placed such that the uninstrumented region near the sector boundary is never larger than 5 mm and 2.5 mm on average.

The electronics at the end face will require cooling, mainly due to the use of FPGAs in the DIF (Detector InterFace board described in 4.4.5.2). The boards will extend 5 to 10 cm in z, but occupy only a fraction of the full width in φ, thus leaving space for ECAL and main tracker services as well as for the TPC support along radial directions. The required extra separation between barrel and endcap is therefore much smaller.

4.4.4.2.2 Scintillators and Photo-Sensors, R&D The successful operation of the 8000 channel CALICE HCAL test beam prototype over several years has proven that the new sensor and scintillator technology is robust and reliable. Less than one per-mil of the SiPMs showed signs of aging in form of increasing noise levels. In the meantime, progress was made by various manufacturers, e.g. in Russia or Japan, to provide sensors with lower dark count rate and / or smaller inter-pixel cross-talk which allow to decrease the noise occupancy above threshold of 10^{-3} in the present prototype by an order of magnitude and thus fulfill the requirements from both physics (for neutron hit identification) and DAQ band width. The demands on dynamic range are less critical than for the ECAL.

For the coupling of sensors to scintillator and PCB different approaches are being followed, based on either wavelength-shifting WLS fibre mediated or direct read-out with blue-sensitive photo-diodes. The WLS option was successfully operated in the HCAL (and ECAL) testbeam prototypes. The production, test and integration of sensors has been industrialised further, e.g. the grove for the fibre can be included in the injection moulding process (or the hole in the extrusion process). The positioning of the tiles must match the precision of the PCBs, for example with alignment pins. Alternatively, so-called mega-tiles (plastic modules comprising several cells, separated by groves) are also being discussed.

In the direct coupling case, the sensor is mounted in SMD style with its sensitive surface in the PCB plane, and collects the scintillation light directly from the tile. The tile has to be shaped in a dedicated way to compensate for the otherwise prohibitive light collection non-uniformities. Verification of both concepts in beam tests are important; besides uniformity also the stability of the light collection must be ensured.

Machine-related backgrounds are not a concern for the AHCAL. Simulations have shown that only in the innermost regions of the end-caps, the neutron fluence reaches levels which may degrade the visibility of single photo-electron signals for SiPM monitoring, but not the MIP detection capability. One may have to revert to alternative monitoring strategies here, or use more robust sensors which are under development.

4.4.4.2.3 Calibration The calibration procedure has to relate the electronic readout signal to the energy deposition in the cell. For the pre-amplifiers and discriminators, charge injection is used as in the ECAL or DHCAL case. The gain of the photo-diodes is monitored by means of an optical calibration system, and adjusted via the bias voltage, by observing the spacing between single photo-electron peaks in LED-induced pulse-height spectra. Using test bench measurements this cares also for sensor efficiency variations, correlated with the

gain.

We follow two approaches for the technical realisation of the LED system, one based on a central driver located at the end faces of the modules and optical light distribution via fibres, and one with electrical signal distribution and surface-mounted LEDs for each tile. To check for long-term effects, track segments in hadronic showers can be used for a large fraction of the calorimeter volume. This has been shown with test beam data and simulated for ILD multi-jet events. Also systems based on radio-active sources might need to be considered.

4.4.4.2.4 Optimisation and Performance The main cost- and performance driving parameters of the AHCAL are the depth and the longitudinal and transverse segmentation. These parameters have been varied, and their current settings have been found, using detailed simulations and particle flow reconstruction as described in the overall detector optimisation section 2.2. The simulations include a modeling of inactive regions at module boundaries which is more conservative than the present engineering design.

The performance of a scintillator-tile HCAL with SiPM read-out and the proposed segmentation has been demonstrated with test beam data taken with the CALICE physics prototype. The detector showed very good imaging capabilities which reveal the substructure in hadronic showers, see Fig. 4.4-18.

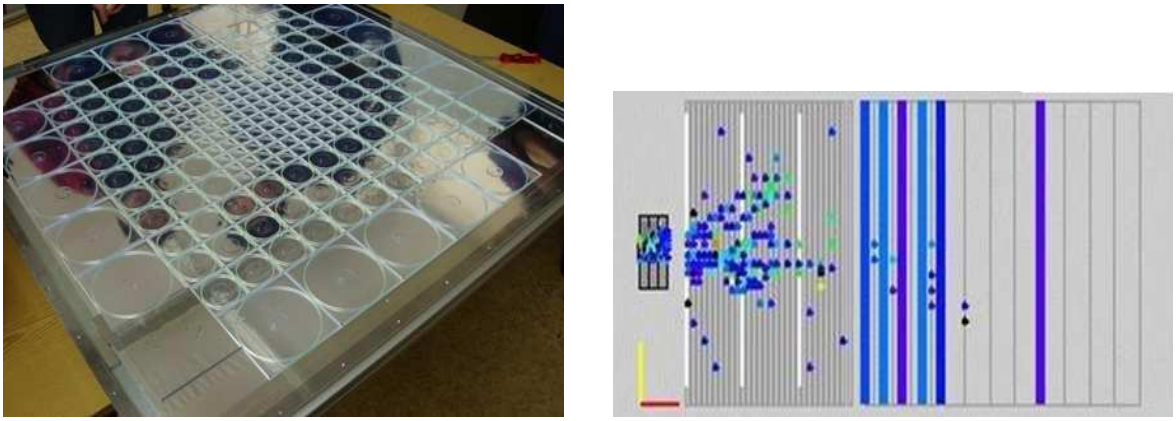

FIGURE 4.4-18. AHCAL physics prototype layer (left), event display (right).

Using test bench data and in-situ measurements, temperature induced variations and SiPM saturation effects could be corrected, and a linearity of better than 2 % for electron induced showers up to 50 GeV was achieved. The calorimeter is non-compensating, but the e/π ratio is not large and the observed linearity is also good for hadronic showers, see Fig. 4.4-19. A hadronic energy resolution of $61\,\%/\sqrt{E}$ is obtained on the electromagnetic scale, which can be reduced to $49\,\%/\sqrt{E}$, preserving linearity, with a simple weighting algorithm, which takes only the energy per tile, but not yet any shower substructure into account.

Based on experimental results from the CALICE prototype a reasonable agreement of the shower profiles with GEANT 4 based simulations has been found, as shown in figure 4.4-20. We found that it is essential to model details of the detector response, such as saturation effects in the scintillator according to Birks' law and the shaping time of the readout electronics, in order to reach this good agreement. These primarily affect the response to neutrons which would otherwise be overestimated.

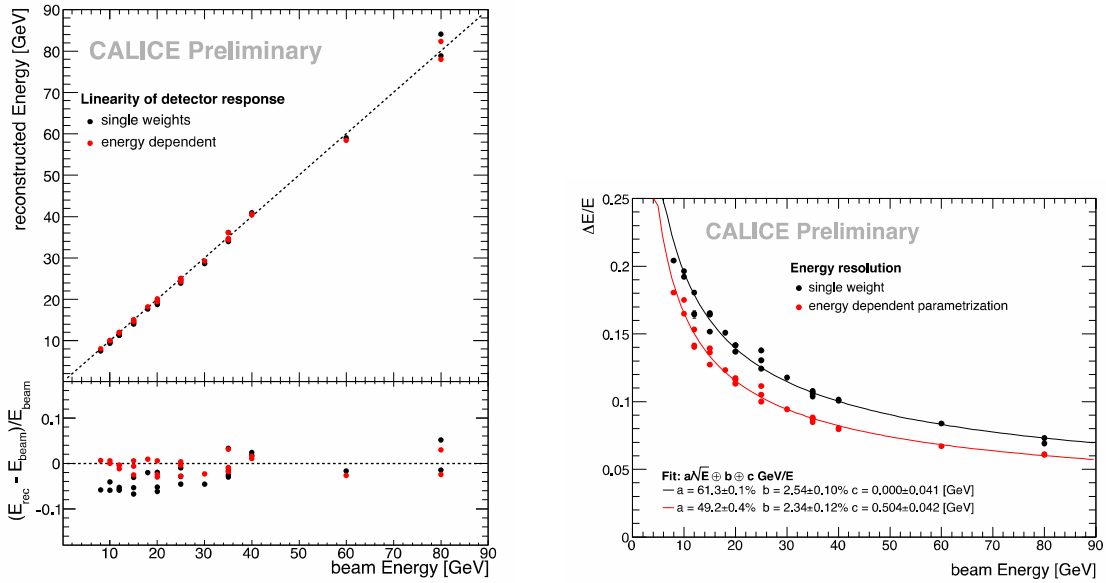

FIGURE 4.4-19. Linearity (left) and resolution (right), on electromagnetic scale and after weighting.

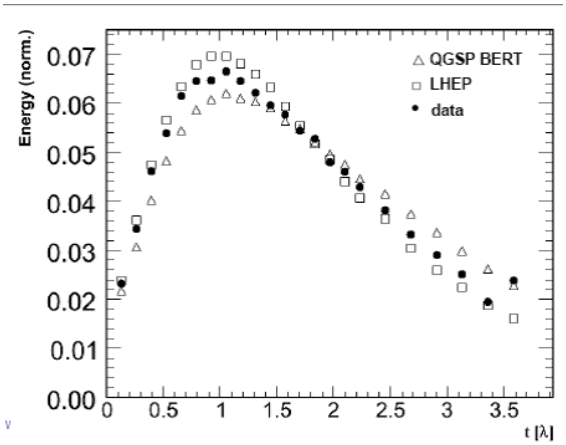

FIGURE 4.4-20. Longitudinal shower profile, test beam data and simulations.

4.4.4.3 Semi-Digital Hadronic Gas Calorimeter

The capacity to apply successfully the particle flow algorithms can be enhanced by increasing the granularity of the different ILD sub-detectors. In the hadronic calorimeter this will doubtlessly help reduce the confusion between charged and neutral hadronic particles by providing a better separation of the associated showers. However, the cost related to such an increase in detector segmentation should be minimised. To satisfy both, a gas hadronic calorimeter with a semi-digital readout is proposed. The study of such an HCAL has been going on for few years in order to validate this option.

The choice of gaseous detectors as the sensitive medium in the HCAL offers the possibility to have very fine segmentation while providing high detection efficiency. The glass resistive plate chamber (GRPC) is one of these detectors which can be built in large quantities at low cost. Large GRPCs as the ones required for the ILD HCAL can be easily produced.

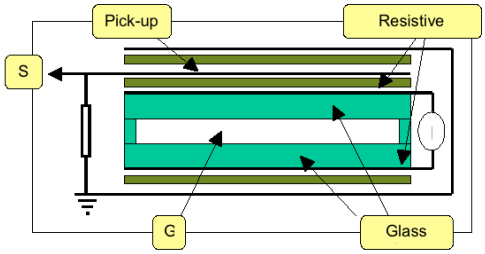

FIGURE 4.4-21. Single gap GRPC scheme

This is an important advantage with respect to other detectors since it guarantees very good homogeneity. Several experiments like BELLE have been using such large detectors with success for years. However, the GRPCs to be used in the ILD HCAL need to be more elaborate. As the HCAL is situated inside the magnet coil, the sensitive medium thickness is an important issue. Very thin GRPCs are requested and 3.3 mm thick GRPCs were indeed produced and successfully tested. In figure 4.4-21 a scheme of such a single gap GRPC is shown. Some key properties of these detectors are:

- GRPC operated in avalanche mode and have been shown to show no ageing for the accumulated charge expected over the ILC running period.
- Test beam performed at DESY have shown that a strong magnetic field has negligible effect on GRPC performance.
- GRPC detectors are insensitive to slow neutrons preventing thus an additional confusion.

Increasing the granularity will lead to a large number of channels. To limit the amount of data we propose a semi-digital readout solution. This simplifies the data treatment while minimising the consequences on the energy resolution performance. Indeed, based on several independent simulation studies, a two-bit readout would provide better energy resolution in the low-energy jet range (1–20 GeV) and a comparable one at higher energies when compared to an analogue readout [108].

FIGURE 4.4-22. Mini-DHCAL prototype (left); Prototype of a large instrumented GRPC (right).

Similiar to the case of the analogue HCAL the readout electronics will be integrated into the sensitive layer of the system, thus minimising dead areas. Large electronics boards

are assembled together to form extra large boards before they are attached to the GRPCs. The board assembly will be made possible thanks to a mechanical structure made of 4 mm stainless steel plate. In addition, to keep the HCAL as compact as possible, the fully equipped electronic boards are designed to have less than 3 mm thickness in all. A mini hadronic calorimeter using this concept was built and successfully tested in beam conditions at CERN in 2008 (see figure 4.4-22).

4.4.4.3.1 The Active Layers R&D activities on large GRPC detectors are being followed. Different kinds of spacers are tested to reduce detector noise and inefficiency while increasing the detector robustness. New gas distribution schemes as well as gas recycling systems are worked out to lower gas consumption and pollution. Although the present GRPC detection rate of 100 Hz/cm^2 obtained with efficiencies greater than 90 % is enough for the needs of ILC, a new development based on using semi-conductive glass will lead to increase this rate. Multi-gap GRPCs are also investigated. This allows reducing the spread of the MIP charge spectrum leading to a better exploitation of the semi-digital information.

Few large GRPCs with different options were built and are currently tested using a 1 m^2 fully equipped electronics board (see figure 4.4-22(right)). This will allow to build the most appropriate GRPC detector to be used in the ILD DHCAL.

In addition to the GRPCs activities, development on other thin and large gaseous detectors like GEM and MICROMEGAS are also followed.

The GRPCs produces strong electric currents (a few 10 pC in 10-20 ns) in the DHCAL pads. In order to reduce cross-talk effects between the pads below the percent level the very front end electronics is located on the other side of the PCBs, (semi-)buried vias are used.

4.4.4.3.2 Energy Reconstruction & Calibration The semi-digital HCAL cell energy reconstruction can, to first order, be estimated as $E_{\text{cell}} = 1$, 5 and 10 MIP if the charge is above the thresholds typically placed at 0.1, 2 and 8 MIPs (for the envisaged GRPC about 0.26, 5.2 and 20.8 pC). Preliminary results on simulation, without algorithm optimisation, show PFA performances comparable to the AHCAL reconstruction.

An interesting aspect of the gaseous semi-digital HCAL is the simplicity with which the detector calibration is performed, if one is needed at all. The sDHCAL energy calibration requires 3 independent steps:

- *An intercalibration of the ASIC thresholds in charge*: All ASICs will have to be tested and calibrated by injecting a precisely controlled charge, adapted for each of the threshold, at the entrance of their final ASU/PCB pad. The variations can be compensated channel by channel in the ASIC by adjusting the channel gains (over a range of 0–2 coded on 8 bits in the current version of HaRDROC, described in sec 4.4.5.1);
- *A calibration of the multiplicity of the RPC*: The multiplicity response curve of the RPC to muons as a function of high voltage applied, thresholds, position and gas flow and atmospheric pressure can be measured on a cosmic test bench or muon beam and parametrised for each type of RPC.
- *A calibration with physics*: The two first steps bring an absolute calibration at the level of the MIP, which can be cross-checked with cosmic muons or $Z \rightarrow \mu\mu$ events; the final energy scale will be a complex interplay in the scope of the PFA analysis between the clustering algorithms, jet and particle energies and types.

The definition of the calibration procedure, and an estimation of the achievable precision, is a part of the DHCAL $1\,m^3$ programme.

4.4.4.3.3 Status and Future R&D Plans A technological prototype of $1\,m^3$ HCAL based on the same principle is currently under study. It aims to validate at large scale the semi-digital HCAL concept. Questions related to the mechanical structure mentioned in the previous section as well as the management of the limited space for services will be addressed. The prototype is to be built by 2010. Combined test beams with the different ECAL prototypes developed within the CALICE collaboration will then be organised at FERMILAB and CERN.

4.4.5 Calorimeter Readout System

A considerable effort has been made in the framework of the CALICE collaboration to standardise the read-out of different type of calorimeter with embedded Very Front-End (VFE) electronics while minimising the space needed for the configuration distribution and the data readout.

4.4.5.1 Very Front End (VFE) ASIC description

The front-end ASICs should ensure a data format uniformity in all the calorimeters, thus having identical back-ends to allow a standardised detector interface board (DIF) for all detectors.

Ensuring such a compatibility between all electronics components involves a unique read-out system based on token ring that allows a number of ASICs to be read out by one output line, using the same protocol. That protocol will help reducing the number of data lines outputted from the calorimeters where the front-end ASICs are now embedded.

All the VFE will feature three operating mode : Acquisition (1 ms), A/D conversion (1 ms), and data outputting during inter-bunch (199 ms) using an ultra low power protocol. When a FE ASIC is in neither of the above modes, it is turned to an idle mode to save up to 99.5 % of power, bringing the power down to 10 to 25 μW per channel.

Three ASICs differing mostly on their analog front-end have been developed to fit the different detectors.

- SKIROC ("Silicon Kalorimeter Integrated Read-Out Chip"): 64 channels charge preamplifier for charge measurement down to the MIP (3.84 fC) to a maximum around 2500 MIP. Dual gain shaping, analog memory, 12 bit-digitisation, self-trigger capability on single MIP. 25 μW/ per channel to run without any active cooling ensuring therefore an extreme compactness of the calorimeter.
- SPIROC ("Si-Pm Integrated Read-Out Chip"): auto-triggered, dual-gain voltage preamp, 36-channel ASIC which allows to measure for each channel the charge from 1 to 2000 photo-electrons with a 12 bit internal ADC and the time with a 1 ns accurate TDC. One 8-bit 5 V input DAC per channel ensures operation of the SiPM at its optimum bias.
- HARDROC("HArdronic RPC Detector ReadOut Chip"): 24 channels semi-digital read-out for RPCs or MicroMegas pads, allowing both good tracking and coarse energy measurement. Each channel made of a variable gain low input impedance current preamp followed by 3 variable gain shapers and 3 low offset discriminators to auto-trig down

to 10 fC up to 10 pC. A 128 deep digital memory to store the encoded outputs of the discriminators as well as the bunch crossing identification.

Prototypes of each type have been produced in the years 2007-2008. Boards equipped with 4 HARDROC(v1) ASICs have been designed for the DHCAL. The electronics readout under beam conditions has been validated. Some key points such as the digital daisy chaining for configuration and readout, the stability, the efficiency, and the capability of the chip to be used without any external components have been checked. A small production is foreseen in Fall 2009 to equip a technological prototype (called EUDET prototype) in 2010.

4.4.5.2 Detector Interface

The ASICs are managed by specifically designed DIF (Detector InterFace) cards; one DIF handles a full slab, whose maximum size are of $260 \times 141\,\mathrm{cm}^2$ for the AHCAL structure, and $90 \times 273\,\mathrm{cm}^2$ for the DHCAL structures. The corresponding maximum number of ASIC per slab are respectively 576 and 420. For an estimated occupancy per ASIC of the HCAL of 5 events / train of 2600 BC, the expected data volume to be read in the inter-train is of 336000 bits; readout at a speed of 5 MHz this takes 67 ms. During the readout phase the ASICs will be on standby except when explicitly addressed.

4.4.5.3 DAQ system

The data acquisition (DAQ) system is defined to start with the detector interface boards (DIF) which service the detector slabs from the ends and which are specific to the VFE of the subsystem. The DIF provides a generic interface, independent of the calorimeter type, to the DAQ system. Because of the limited space available for cabling and services, data are concentrated onto a single optical communication channel with the off-detector electronics, by a link-data aggregator (LDA) inside the detector. The resulting data volume is mainly determined by the zero-suppression scheme incorporated in the self-triggering Front-End electronics. But as the calorimeter has over 100 million readout channels, significant demands are put on the scalability and on an attractive price/performance ratio of the read-out electronics and the associated data-acquisition systems. Therefore the design should minimise the number of LDAs and maximise the data rates on the link which are expected to be 10 GB Ethernet links.

With the data delivered over optical high-speed links, an optical switch is used to dynamically redirect the data streams coming from the detector towards available data receivers of the off-detector system. The off-detector is currently realised as a PCIexpress card hosted in a commodity PC but can be easily implemented in a μTCA crate for the future detector.

For the event building the machine clock will be fed into the off-detector system to the data concentrators and the detector interfaces. The requirements on the clock are a low jitter and fixed latency between the machine clock and the clock in the detector interfaces. This part of the system needs to be custom built to guarantee delivery times and latencies.

For all of the introduced systems (detector interface, data concentrator, off detector system and the clock) prototypes already exist which have been built within the EUDET [109] project. The prototypes perform the same tasks as in the final detector, however the prototypes are build for a proof of principle and need to be optimised for the final detector design.